National Technical University of Athens
School of Mechanical Engineering
Fluids Sector
Laboratory of Thermal Turbomachines
Parallel CFD & Optimization Unit

Parametric studies of aerothermal optimization of internally cooled turbine blade airfoil, using the continuous adjoint method

MSc Thesis by
Evangelos Mallios

for the Joint Postgraduate Studies Program in Computational Mechanics

Supervisor
Kyriakos C. Giannakoglou, Professor

Athens, 2023

National Technical University of Athens - School of Mechanical Engineering -
Parallel CFD & Optimization Unit

Abstract

Parametric studies of aerothermal optimization of internally cooled turbine blade airfoil, using the continuous adjoint method

by Evangelos Mallios

The present thesis deals with the aerothermal optimization of an internally cooled turbine blade, using the continuous adjoint method. The computational procedure is based on tools developed by the PCOpt/NTUA members, namely the GPU accelerated PUMA software. The optimization procedure is applied to the C3X turbine blade, being a well-known test-case for validation purposes, involving CFD optimization in Conjugate Heat Transfer problems. The optimization aims at decreasing the highest solid temperature by updating the positions of the ten cooling channels inside the blade airfoil. The Method of Moving Asymptotes is used to compute the design variables in each optimization cycle. Initially, only the primal problem is solved, using the Spalart-Allmaras turbulence model, to compare with the experimental data in the bibliography. Five operating points are considered, one of which corresponds to transonic flow. Proceeding with the first series of the optimization runs, the starting geometry is derived from either the baseline model or blade airfoils that have also been optimized in terms of total pressure losses. Parametric studies follow, changing the total number of cooling channels, and further optimizing the cooling system, allowing their displacement toward the trailing edge.

Εθνικό Μετσόβιο Πολυτεχνείο - Σχολή Μηχανολόγων Μηχανικών - Μονάδα Παράλληλης ΥΡΔ & Βελτιστοποίησης

Περίληψη

Παραμετρικές μελέτες αεροθερμικής βελτιστοποίησης μορφής αεροτομής ψυχόμενου πτερυγίου στροβίλου με χρήση της συνεχούς συζυγούς μεθόδου

Ευάγγελος Μάλλιος

Η διπλωματική εργασία πραγματεύεται την αεροθερμική βελτιστοποίηση ενός εσωτερικά ψυχόμενου πτερυγίου στροβίλου, με χρήση της συνεχούς συζυγούς μεθόδου. Η υπολογιστική διαδικασία βασίζεται σε εργαλεία που αναπτύχθηκαν από τα μέλη της ΜΠΥΡΒ/ΕΜΠ, συγκεκριμένα το λογισμικό PUMA που τρέχει σε κάρτες γραφικών. Η διαδικασία βελτιστοποίησης εφαρμόζεται στο πτερύγιο στροβίλου C3X, καθώς αποτελεί γνωστή περίπτωση μελέτης για τον έλεγχο λογισμικών Υπολογιστικής Ρευστοδυναμικής που σχετίζονται με φαινόμενα Συζευγμένης Μεταφοράς Θερμότητας. Η βελτιστοποίηση στοχεύει στη μείωση της μέγιστης θερμοκρασίας του στερεού, ανανεώνοντας τις θέσεις των δέκα ψυκτικών οπών στην αεροτομή του πτερυγίου. Για τον υπολογισμό των μεταβλητών σχεδιασμού σε κάθε κύκλο βελτιστοποίησης, χρησιμοποιείται η Μέθοδος των Κινούμενων Ασυμπτώτων. Αρχικά επιλύεται μόνο το πρόβλημα ροής, με χρήση του μοντέλου τύρβης των Spalart − Allmaras, ώστε να επιτευχθεί η σύγκριση με τα πειραματικά δεδομένα της βιβλιογραφίας. Μελετώνται πέντε σημεία λειτουργίας, με ένα από αυτά να αφορά ηχητική ροή. Συνεχίζοντας με την πρώτη σειρά εκτελέσεων του κώδικα βελτιστοποίησης, η αρχική γεωμετρία προέρχεται είτε από το μοντέλο της βιβλιογραφίας, είτε από βελτιστοποιημένες, ως προς τις απώλειες ολικής πίεσης, αεροτομές. Ακολουθούν παραμετρικές μελέτες, μεταβάλλοντας το συνολικό αριθμό των ψυκτικών οπών στην αεροτομή του πτερυγίου και βελτιστοποιώντας περαιτέρω τη ψυκτική διάταξη, επιτρέποντας τη μετατόπιση τους προς την ακμή φυγής.

Acknowledgements

First of all, I would like to thank my professor and supervisor Kyriakos C. Giannakoglou for his trust and guidance in the writing of this thesis. His teaching, under the Postgaduate Studies Program, motivated me to get involved in optimization processes. His observations and comments were crucial to the final outcome of this project.

Furthermore, I would like to thank Dr. Xenofon Trompoukis for introducing me to PUMA software and its parameterization tools. I am grateful for his patience and willingness to help me to overcome any technical difficulties that arose during the project.

Finally, I would like to thank graduate student Dimitris Panagiotopoulos for his excellent work on the C3X airfoil shape optimization. His aerodynamically optimized blades were used in this thesis to optimize their aerothermal performance.

Contents

Abstract **iii**

Acknowledgements **v**

1 Introduction **1**
1.1 CHT Optimization 1
1.2 Literature Review on Continuous Adjoint Method 2
1.3 Thesis Overview 2

2 Mathematical Approach **3**
2.1 Governing Equations 3
2.2 Turbulence Modeling 4
2.3 The Continuous Adjoint Method 5
2.3.1 Developing the mean-flow integral 6
2.3.2 Developing the Spalart-Allmaras integral 8
2.3.3 Developing the Eikonal integral 10
2.3.4 Developing the heat conduction integral 10
2.3.5 Field Adjoint Equations (FAEs) and Adjoint Boundary Conditions (ABCs) 11
2.3.6 Expression for SDs 12
2.4 PUMA Software 13
2.4.1 Grid Properties 13
2.4.2 Coupling Scheme 15
2.4.3 Method of Moving Asymptotes 16

3 Validation of the Solver and Optimization Set-Up **19**

4 Results **27**
4.1 TH1 Optimization 29
4.2 TH2 Optimization 40
4.3 Additional Parametric Studies 54

5 Conclusions **71**

Bibliography **73**

List of Abbreviations

ABC	**A**djoint **B**oundary **C**onditions
CFD	**C**omputational **F**luid **D**ynamics
CHT	**C**onjugate **H**eat **T**ransfer
FAE	**F**ield **A**djoint **E**quations
FSI	**F**luid **S**olid **I**nterface
GPU	**G**raphic **P**rocessing **U**nit
MMA	**M**ethod of **M**oving **A**symptotes
MPI	**M**essage **P**rotocol **I**nterface
NTUA	**N**ational **T**echnical **U**niversity of **A**thens
PCOpt	**P**arallel **C**FD & **O**ptimization Unit
PDEs	**P**artial **D**ifferential **E**quations
PUMA	**P**arallel Flow-Solver, on **U**structured Grids for **M**ulti-Row Analysis & **A**djoint-based optimization
RANS	**R**eynolds-**A**veraged **N**avier-**S**tokes
SDs	**S**ensitivity **D**erivatives

1 Introduction

1.1 CHT Optimization

The high efficiency of gas turbines is inextricably linked to aerodynamically designed blades and high turbine inlet temperatures. The first turbine row, located right after the combustor, is exposed to high gas temperatures, which should not exceed the limit set by the thermal resistance of the blade's material. For that reason, it is necessary to reduce the temperature locally in the turbine blade, using a cooling configuration. Blade cooling can commonly be achieved by injecting cold air into the main flow (external) or passing the air through channels inside the blade (internal). In the case of internal cooling, the air used to cool down the blade is usually extracted from the compressor cascade flow. These types of physical problems, involving a solid body inside a flow field with thermal interaction between them, are called Conjugate Heat Transfer (CHT) problems.

In a CHT problem, the computational domain splits into a fluid and a solid one, with heat transfer crossing the boundary between them, known as Fluid Solid Interface (FSI) region. PDEs in fluid and solid domains can be either strongly or loosely coupled. In the first case, the equations are solved simultaneously, while in the latter one, there are 2 different solvers, one for each domain, communicating between them with a coupling scheme [11].

The adjoint method is a widely-used gradient-based optimization algorithm, computing the objective function's sensitivity derivatives (SDs) with respect to the design variables. The method is used in the current thesis, as it is ideal for shape optimization problems since its cost is proportional to the number of objective functions and not to the number of design variables. For that reason, it is preferred to the stochastic optimization algorithms and is applied to aerodynamic and turbomachinery applications, combined with various solvers. In that case, the design variables consist of the geometrical properties of a blade or any aerodynamic surface. For the aerothermal optimization of an internally cooled turbine blade, the design variables contain the coordinates of channels' centers or their perimeter points. The main disadvantage of the method is its dependence on the primal problem, meaning that if either its formulation or the objective function is changed, the adjoint formulation has to be reprogrammed too.

The C3X turbine blade [6] is a benchmark test-case, which has been frequently used for validation purposes, involving CFD and optimization algorithms in CHT problems. In [12], an evolutionary algorithm is used to optimize the cooling system of the blade, while the immersed boundary method is used in [3] discretizing the fluid and solid domains with a common grid. In [10], a combination of random search and gradient-based schemes is proposed, to optimize the number and shape of cooling channels. The Boss-Quattro platform with MMA method, is used in [21].

1.2 Literature Review on Continuous Adjoint Method

Extensive research carried out by the PCOpt/NTUA members on the gradient-based methods, forms the basis of the present thesis. Using the in-house PUMA software [2] an optimization procedure is performed, aiming to minimize the highest blade temperature to the 2D turbine problem, by controlling the cooling channels' locations. It is noted that a similar procedure with a different objective function (total pressure losses) has already been completed [13], the outcomes of which have been used for thermal optimization in this thesis. Adjoint formulations for the compressible RANS equations were developed in [14], while the method includes the Spalart-Allmaras model, used in the current thesis, introduced in [22]. The Eikonal equation for computing the distance field and its adjoint counterpart was presented in [15]. The continuous adjoint method is extended to CHT problems, including the fluid energy and solid heat conduction equations, which has been developed in [5] for incompressible and in [20] for compressible flows and applied to the internally cooled C3X turbine blade. The latter paper describes the mathematical approach, herein summarized in chapter 2.

1.3 Thesis Overview

The 5 chapters of the present thesis are summarized below:

- Chapter 1 - Introduction
- Chapter 2 - Mathematical Approach: The continuous adjoint method in the CHT problem is described. The entire computational procedure is outlined, starting with the equations for the primal problem and proceeding to the development of the adjoint equations, along with their boundary conditions. Information on discretization and coupling schemes are given, while grid properties are detailed and the MMA method is demonstrated based on [19].
- Chapter 3 - Optimization of C3X Turbine Airfoil: This chapter contains a detailed presentation of the geometrical aspects of the C3X turbine, including tables with information on the cooling channels' positions and flow properties. The conditions of the 5 cases studied in the present thesis are included, while a series of runs are carried out, with the Spalart-Allmaras turbulence model, including comparisons with the experimental data. All data were obtained from [6].
- Chapter 4 - Results: In this chapter, the results of the optimization procedure for the internally cooled blade are presented. Runs are divided into two different categories according to whether the starting geometry is the baseline one from [6] or based on [13]. Additional parametric studies are performed with modifications in the number of design variables, by changing the number of cooling channels which can be displaced. Further optimization is performed by updating the design variables to consist of the 3 back channels, following the main optimization procedure.
- Chapter 5 - Conclusions: The final conclusions are drawn and possible future approaches related to the aerothermal optimization of the C3X turbine airfoil are proposed.

2 Mathematical Approach

2.1 Governing Equations

Using the Einstein summation notation, the Reynolds-Averaged Navier-Stokes (RANS) equations [20] over fluid domain Ω^F read:

$$R_n^{MF} = \frac{\partial U}{\partial \tau} + \frac{\partial f_{nk}^{inv}}{\partial x_k} - \frac{\partial f_{nk}^{vis}}{\partial x_k} = 0 \tag{2.1}$$

where $f_k^{inv} = [\rho v_k \quad \rho v_k v_1 + p\delta_{1k} \quad \rho v_k v_2 + p\delta_{2k} \quad \rho v_k h_t]^T$ contains the inviscid fluxes (convection, pressure terms) and $f_k^{vis} = [0 \quad \tau_{1k} \quad \tau_{2k} \quad v_\ell \tau_{\ell k} + q_k^F]^T$ contains the viscid fluxes (dissipation terms). $\frac{\partial U}{\partial \tau}$ is the pseudo-time term, with $U = [\rho \quad \rho v_1 \quad \rho v_2 \quad \rho E]^T$ and E being the total energy per unit mass. Henceforth, R will be used to denote the residual value of an equation. The index $n = 1, 2, 3, 4$ refers to the n^{th} component of the aforementioned vectors, indicating which equation will be satisfied.

For instance, $n = 1$ refers to $R_1^{MF} = 0$ or $\frac{\partial(\rho v_k)}{\partial x_k} = 0$, thus the continuity equation is satisfied. The general form of the motion equation for the steady compressible fluid flows is $\frac{\partial(\rho v_k v_i)}{\partial x_k} + \frac{\partial(p\delta_{ik})}{\partial x_k} - \frac{\partial \tau_{ik}}{\partial x_k} = 0$ or $R_{2-3}^{MF} = 0$ where $i = 1, 2$ for 2D flows. ρ and p stand for the fluid's density and pressure, while v_k are the velocity components in the x_k direction of the Cartesian coordinate system. The stress tensor, defined as $\tau_{km} = (\mu + \mu_t)\left(\frac{\partial v_k}{\partial x_m} + \frac{\partial v_m}{\partial x_k} - \frac{2}{3}\delta_{km}\frac{\partial v_\ell}{\partial x_\ell}\right)$, contains fluxes due to molecular diffusion and turbulent fluctuations, based on the Boussinesq hypothesis. μ and μ_t represent the bulk and turbulent viscosity, while k is the turbulent kinetic energy. δ_{km} is the Kronecker symbol. The dynamic viscosity μ is a function of fluid's temperature T^F, established by Sutherland [18], hence $\mu = \mu_{ref}\left(\frac{T}{T_{ref}}\right)^{1.5}\frac{T_{ref}+C}{T+C}$, with $C = 110.56$ K, $T_{ref} = 273.11$ K and $\mu_{ref} = 1.7894 \cdot 10^{-5}$Pa $\cdot$ s. For the computation of μ_t, turbulence models must be introduced. With h_t being the fluid's total enthalpy, the conservation of energy states that $R_4^{MF} = 0$ or $\frac{\partial(\rho v_k h_t)}{\partial x_k} = \frac{\partial(v_\ell \tau_{\ell k})}{\partial x_k} + \frac{\partial q_k^F}{\partial x_k} = 0$ where the heat fluxes are equal to $q_k^F = \kappa^F \frac{\partial T^F}{\partial x_k}$, according to Fourier's law (the index F indicates the fluid domain Ω^F). $\kappa^F = C_p\left(\frac{\mu}{\mathrm{Pr}} + \frac{\mu_t}{\mathrm{Pr}_t}\right)$ is the fluid's conductivity, where C_p is the specific heat capacity under constant pressure. The laminar and turbulent Prandtl numbers equal Pr = 0.72 and Pr_t = 0.90, respectively.

The heat conduction equation over solid domain Ω^S can be written as:

$$R^S = -\frac{\partial q_k^S}{\partial x_k} = 0 \tag{2.2}$$

where $q_k^S = \kappa^S \frac{\partial T^S}{\partial x_k}$ are the heat fluxes and T^S, κ^S the temperature and thermal conductivity of the blade, respectively. Index S indicates the solid domain Ω^S.

Equation (2.1) and eq. (2.2) are coupled for the CHT problem. The boundary of the domain Ω^F is $S_F = S_{F,I} \cup S_{F,O} \cup S_{F,FSI} \cup S_{F,per}$. Along the inlet $S_{F,I}$ fixed values

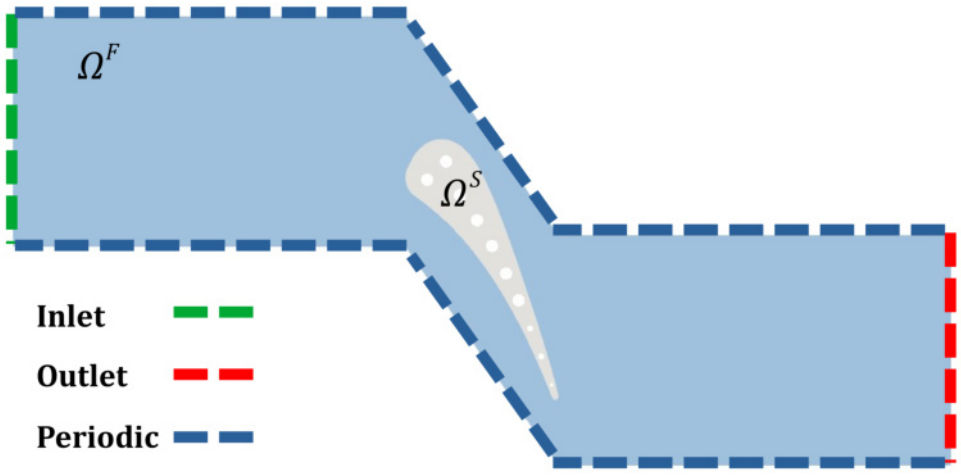

FIGURE 2.1: Computational domain for the 2D CHT problem along with the C3X airfoil geometry and boundaries.

are imposed on the total pressure, total temperature, and flow angles. The Mach number variable is extrapolated from the interior of the fluid domain to the boundary. The static pressure is imposed along the outlet $S_{F,O}$ while the temperature and velocity components are extrapolated. Information on the above values is given in table 3.3. $S_{F,per}$ denotes the periodic boundary conditions to simulate the passage through the stator cascade. $S_{F,FSI}$ stands for the Fluid-Solid Interface (FSI) region between the flow and the airfoil. Along the region, the no-slip condition is imposed. The boundary of the solid domain Ω^S is decomposed into $S_S = S_{S,W} \cup S_{S,FSI}$. S_{SW} includes the interior airfoil's walls, i.e. the cooling holes' perimeters, based on the geometrical data of table 3.1. No coolant flow simulation is considered, instead, the convective heat flux boundary condition is used. Finally, the boundary conditions dictate that the temperature and heat flux are the same across the common FSI boundary $S_{F,FSI}, S_{S,FSI}$:

$$\begin{aligned} T^F &= T^S \\ q_k^F n_k^F &= -q_k^S n_k^S \end{aligned} \tag{2.3}$$

where n_k^F, n_k^S are the unit normal vectors to the FSI, pointing toward Ω^F and Ω^S respectively. The coupling scheme is presented in detail in section 2.4.2.

Figure 2.1 illustrates the computational domain which consists of the fluid domain Ω^F including the fluid region, and solid domain Ω^S including the airfoil, defined by the aforementioned boundaries. The RANS equations eq. (2.1) along with the turbulence model eq. (2.4) and Eikonal eq. (2.7) equations, (which will be presented in the following sections), are solved in the fluid domain Ω^F. In the solid domain Ω^S, the heat conduction equation eq. (2.2) is solved.

2.2 Turbulence Modeling

Given that turbulence is a high-complexity fluid motion type, a precise definition of it seems to be rather impossible. It can be characterized as a dissipative, diffusive,

and rotational phenomenon and is thought to be nonlinear and time-dependent. In order to find a direct solution, a huge amount of computational power is required, due to the small-scale fluctuations of the flow quantities', appearing in the RANS equations. Time must be discretized into incredibly small steps, and large computing meshes are necessary. Thus, turbulence should be commonly modeled in fluid mechanics applications.

The Spalart-Allmaras one-equation turbulence model [17] is used in this thesis. Introducing the Spalart-Allmaras variable $\tilde{\nu}$, the turbulent viscosity is given by $\mu_t = \rho\tilde{\nu}f_{v1}$, where $f_{v1} = \frac{\chi^3}{\chi^3+C_{v1}^3}$ with $\chi = \frac{\tilde{\nu}}{\nu}$, $C_{v1} = 7.1$. The transport equation of $\tilde{\nu}$ reads:

$$R^{\tilde{\nu}} = \frac{\partial}{\partial x_k}(\rho v_k \tilde{\nu}) - \frac{\rho}{\sigma}\frac{\partial}{\partial x_k}\left[[\nu + (1+C_{b2})\tilde{\nu}]\frac{\partial \tilde{\nu}}{\partial x_k}\right] + \frac{\rho C_{b2}\tilde{\nu}}{\sigma}\frac{\partial}{\partial x_k}\left(\frac{\partial \tilde{\nu}}{\partial x_k}\right) - \mathcal{P}^{\tilde{\nu}} + \mathcal{D}^{\tilde{\nu}} = 0 \tag{2.4}$$

where $\mathcal{P}^{\tilde{\nu}} = \rho C_{b1}(1-f_{t2})\tilde{S}\tilde{\nu}$ and $\mathcal{D}^{\tilde{\nu}} = \rho(C_{w1}f_w - \frac{C_{b1}}{\kappa^2}f_{t2})\left(\frac{\tilde{\nu}}{d}\right)^2$ are the production and destruction terms of $\tilde{\nu}$ respectively. d denotes the distance from the nearest solid wall boundary. In the production term $\tilde{S} = S + \frac{\tilde{\nu}}{\kappa^2 d^2}f_{v2}$, with $f_{v2} = 1 - \frac{\chi}{1+\chi f_{v1}}$ and S being the strain rate magnitude. κ is the von Kármán constant, taken as $\kappa = 0.41$, while $\sigma = \frac{2}{3}$, $C_{b1} = 0.1355$, and $C_{b2} = 0.622$. C_{w1} is a function of $C_{w1} = \frac{C_{b1}}{\kappa} + \frac{1+C_{b2}}{\sigma}$. Continuing on, $f_w = g\left(\frac{1+C_{w3}^6}{g^6+C_{w3}^6}\right)^{\frac{1}{6}}$, with $g = r + C_{w2}(r^6 - r)$, $C_{w2} = 0.3$, $C_{w3} = 3$, and $r = \frac{\tilde{\nu}}{\tilde{S}\kappa^2 d^2}$. Lastly, $f_{t2} = C_{t3}e^{-C_{t4}\chi^2}$, where $C_{t3} = 1.2$ and $C_{t4} = 0.5$.

2.3 The Continuous Adjoint Method

In this section, the formulation of the continuous adjoint method for an objective function F is presented. The full mathematical development, including the CHT problem for the 3D C3X turbine blade, is published in [20]. Furthermore, the PhD thesis of Gkaragkounis [4] and his paper [5] provide a more detailed presentation of the adjoint formulation in the CHT problem for incompressible flows, developed in OpenFOAM. The optimization aims at minimizing the highest blade temperature, thus the objective function will be approximated by the differentiable expression of $\max(T^S)$ or:

$$F = \frac{\sum_{\text{solid}} T^S e^{aT^S}}{\sum_{\text{solid}} e^{aT^S}} \tag{2.5}$$

where $a = 0.2$. The above operator is known as Boltzmann softmax operator. For the cases of $a \to -\infty$, $a \to 0$, and $a \to \infty$, the function approximates the behavior of the min, mean, and max function, respectively. The function $p(x_i) = \frac{e^{ax_i}}{\sum_{j=1}^{n} e^{ax_j}}$ normalizes the inputs x_i into a probability distribution. For instance, with $\boldsymbol{x} = [1 \quad 5 \quad 3]$ being the input vector, the function returns $\boldsymbol{p} = [0.2120 \quad 0.4718 \quad 0.3162]$ for $a = 0.2$ and $\boldsymbol{p} = [0.0900 \quad 0.6652 \quad 0.2447]$ for $a = 0.5$. The formula is a smooth differentiable approximation of arg max function, which marks the input vector's index i, where the maximum value appears. In the example above, arg max returns the vector $[0 \quad 1 \quad 0]$, meaning it is a discontinuous function. The maximum value is calculated, by summing the products $\sum(x_i p(x_i))$, thus forming eq. (2.5). As it turns out, $p(x_i)$ are the weighting factors, assigned to x_i. Higher values of x_i (those approaching the maximum value), are given higher weights. For $\boldsymbol{x} = [1 \quad 5 \quad 3]$, Boltzmann operator determines the maximum value as 3.5196 ($a = 0.2$) and 4.1504 ($a = 0.5$).

The continuous adjoint method starts with the definition for the augmented form of F, denoted by F_{aug}:

$$F_{aug} = F + \int_{\Omega^F} \Psi_n R_n^{MF}\, d\Omega + \int_{\Omega^F} \tilde{v}_a R^{\tilde{v}}\, d\Omega + \int_{\Omega^F} d_a R^d\, d\Omega + \int_{\Omega^S} T_a R^S\, d\Omega \tag{2.6}$$

As can be seen, the volume integrals contain the adjoint variables fields and their corresponding equation residuals. R^d stands for the residual of the Eikonal equation [15], that computes the field of distances d from the solid boundary, affecting the terms $\mathcal{P}^{\tilde{\nu}}$, $\mathcal{D}^{\tilde{\nu}}$ of the turbulence model:

$$R^d = \frac{\partial d}{\partial x_k}\frac{\partial d}{\partial x_k} = 0 \tag{2.7}$$

Ψ_n refer to the n$^{\text{th}}$ adjoint flow field in the fluid domain Ω^F (it is reminded that $n = 1,2,3,4$), while $\tilde{v}_a$ stands for the adjoint field of $\tilde{v}$ and d_a refers to the adjoint distance field, both defined in Ω^F. T_a is the adjoint temperature in the solid domain Ω^S. By definition [1], F is equal to F_{aug}. Differentiating eq. (2.6) with respect to the design variables b_i, leads to:

$$\frac{\delta F_{aug}}{\delta b_i} = \frac{\delta F}{\delta b_i} + \underbrace{\int_{\Omega^F} \Psi_n \frac{\delta R_n^{MF}}{\delta b_i}\, d\Omega}_{\mathcal{I}^{MF}} + \underbrace{\int_{\Omega^F} \tilde{v}_a \frac{\delta R^{\tilde{v}}}{\delta b_i}\, d\Omega}_{\mathcal{I}^{SA}} + \underbrace{\int_{\Omega^F} d_a \frac{\delta R^d}{\delta b_i}\, d\Omega}_{\mathcal{I}^{D}} + \underbrace{\int_{\Omega^S} T_a \frac{\delta R^S}{\delta b_i}\, d\Omega}_{\mathcal{I}^{S}} \tag{2.8}$$

Each of the four field integrals is to be developed separately in the following subsections. The total derivative of any flow quantity Φ at a grid node can be written as $\frac{\delta \Phi}{\delta b_i} = \frac{\partial \Phi}{\partial b_i} + \frac{\partial \Phi}{\partial x_k}\frac{\delta x_k}{\delta b_i}$, correlating the total and partial derivatives of Φ with the grid sensitivities $\frac{\delta x_k}{\delta b_i}$. According to [14], it can be derived that $\frac{\delta}{\delta b_i}\left(\frac{\partial \Phi}{\partial x_\ell}\right) = \frac{\partial}{\partial x_\ell}\left(\frac{\delta \Phi}{\delta b_i}\right) - \frac{\partial \Phi}{\partial x_k}\frac{\partial}{\partial x_\ell}\left(\frac{\delta x_k}{\delta b_i}\right)$, which is valid for both structured and unstructured grids, allowing the Gauss' divergence theorem to be applied to eq. (2.8). After the proper mathematical development, $\frac{\delta F_{aug}}{\delta b_i}$ will contain field and surface integrals, that include variations in the state variables, as well as integrals depending on grid sensitivities. A new set of partial differential equations, known as field adjoint equations (FAEs), along with the adjoint boundary conditions (ABCs) emerge when the multipliers of the variations are set to zero. The mathematical approach will be concluded with the derivation of the expression of the sensitivity derivatives (SDs) $\frac{\delta F}{\delta b_i}$. The procedure is called FI adjoint formulation, as the final expression for SDs contain the field variations of x_k [8].

2.3.1 Developing the mean-flow integral

Starting with the development of $\mathcal{I}^{MF}$, the substitution of R_n^{MF} from eq. (2.1), gives:

$$\mathcal{I}^{MF} = \underbrace{\int_{\Omega^F} \Psi_n \frac{\delta}{\delta b_i}\left(\frac{\partial f_{nk}^{inv}}{\partial x_k}\right) d\Omega}_{\mathcal{I}_{inv}^{MF}} \underbrace{- \int_{\Omega^F} \Psi_n \frac{\delta}{\delta b_i}\left(\frac{\partial f_{nk}^{vis}}{\partial x_k}\right) d\Omega}_{\mathcal{I}_{vis}^{MF}} \tag{2.9}$$

Using the divergence theorem, the inviscid term $\mathcal{I}_{inv}^{MF}$ is expanded into [14]:

[1] Considering that the primal equations should be satisfied, thus the residuals are equal to zero or $R_n^{MF} = R^{\tilde{v}} = R^d = R^S = 0$.

$$\mathcal{I}^{MF}_{inv} = \underbrace{\int_{S^F} \Psi_n n_k \frac{\delta f^{inv}_{nk}}{\delta b_i}\, dS}_{\rightarrow \mathcal{I}^B} \underbrace{- \int_{\Omega^F} A_{nmk} \frac{\partial \Psi_n}{\partial x_k} \frac{\delta U_m}{\delta b_i}\, d\Omega}_{\rightarrow FAE_{MF}} \underbrace{- \int_{\Omega^F} \Psi_n \frac{\partial f^{inv}_{nk}}{\partial x_\ell} \frac{\partial}{\partial x_k}\left(\frac{\delta x_\ell}{\delta b_i}\right) d\Omega}_{\rightarrow SD}$$

where $U = [\rho \quad \rho v_1 \quad \rho v_2 \quad \rho E]^T$ contains the conservative flow variables, E is the total energy per unit mass, and $A_{nmk} = \frac{\partial f_{nk} inv}{\partial U_m}$ the inviscid flux Jacobian matrix. The contribution of each term is denoted by an arrow, located beneath it. For instance, surface integrals are categorized under $\mathcal{I}^B$. Integrals including $\frac{\delta U_m}{\delta b_i}$ contribute to the field adjoint mean flow equations (FAE_{MF}), while those with grid sensitivities $\frac{\delta x_\ell}{\delta b_i}$ contribute to SDs.

Applying the divergence theorem to the viscid term $\mathcal{I}^{MF}_{vis}$ gives:

$$\mathcal{I}^{MF}_{vis} = \underbrace{- \int_{S^F} \Psi_n n_k \frac{\delta f^{vis}_{nk}}{\delta b_i}\, dS}_{\rightarrow \mathcal{I}^B} \underbrace{+ \int_{\Omega^F} \frac{\partial \Psi_n}{\partial x_k} \frac{\delta f^{vis}_{nk}}{\delta b_i}\, d\Omega}_{\mathcal{I}^{MF}_{vis,\Omega}} \underbrace{+ \int_{\Omega^F} \Psi_n \frac{\partial f^{vis}_{nk}}{\partial x_\ell} \frac{\partial}{\partial x_k}\left(\frac{\delta x_\ell}{\delta b_i}\right) d\Omega}_{\rightarrow SD}$$

Substituting f^{vis}_{nk} in $\mathcal{I}^{MF}_{vis,\Omega}$ gives:

$$\begin{aligned}
\mathcal{I}^{MF}_{vis,\Omega} = & \underbrace{\int_{\Omega^F} \left[\frac{\tau_{km}}{\mu + \mu_t}\left(\frac{\partial \Psi_{m+1}}{\partial x_k} + v_m \frac{\partial \Psi_4}{\partial x_k}\right) + \frac{\partial \Psi_4}{\partial x_k}\frac{\partial T}{\partial x_k}\frac{\partial \kappa^F}{\partial \mu}\right] \frac{\delta \mu}{\delta b_i}\, d\Omega - \int_{\Omega^F} \mathcal{K}_k \frac{\delta V_k}{\delta b_i}\, d\Omega}_{\rightarrow FAE_{MF}} \\
& \underbrace{+ \int_{\Omega^F} \left[\frac{\tau_{km}}{\mu + \mu_t}\left(\frac{\partial \Psi_{m+1}}{\partial x_k} + v_m \frac{\partial \Psi_4}{\partial x_k}\right) + \frac{\partial \Psi_4}{\partial x_k}\frac{\partial T}{\partial x_k}\frac{\partial \kappa^F}{\partial \mu_t}\right] \frac{\delta \mu_t}{\delta b_i}\, d\Omega}_{\mathcal{I}^{MF}_{\mu_t}} \\
& \underbrace{- \int_{\Omega^F} \left(\tau^{adj}_{km}\frac{\partial v_k}{\partial x_\ell} + q^{adj}_m \frac{\partial T}{\partial x_\ell}\right) \frac{\partial}{\partial x_m}\left(\frac{\delta x_\ell}{\delta b_i}\right) d\Omega}_{\rightarrow SD} \underbrace{+ \int_{S^F} \left(\tau^{adj}_{km} n_m \frac{\delta v_k}{\delta b_i} + q^{adj}_k n_k \frac{\delta T}{\delta b_i}\right) dS}_{\rightarrow \mathcal{I}^B}
\end{aligned}$$

For the sake of simplicity, indices F, S of T, q_{adj}, included in integrals are dropped. Arrays V, $\mathcal{K}$ are defined as:

$$V = [p \quad v_1 \quad v_2 \quad T^F]^T$$

$$\mathcal{K} = \left[0 \quad \frac{\partial \tau^{adj}_{1m}}{\partial x_k} - \frac{\partial \Psi_4}{\partial x_m}\tau_{1m} \quad \frac{\partial \tau^{adj}_{2m}}{\partial x_m} - \frac{\partial \Psi_4}{\partial x_m}\tau_{2m} \quad \frac{\partial q^{adj,F}_k}{\partial x_k}\right]^T$$

where the adjoint stresses and adjoint heat flux are:

$$\tau^{adj}_{km} = (\mu + \mu_t)\left(\frac{\partial \Psi_{k+1}}{\partial x_m} + \frac{\partial \Psi_{m+1}}{\partial x_k} - \frac{2}{3}\delta_{km}\frac{\partial \Psi_{\ell+1}}{\partial x_\ell} + \frac{\partial \Psi_4}{\partial x_k}v_m + \frac{\partial \Psi_4}{\partial x_m}v_k - \frac{2}{3}\delta_{km}\frac{\partial \Psi_4}{\partial x_\ell}v_\ell\right)$$

$$q^{adj,F}_k = \kappa^F \frac{\partial \Psi_4}{\partial x_k}$$

By differentiating μ with respect to T^F (based on Sutherland law [18]), variations $\frac{\delta\mu}{\delta b_i}$ can be taken into account. In addition, the differentiation of equation $\mu_t = \rho\tilde{\nu}f_{v1}$ or alternatively $\mu_t = \tilde{\mu}f_{v1}$ develops $\mathcal{I}^{MF}_{\mu_t}$ as follows:

$$\mathcal{I}^{MF}_{\mu_t} = \underbrace{\int_{\Omega^F}\left[\frac{\tau_{km}}{\mu+\mu_t}\left(\frac{\partial\Psi_{m+1}}{\partial x_k}+v_m\frac{\partial\Psi_4}{\partial x_k}\right)+\frac{\partial\Psi_4}{\partial x_k}\frac{\partial T}{\partial x_k}\frac{\partial\kappa^F}{\partial\mu_t}\right]\frac{\partial\mu_t}{\partial\tilde{\mu}}\frac{\delta\tilde{\mu}}{\delta b_i}\,d\Omega}_{\rightarrow FAE_{SA}} \tag{2.10}$$

2.3.2 Developing the Spalart-Allmaras integral

Substituting $R^{\tilde{v}}$ from eq. (2.4), $\mathcal{I}^{SA}$ integral takes the form:

$$\begin{aligned}\mathcal{I}^{SA} = &\underbrace{\int_{\Omega^F}\tilde{v}_a\frac{\delta}{\delta b_i}\left[\frac{\partial}{\partial x_k}(\rho v_k\tilde{\nu})\right]d\Omega}_{\mathcal{I}^{SA}_C}\\ &\underbrace{+\int_{\Omega^F}\tilde{v}_a\frac{\delta}{\delta b_i}\left[-\frac{\rho}{\sigma}\frac{\partial}{\partial x_k}\left[[\nu+(1+C_{b2})\tilde{\nu}]\frac{\partial\tilde{\nu}}{\partial x_k}\right]+\frac{\rho C_{b2}\tilde{\nu}}{\sigma}\frac{\partial}{\partial x_k}\left(\frac{\partial\tilde{\nu}}{\partial x_k}\right)\right]d\Omega}_{\mathcal{I}^{SA}_D}\\ &\underbrace{-\int_{\Omega^F}\tilde{v}_a\frac{\delta\mathcal{P}^{\tilde{\nu}}}{\delta b_i}d\Omega+\int_{\Omega^F}\tilde{v}_a\frac{\delta\mathcal{D}^{\tilde{\nu}}}{\delta b_i}d\Omega}_{\mathcal{I}^{SA}_S}\end{aligned} \tag{2.11}$$

It can be seen, the above equation can be simplified to $\mathcal{I}^{SA} = \mathcal{I}^{SA}_C + \mathcal{I}^{SA}_D + \mathcal{I}^{SA}_S$, where the $\mathcal{I}^{SA}_C$, $\mathcal{I}^{SA}_D$, $\mathcal{I}^{SA}_S$ contain the convection, diffusion, and source terms of the Spalart-Allmaras model, respectively. Using the divergence theorem, the first two integrals can further be analyzed as [22]:

$$\mathcal{I}_C^{SA} = \underbrace{-\int_{\Omega^F} \frac{\partial \tilde{\nu}_a}{\partial x_k} v_k \frac{\delta \tilde{\mu}}{\delta b_i}\, d\Omega}_{\rightarrow FAE_{SA}} \underbrace{-\int_{\Omega^F} \frac{\partial \tilde{\nu}_a}{\partial x_k} \frac{\delta v_k}{\delta b_i} \tilde{\mu}\, d\Omega}_{\rightarrow FAE_{MF}} \underbrace{+\int_{S^F} \tilde{\mu}\tilde{\nu}_a \frac{\delta v_k}{\delta b_i} n_k\, dS + \int_{S^F} v_k \tilde{\nu}_a \frac{\delta \tilde{\mu}}{\delta b_i} n_k\, dS}_{\rightarrow \mathcal{I}^B}$$
$$\underbrace{-\int_{\Omega^F} \tilde{\nu}_a \frac{\partial}{\partial x_\ell}(\rho v_k \tilde{\nu}) \frac{\partial}{\partial x_k}\left(\frac{\delta x_\ell}{\delta b_i}\right) d\Omega}_{\rightarrow SD}$$

$$\mathcal{I}_D^{SA} = \underbrace{\int_{\Omega^F} \tilde{\nu}_a \left[-\frac{\rho}{\sigma}\frac{\partial}{\partial x_k}\left[[\nu + (1+C_{b2})\tilde{\nu}]\frac{\partial \tilde{\nu}}{\partial x_k}\right] + \frac{\rho C_{b2}\tilde{\nu}}{\sigma}\frac{\partial}{\partial x_k}\left(\frac{\partial \tilde{\nu}}{\partial x_k}\right)\right]\frac{\delta \rho}{\delta b_i}\, d\Omega}_{\rightarrow FAE_{MF}}$$
$$\underbrace{+\int_{\Omega^F} \frac{\rho C_{b2}\tilde{\nu}_a}{\sigma}\frac{\partial}{\partial x_k}\left(\frac{\partial \tilde{\nu}}{\partial x_k}\right)\frac{\delta \tilde{\nu}}{\delta b_i}\, d\Omega}_{\rightarrow FAE_{MF}\,\&\,FAE_{SA}} \underbrace{+\int_{\Omega^F} \frac{\rho C_{b2}\tilde{\nu}\tilde{\nu}_a}{\sigma}\frac{\partial}{\partial x_\ell}\left(\frac{\partial \tilde{\nu}}{\partial x_k}\right)\frac{\partial}{\partial x_k}\left(\frac{\delta x_\ell}{\delta b_i}\right) d\Omega}_{\rightarrow SD}$$
$$\underbrace{+\int_{\Omega^F} \frac{\rho \tilde{\nu}_a}{\sigma}\frac{\partial}{\partial x_\ell}\left[[\nu + (1+C_{b2})\tilde{\nu}]\frac{\partial \tilde{\nu}}{\partial x_k}\right]\frac{\partial}{\partial x_k}\left(\frac{\delta x_\ell}{\delta b_i}\right) d\Omega}_{\rightarrow SD}$$
$$\underbrace{+\int_{\Omega^F} \frac{\rho C_{b2}\tilde{\nu}\tilde{\nu}_a}{\sigma}\frac{\partial}{\partial x_k}\left[\frac{\delta}{\delta b_i}\left(\frac{\partial \tilde{\nu}}{\partial x_k}\right)\right] d\Omega - \int_{\Omega^F} \frac{\rho \tilde{\nu}_a}{\sigma}\frac{\partial}{\partial x_k}\left[\frac{\delta}{\delta b_i}\left[[\nu + (1+C_{b2})\tilde{\nu}]\frac{\partial \tilde{\nu}}{\partial x_k}\right]\right] d\Omega}_{\mathcal{I}^{SA}_{grad\tilde{\nu}}}$$

The integrals containing variation in $\tilde{\mu}$ contribute to the field adjoint Spalart-Allmaras equation (FAE_{SA}), while those including variations in $\tilde{\nu}$ contribute to both FAE_{MF} and FAE_{SA}, given that $\frac{\delta \tilde{\nu}}{\delta b_i} = \frac{\partial \tilde{\nu}}{\partial \rho}\frac{\delta \rho}{\delta b_i} + \frac{\partial \tilde{\nu}}{\partial \tilde{\mu}}\frac{\delta \tilde{\mu}}{\delta b_i} = -\frac{\tilde{\nu}}{\rho}\frac{\delta \rho}{\delta b_i} + \frac{1}{\rho}\frac{\delta \tilde{\mu}}{\delta b_i}$. The remaining integral $\mathcal{I}^{SA}_{grad\tilde{\nu}}$ is expanded as follows:

$$\mathcal{I}^{SA}_{grad\tilde{\nu}} = \underbrace{\int_{\Omega^F} \frac{1}{\sigma}\frac{\partial \tilde{\nu}}{\partial x_k}\frac{\partial(\rho\tilde{\nu}_a)}{\partial x_k}\frac{\delta \nu}{\delta b_i}\, d\Omega}_{\rightarrow FAE_{MF}} \underbrace{+\int_{\Omega^F} \frac{1+C_{b2}}{\sigma}\frac{\partial \tilde{\nu}}{\partial x_k}\frac{\partial(\rho\tilde{\nu}_a)}{\partial x_k}\frac{\delta \tilde{\nu}}{\delta b_i}\, d\Omega}_{\rightarrow FAE_{MF}\,\&\,FAE_{SA}}$$
$$\underbrace{-\int_{\Omega^F} \frac{\partial}{\partial x_k}\left[\frac{1}{\sigma}[\nu + (1+C_{b2})\tilde{\nu}]\frac{\partial(\rho\tilde{\nu}_a)}{\partial x_k} - \frac{C_{b2}}{\sigma}\frac{\partial(\rho\nu\tilde{\nu}_a)}{\partial x_k}\right]\frac{\delta \tilde{\nu}}{\delta b_i}\, d\Omega}_{\rightarrow FAE_{MF}\,\&\,FAE_{SA}}$$
$$\underbrace{+\int_{S^F} \left[\frac{1}{\sigma}[\nu + (1+C_{b2})\tilde{\nu}]\frac{\partial(\rho\tilde{\nu}_a)}{\partial x_k} - \frac{C_{b2}}{\sigma}\frac{\partial(\rho\tilde{\nu}\tilde{\nu}_a)}{\partial x_k}\right]\frac{\delta \tilde{\nu}}{\delta b_i} n_k\, dS}_{\rightarrow \mathcal{I}^B}$$
$$\underbrace{-\int_{S^F} \frac{1}{\sigma}\rho\tilde{\nu}_a\frac{\delta}{\delta b_i}\left[[\nu + (1+C_{b2})\tilde{\nu}]\frac{\partial \tilde{\nu}}{\partial x_k}\right] n_k\, dS + \int_{S^F} \frac{C_{b2}}{\sigma}\rho\tilde{\nu}\tilde{\nu}_a\frac{\delta}{\delta b_i}\left(\frac{\partial \tilde{\nu}}{\partial x_k}\right) n_k\, dS}_{\rightarrow \mathcal{I}^B}$$
$$\underbrace{+\int_{\Omega^F} \left[\frac{1}{\sigma}[\nu + (1+C_{b2})\tilde{\nu}]\frac{\partial(\rho\tilde{\nu}_a)}{\partial x_k} - \frac{C_{b2}}{\sigma}\frac{\partial(\rho\tilde{\nu}\tilde{\nu}_a)}{\partial x_k}\right]\frac{\partial \tilde{\nu}}{\partial x_\ell}\frac{\partial}{\partial x_k}\left(\frac{\delta x_\ell}{\delta b_i}\right) d\Omega}_{\rightarrow SD}$$

Defining $\zeta = \sqrt{2W_{km}W_{km}}$ as the vorticity magnitude with $W_{km} = \frac{1}{2}\left(\frac{\partial v_k}{\partial x_m} - \frac{\partial v_m}{\partial x_k}\right)$, $\mathcal{P}^{\tilde{\nu}}$ and $\mathcal{D}^{\tilde{\nu}}$ are functions of ρ, ζ, d, and $\tilde{\mu}$, which means that:

$$\mathcal{I}_S^{SA} = \underbrace{\int_{\Omega^F} \tilde{v}_a \frac{\partial \mathcal{S}^{\tilde{\nu}}}{\partial \rho}\frac{\delta \rho}{\delta b_i}\, d\Omega}_{\rightarrow FAE_{MF}} + \underbrace{\int_{\Omega^F} \tilde{v}_a \frac{\partial \mathcal{S}^{\tilde{\nu}}}{\partial \tilde{\mu}}\frac{\delta \tilde{\mu}}{\delta b_i}\, d\Omega}_{\rightarrow FAE_{SA}} + \underbrace{\int_{\Omega^F} \tilde{v}_a \frac{\partial \mathcal{S}^{\tilde{\nu}}}{\partial d}\frac{\delta d}{\delta b_i}\, d\Omega}_{\rightarrow FAE_{D}} + \underbrace{\int_{\Omega^F} \tilde{v}_a \frac{\partial \mathcal{S}^{\tilde{\nu}}}{\partial \zeta}\frac{\delta \zeta}{\delta b_i}\, d\Omega}_{\mathcal{I}_\zeta^{SA}}$$

with $\mathcal{S}^{\tilde{\nu}} = \mathcal{D}^{\tilde{\nu}} - \mathcal{P}^{\tilde{\nu}}$. The field integral containing variations in d contribute to the field adjoint distance equation (FAE_D). Finally, $\mathcal{I}_\zeta^{SA}$ is developed as:

$$\mathcal{I}_\zeta^{SA} = \underbrace{-\int_{\Omega^F} \frac{\partial}{\partial x_m}\left[\tilde{v}_a \frac{\partial \mathcal{S}^{\tilde{\nu}}}{\partial \zeta}\frac{2}{\zeta}W_{km}\right]\frac{\delta v_k}{\delta b_i}\, d\Omega}_{\rightarrow FAE_{MF}} + \underbrace{\int_{\Omega^F} \tilde{v}_a \frac{\partial \mathcal{S}^{\tilde{\nu}}}{\partial \zeta}\frac{2}{\zeta}W_{km}\frac{\partial v_k}{\partial x_\ell}\frac{\partial}{\partial x_m}\left(\frac{\delta x_\ell}{\delta b_i}\right) d\Omega}_{\rightarrow SA}$$
$$+ \underbrace{\int_{S^F} \tilde{v}_a \frac{\partial \mathcal{S}^{\tilde{\nu}}}{\partial \zeta}\frac{2}{\zeta}W_{km}n_m\frac{\delta v_k}{\delta b_i}\, dS}_{\rightarrow \mathcal{I}^B}$$

2.3.3 Developing the Eikonal integral

Substituting R^d from eq. (2.7) gives:

$$\mathcal{I}^D = \underbrace{-\int_{\Omega^F} \frac{\partial}{\partial x_m}\left(2\frac{\partial d}{\partial x_m}d_a\right)\frac{\delta d}{\delta b_i}\, d\Omega}_{\rightarrow FAE_D} + \underbrace{\int_{S^F} 2\frac{\partial d}{\partial x_m}n_m d_a \frac{\delta d}{\delta b_i}\, dS}_{\rightarrow \mathcal{I}^B} \underbrace{- \int_{\Omega^F} 2\frac{\partial d}{\partial x_m}\frac{\partial d}{\partial x_\ell}d_a\frac{\partial}{\partial x_m}\left(\frac{\delta x_\ell}{\delta b_i}\right) d\Omega}_{\rightarrow SD}$$

2.3.4 Developing the heat conduction integral

From eq. (2.2), the integral $\mathcal{I}^S$ can be rewritten as:

$$\mathcal{I}^S = \underbrace{-\int_{S^S} T_a n_k \frac{\delta q_k}{\delta b_i}\, dS}_{\rightarrow \mathcal{I}^B} + \underbrace{\int_{\Omega^S} \frac{\partial T_a}{\partial x_k}\frac{\delta q_k}{\delta b_i}\, d\Omega}_{\mathcal{I}_q^S} + \underbrace{\int_{\Omega^S} T_a \frac{\partial q_k}{\partial x_\ell}\frac{\partial}{\partial x_k}\left(\frac{\delta x_\ell}{\delta b_i}\right) d\Omega}_{\rightarrow SD}$$

By definition, the adjoint heat fluxes in the solid domain are $q_k^{adj,S} = \kappa^S \frac{\partial T_a}{\partial x_k}$, which means that:

$$\mathcal{I}_q^S = \underbrace{\int_{\Omega^S} \frac{\partial T_a}{\partial x_k}\frac{\partial T}{\partial x_k}\frac{\delta \kappa^S}{\delta b_i}\, d\Omega - \int_{\Omega^S} \frac{\partial q_k^{adj}}{\partial x_k}\frac{\delta T}{\delta b_i}\, d\Omega}_{\rightarrow FAE_S} + \underbrace{\int_{S^S} q_k^{adj} n_k \frac{\delta T}{\delta b_i}\, dS}_{\rightarrow \mathcal{I}^B} \underbrace{- \int_{\Omega^S} q_k^{adj}\frac{\partial T}{\partial x_\ell}\frac{\partial}{\partial x_k}\left(\frac{\delta x_\ell}{\delta b_i}\right) d\Omega}_{\rightarrow SD}$$

2.3.5 Field Adjoint Equations (FAEs) and Adjoint Boundary Conditions (ABCs)

Based on the aforementioned mathematical analysis, by setting the multipliers of variations to zero, the resulting set of equations (i.e. FAE_{MF}, FAE_{SA}, FAE_D, FAE_S) is:

$$
\begin{aligned}
R_m^{\Psi} =& -A_{nmk}\frac{\partial \Psi_n}{\partial x_k} - \mathcal{K}_n\frac{\partial V_n}{\partial U_m} - \tilde{\mu}\frac{\partial \tilde{v}_a}{\partial x_k} \\
&+ \left[\frac{\tau_{km}}{\mu+\mu_t}\left(\frac{\partial \Psi_{m+1}}{\partial x_k} + v_m\frac{\partial \Psi_4}{\partial x_k}\right) + \frac{\partial \Psi_4}{\partial x_k}\frac{\partial T}{\partial x_k}\frac{\partial \kappa^F}{\partial \mu_t} + \frac{1}{\rho\sigma}\frac{\partial \tilde{v}}{\partial x_k}\frac{\partial(\rho\tilde{v}_a)}{\partial x_k}\right]\frac{\partial \mu}{\partial U_m} \\
&+ \tilde{v}_a\left[-\frac{\rho}{\sigma}\frac{\partial}{\partial x_k}\left[[\nu+(1+C_{b2})\tilde{v}]\frac{\partial \tilde{v}}{\partial x_k}\right] + \frac{\rho C_{b2}\tilde{v}}{\sigma}\frac{\partial}{\partial x_k}\left(\frac{\partial \tilde{v}}{\partial x_k}\right)\right] \\
&- \frac{C_{b2}}{\sigma}\tilde{v}\tilde{v}_a\frac{\partial}{\partial x_k}\left(\frac{\partial \tilde{v}}{\partial x_k}\right) - \frac{\nu}{\rho\sigma}\frac{\partial \tilde{v}}{\partial x_k}\frac{\partial(\rho\tilde{v}_a)}{\partial x_k} - \frac{\tilde{v}(1+C_{b2})}{\rho\sigma}\frac{\partial \tilde{v}}{\partial x_k}\frac{\partial(\rho\tilde{v}_a)}{\partial x_k} \\
&+ \frac{\tilde{v}}{\rho}\frac{\partial}{\partial x_k}\left[\frac{1}{\sigma}[\nu+(1+C_{b2})\tilde{v}]\frac{\partial(\rho\tilde{v}_a)}{\partial x_k} - \frac{C_{b2}}{\sigma}\frac{\partial(\rho\tilde{v}\tilde{v}_a)}{\partial x_k}\right] \\
&+ \tilde{v}_a\frac{\partial \mathcal{S}^{\tilde{v}}}{\partial \rho} - \frac{\partial}{\partial x_k}\left(\tilde{v}_a\frac{\partial \mathcal{S}^{\tilde{v}}}{\partial \zeta}\frac{2}{\zeta}W_{\ell k}\right) = 0 \\
R^{\tilde{v}_a} =& -v_k\frac{\partial \tilde{v}_a}{\partial x_k} - \frac{1}{\rho}\frac{\partial}{\partial x_k}\left[\frac{1}{\sigma}[\nu+(1+C_{b2})\tilde{v}]\frac{\partial(\rho\tilde{v}_a)}{\partial x_k} - \frac{C_{b2}}{\sigma}\frac{\partial(\rho\tilde{v}\tilde{v}_a)}{\partial x_k}\right] \\
&+ \frac{1+C_{b2}}{\rho\sigma}\frac{\partial \tilde{v}}{\partial x_k}\frac{\partial(\rho\tilde{v}_a)}{\partial x_k} + \frac{C_{b2}}{\sigma}\tilde{v}_a\frac{\partial}{\partial x_k}\left(\frac{\partial \tilde{v}}{\partial x_k}\right) \\
&+ \left[\frac{\tau_{km}}{\mu+\mu_t}\left(\frac{\partial \Psi_{m+1}}{\partial x_k} + v_m\frac{\partial \Psi_4}{\partial x_k}\right) + \frac{\partial \Psi_4}{\partial x_k}\frac{\partial T}{\partial x_k}\frac{\partial \kappa^F}{\partial \mu_t}\right]\frac{\partial \mu_t}{\partial \tilde{\mu}} + \tilde{v}_a\frac{\partial \mathcal{S}^{\tilde{v}}}{\partial \tilde{\mu}} = 0 \\
R^{d_a} =& -\frac{\partial}{\partial x_k}\left(2\frac{\partial d}{\partial x_k}d_a\right) + \tilde{v}_a\frac{\partial \mathcal{S}^{\tilde{v}}}{\partial d} = 0 \\
R^{T_a} =& -\frac{\partial}{\partial x_k}\left(\kappa^S\frac{\partial T_a}{\partial x_k}\right) + \frac{\partial T_a}{\partial x_k}\frac{\partial T^S}{\partial x_k}\frac{\partial \kappa^S}{\partial T^S} + \frac{\partial F}{\partial T^S} = 0
\end{aligned}
\tag{2.12}
$$

Only FAE_D depend on the adjoint distance d_a, therefore it is the last equation to be numerically solved.

Excluding the surface integrals with variations in $\tilde{v}$ and d, the rest of them form:

$$
\begin{aligned}
\mathcal{I}^B = &\int_{S^F}\left(\Psi_n n_k\frac{\delta f_{nk}^{inv}}{\delta b_i} - \Psi_n n_k\frac{\delta f_{nk}^{vis}}{\delta x_k} + \tau_{km}^{adj}n_m\frac{\delta v_k}{\delta b_i} + q_k^{adj}n_k\frac{\delta T}{\delta b_i}\right)dS \\
&- \int_{S^S}\left(T_a n_k\frac{\delta q_k}{\delta b_i} + q_k^{adj}n_k\frac{\delta T}{\delta b_i}\right)dS
\end{aligned}
\tag{2.13}
$$

I^B splits into the integrals $I^B_{I/O}$, over the inlet/outlet boundaries $S_{I/O}$ and I^B_W, over the solid boundaries (including the FSI region) S_W. The first one is developed as follows:

$$
\mathcal{I}^B_{I/O} = \int_{S_{I/O}}\left[\Psi_n A_{nmk}n_k\frac{\delta U_m}{\delta b_i} + (\tau_{km}^{adj}n_m - \Psi_4\tau_{km}n_m)\frac{\delta v_k}{\delta b_i} + q_k^{adj}n_k\frac{\delta T}{\delta b_i}\right]dS
$$

By eliminating the variations in the flow variables and ignoring those in viscous stresses and heat flux, the adjoint inlet/outlet equations arise:

$$\Psi_n A_{nmk} n_k \frac{\partial U_m}{\partial \mathcal{V}_j^{I/O}} + (\tau_{km}^{adj} n_m - \Psi_4 \tau_{km} n_m) \frac{\partial v_k}{\partial \mathcal{V}_j^{I/O}} + q_k^{adj} n_k \frac{\partial T}{\partial \mathcal{V}_j^{I/O}} + \frac{\partial F}{\partial \mathcal{V}_j^{I/O}} = 0 \quad (2.14)$$

with $\mathcal{V}^{I/O}$ standing for any flow variable extrapolated to boundary $S_{I/O}$ from the interior of the fluid domain Ω^F. Specifically, $\mathcal{V}_j^I$ is the velocity magnitude for the inlet and V_j^O are the outgoing Riemann variables. Imposing the no-slip condition on eq. (2.13), the integral over S_W gives:

$$\begin{aligned}\mathcal{I}_W^B = &\int_{S_W^F} \Psi_{m+1} n_m \frac{\delta p}{\delta b_i}\, dS - \int_{S_W^F} \Psi_{m+1} n_k \frac{\delta \tau_{km}}{\delta b_i}\, dS - \int_{S_W^F} \Psi_4 \frac{\delta (q_k n_k)}{\delta b_i}\, dS + \int_{S_W^F} q_k^{adj} n_k \frac{\delta T}{\delta b_i}\, dS \\ &- \int_{S_W^S} T_a \frac{\delta (q_k n_k)}{\delta b_i}\, dS + \int_{S_W^S} q_k^{adj} n_k \frac{\delta T}{\delta b_i}\, dS + \underbrace{\int_{S_W^F} \Psi_4 q_k \frac{\delta n_k}{\delta b_i}\, dS + \int_{S_W^S} T_a q_k \frac{\delta n_k}{\delta b_i}\, dS}_{\to SD}\end{aligned}$$

The surface integrals, including $\frac{\delta p}{\delta b_i}$, $\frac{\delta \tau_{km}}{\delta b_i}$ are eliminated by satisfying the adjoint no-slip condition $\Psi_2 = \Psi_3 = 0$. On the same pattern, the adjoint FSI conditions ($\Psi_4 = T_a$ and $q_k^{adj,F} n_k^F = -q_k^{adj,S} n_k^S$) eliminate the surface integrals with variations in heat flux or T. Lastly, the surfaces integrals with $\frac{\delta \tilde{\nu}}{\delta b_i}$, $\frac{\delta d}{\delta b_i}$ are eliminated by setting $\tilde{v}_a = d_a = 0$ over the boundaries of Ω^F.

2.3.6 Expression for SDs

Following the definition of the adjoint equations and their corresponding boundary conditions, the sensitivity derivatives (SDs) are computed via:

$$\frac{\delta F}{\delta b_i} = \mathcal{I}_{MF}^{SD} + \mathcal{I}_{SA}^{SD} + \mathcal{I}_D^{SD} + \mathcal{I}_S^{SD} \quad (2.15)$$

where

$$\begin{aligned}\mathcal{I}_{MF}^{SD} = &- \int_{\Omega^F} \left[\Psi_n \left(\frac{\partial f_{nk}^{inv}}{\partial x_\ell} - \frac{\partial f_{nk}^{vis}}{\partial x_\ell} \right) - \tau_{km}^{adj} \frac{\partial v_m}{\partial x_\ell} - q_k^{adj} \frac{\partial T}{\partial x_\ell} \right] \frac{\partial}{\partial x_k} \left(\frac{\delta x_\ell}{\delta b_i} \right) d\Omega + \int_{S_W^F} \Psi_4 q_k \frac{\delta n_k}{\delta b_i}\, dS \\ \mathcal{I}_{SA}^{SD} = &- \int_{\Omega^S} \tilde{\nu}_a \frac{\partial}{\partial x_\ell} (\rho v_k \tilde{\nu}) \frac{\partial}{\partial x_k} \left(\frac{\delta x_\ell}{\delta b_i} \right) d\Omega \\ &+ \int_{\Omega^F} \frac{\rho \tilde{\nu}_a}{\sigma} \left[\frac{\partial}{\partial x_\ell} \left[[\nu + (1 + C_{b2}) \tilde{\nu}] \frac{\partial \tilde{\nu}}{\partial x_k} \right] + C_{b2} \tilde{\nu} \frac{\partial}{\partial x_\ell} \left(\frac{\partial \tilde{\nu}}{\partial x_k} \right) \right] \frac{\partial}{\partial x_k} \left(\frac{\delta x_\ell}{\delta b_i} \right) d\Omega \\ &+ \int_{\Omega^F} \left[\frac{1}{\sigma} [\nu + (1 + C_{b2}) \tilde{\nu}] \frac{(\partial \rho \tilde{\nu}_a)}{\partial x_k} - \frac{C_{b2}}{\sigma} \frac{\partial (\rho \tilde{\nu} \tilde{\nu}_a)}{\partial x_k} \right] \frac{\partial \tilde{\nu}}{\partial x_\ell} \frac{\partial}{\partial x_k} \left(\frac{\delta x_\ell}{\delta b_i} \right) d\Omega \\ &- \int_{\Omega^F} \tilde{\nu}_a \frac{\partial \mathcal{S}^{\tilde{\nu}}}{\partial \zeta} \frac{2}{\zeta} W_{km} \frac{\partial v_k}{\partial x_m} \frac{\partial}{\partial x_m} \left(\frac{\delta x_\ell}{\delta b_i} \right) d\Omega \\ \mathcal{I}_D^{SD} = &- \int_{\Omega^S} 2 \frac{\partial d}{\partial x_m} \frac{\partial d}{\partial x_\ell} d_a \frac{\partial}{\partial x_m} \left(\frac{\delta x_\ell}{\delta b_i} \right) d\Omega \\ \mathcal{I}_S^{SD} = &\int_{\Omega^S} \left(T_a \frac{\partial q_k}{\partial x_\ell} - q_k^{adj} \frac{\partial T}{\partial x_\ell} \right) \frac{\partial}{\partial x_k} \left(\frac{\delta x_\ell}{\delta b_i} \right) d\Omega + \int_{S_W^S} T_a q_k \frac{\delta n_k}{\delta b_i}\, dS\end{aligned} \quad (2.16)$$

2.4 PUMA Software

All the necessary computations were conducted using PUMA, developed by the Parallel CFD & Optimization Unit of the National Technical University of Athens (PCOpt/NTUA) [2]. It is a GPU-accelerated software, including solvers for the RANS equations, heat conduction equation, and a variety of turbulence model equations. In addition, PUMA includes an adjoint solver, based on the continuous approach for the solution of aerodynamic and CHT optimization problems. The data transfer among GPUs on different nodes is achieved using the MPI protocol.

The so-called primal and adjoint equations are discretized using unstructured grids for the fluid and solid domains, following the vertex-centered finite-volume approach. The 3-stage Runge-Kutta scheme with residual smoothing is employed to solve the steady-state equations in pseudo-time. At each Runge-Kutta stage, the computed residuals are smoothed using the spectral radii technique. For the computation of the spatial derivatives, the Green-Gauss method is used. The 2^{nd} order Jameson-Schmidt-Turkel (JST) discretization scheme [7] is applied on the transport terms of the RANS equations, while the 1^{st} order upwind Roe scheme [16] is used to discretize the turbulence model convection fluxes. The heat conduction equation is also discretized using vertex-centered finite volumes and solved with the Gauss-Seidel method. The cooling holes' walls act as boundaries on which PUMA imposes heat flux conditions, where the bulk temperature and the constant heat transfer coefficient need to be defined. The algorithm does not use wall functions in the modeling, as the grid density is considered to be sufficiently high near the solid boundaries.

The computational procedure starts with the generation of the initial geometry including both the airfoil shape and the geometric features of the cooling configuration system. The algorithm solves the primal and then the adjoint problem, computing the sensitivity derivatives. Information on the primal and the adjoint solvers, highlighting the function of the coupling scheme, is presented in section 2.4.2. The MMA method is used (section 2.4.3) to update the design variables and, consequently, the cooling holes' displacements. Then, with the updated geometry, the new grid in the solid domain is generated using the advancing front method. The properties of the airfoil shape and fluid domain's grid do not change during the optimization. The procedure is repeated till the convergence criteria be met. The aforementioned process is summarized in fig. 2.2.

2.4.1 Grid Properties

The computational domain is generated from 16 curves, i.e. the inlet, outlet, and periodic boundaries, the pressure and suction side, and the 10 cooling holes. During the optimization, only the holes' positions can be modified. The design variables vector consists of the hole centers, i.e. $\boldsymbol{b} = [x_{c1} \quad y_{c1} \quad x_{c2} \quad y_{c2} \quad \dots \quad x_{cn} \quad y_{cn}]^T$ with n the holes' total number. After each optimization cycle, due to changes in the cooling hole's positions, the grid inside the blade is generated from scratch, while that in the fluid domain remains intact, as there is no change in the airfoil shape. The displacement of the points forming the perimeter of each hole depends on the coordinates of the hole center itself. For instance, the perimeter points $\boldsymbol{x_{per2}} = (x_\ell, y_\ell)$ of hole no. 2 (ℓ is the number of the parameter points) are transformed via $\boldsymbol{x_{per2}} = \frac{\delta x_2}{\delta b}\boldsymbol{b}$ with

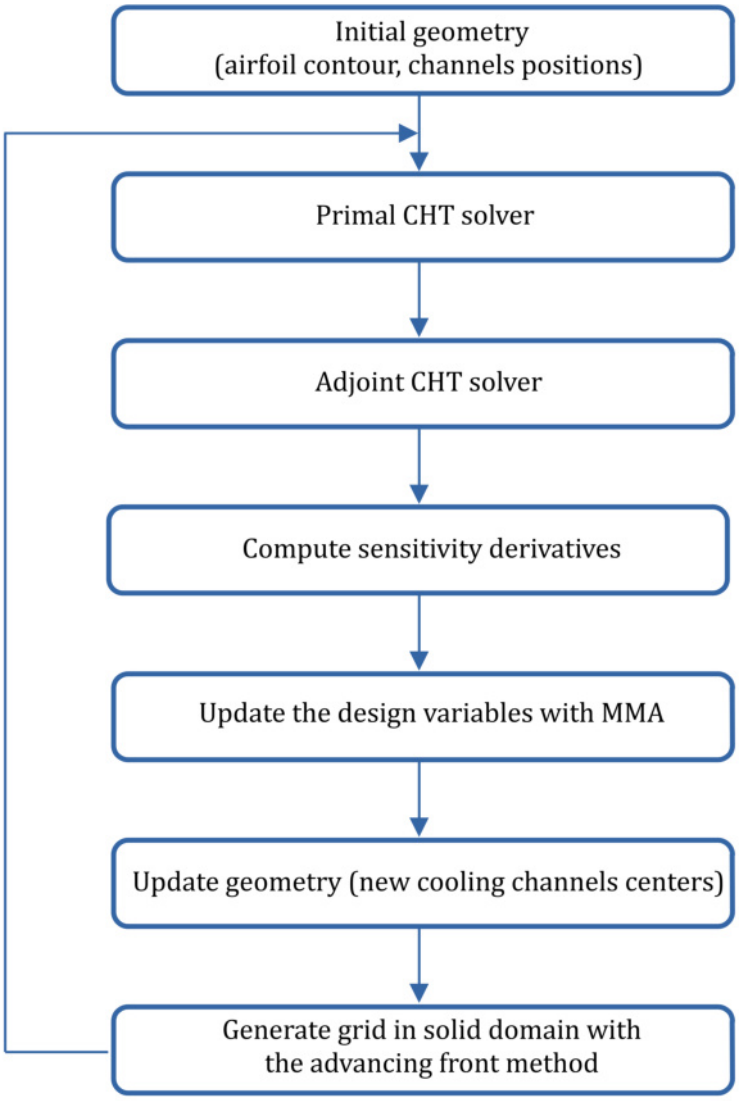

FIGURE 2.2: Flow chart of an optimization cycle.

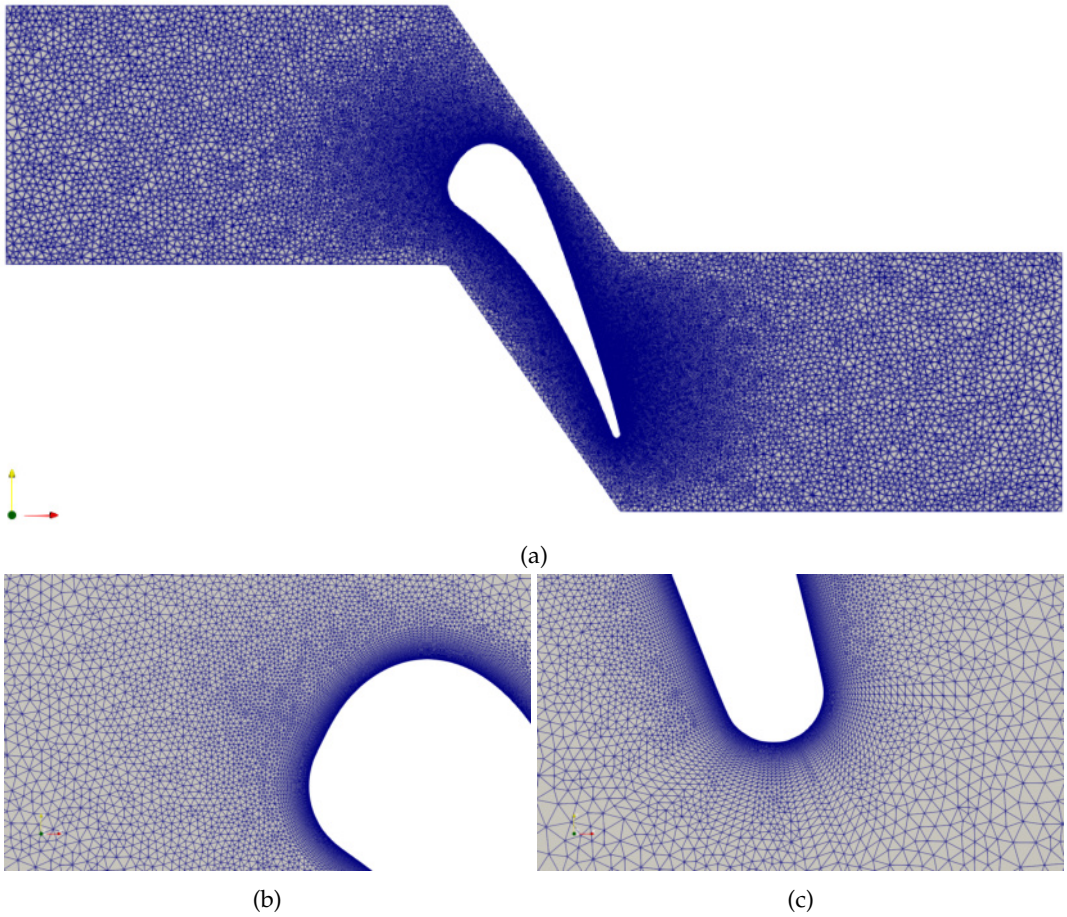

(a)

(b) (c)

FIGURE 2.3: Grid illustration in the (a) fluid domain (b) leading edge (c) trailing edge.

the cooling system grid sensitivities vector [2] being $\frac{\delta x_2}{\delta b} = [0 \quad 0 \quad 1 \quad 1 \quad ... \quad 0 \quad 0]^T$. The PUMA software uses the advancing front method [9] to triangulate the computational solid domain Ω^S, starting from the boundaries and then progressing inwards, to generate the unstructured grid. To better handle the large spatial derivative near the solid boundaries, the grid is structured-like in that region, as illustrated in figs. 2.3 and 2.4. Regarding the baseline geometry, the total number of nodes in the fluid and solid domains is 190124 and 91188 respectively.

2.4.2 Coupling Scheme

The flow and heat transfer solvers for the primal problem are loosely coupled. The heat transfer solver computes the temperature field values in the solid domain Ω^S and then imposes them as boundary conditions on the flow solver. The flow solver calculates the heat fluxes in the FSI boundary and feeds them back to the heat transfer solver. That can be achieved by integrating the energy equation $R_4^{MF} = 0$ on the adjacent finite volumes Ω^F for each node i to consider the heat fluxes crossing the interface between it and its neighbour-nodes. The process is repeated until the convergence criteria are met. The communication of the temperature fields along the FSI region is achieved using the fixed-point iteration method, meaning

[2] For visualization reasons, a turning angle may be introduced. In that case, as in the present thesis where the angle equals 70°, the vector changes into $\frac{\delta x_2}{\delta b} = [0 \quad 0 \quad \cos 70° \quad \sin 70° \quad ... \quad 0 \quad 0]^T$.

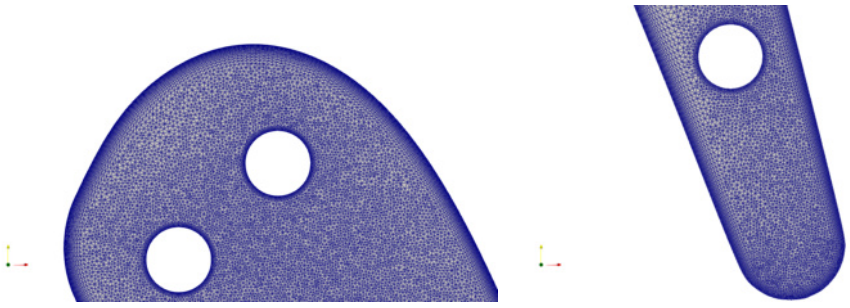

(a) (b)

FIGURE 2.4: Grid illustration in the solid domain near the (a) leading (b) trailing edge.

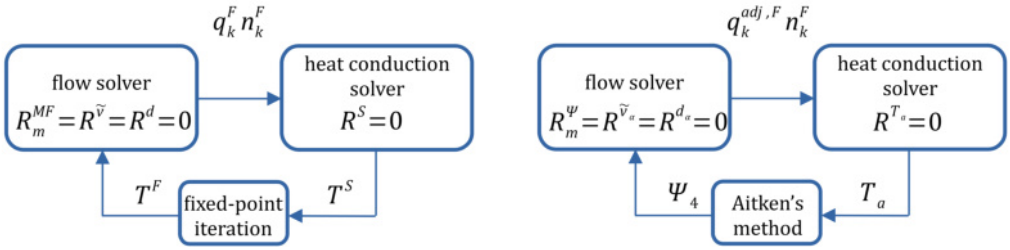

(a) (b)

FIGURE 2.5: Coupling scheme of the (a) primal and (b) adjoint CHT solver.

that $T_{n+1}^F = T_n^S$ for the n^{th} iteration. The aforementioned method was also followed in the case of the adjoint problem, the only difference being the coupling is achieved with Aitken's dynamic relaxation formula, named after Alexander Aitken [1]. The numerical method accelerates the rate of convergence of a sequence, using the values from three consecutive iterations. With $R_n = T_n^S - T_n^F$, the relaxation factor $a_{n+1} = a_n \left(1 - \frac{(R_n - R_{n-1})R_n}{||R_n - R_{n-1}||_2}\right)$ is updated at each iteration, using the residuals from the 2 last iterations. The temperature field is updated via $T_{n+1}^F = a_{n+1}T_n^S + (1 - a_{n+1})T_n^F$. Figure 2.5 illustrates the coupling procedures for the primal and adjoint problem.

2.4.3 Method of Moving Asymptotes

The gradient-based method of moving asymptotes (MMA) is used [19], to conclude the computational procedure. Its function is to obtain the expressions of SDs generated by the continuous adjoint solver and then optimize the objective function $f_0(\boldsymbol{b})$, taking into account both the inequality constraints $f_i(\boldsymbol{b}) \leq \hat{f}_i$ (i=1, 2, ... m) and the bounds subjected to the design variables $\boldsymbol{b} = [b_1 \quad b_2 \quad ... \quad b_n]^T$. In the present thesis, the constraints are related to the displacement of the cooling holes. The design variables along with their geometrical constraints are detailed in chapter 4.

The algorithm's approach is based on an iterative scheme of generating and solving a sequence of explicit sub-problems. Starting with the initial vector $\boldsymbol{b}^0$, the values of $f_i(\boldsymbol{b}^k)$ and $\nabla f_i(\boldsymbol{b}^k)$ (i=0, 1, 2, ... m) are calculated in k^{th} iteration. m, n denote the number of inequality constraints and design variables, respectively. After that, a sub-problem P^k is generated, its solution being the next iteration point $\boldsymbol{b}^{k+1}$, until

the convergence criteria are fulfilled. With L_j^k, U_j^k being the lower and upper bounds of the design variables, i.e. $L_j^k < b_j^k < U_j^k$, functions f_i^k are defined as:

$$f_i^k(\boldsymbol{b}) = r_i^k + \sum_{j=1}^{n} \left(\frac{p_{ij}^k}{U_j^k - b_j} + \frac{q_{ij}^k}{b_j - L_j^k} \right)$$

where

$$p_{ij}^k = \begin{cases} (U_j^k - b_j^k)^2 \frac{\partial f_i}{\partial b_j}, & \text{if} \quad \frac{\partial f_i}{\partial b_j} > 0 \\ 0, & \text{if} \quad \frac{\partial f_i}{\partial b_j} \leq 0 \end{cases}$$

$$q_{ij}^k = \begin{cases} 0, & \text{if} \quad \frac{\partial f_i}{\partial b_j} \geq 0 \\ -(b_j^k - L_j^k)^2 \frac{\partial f_i}{\partial b_j}, & \text{if} \quad \frac{\partial f_i}{\partial b_j} < 0 \end{cases}$$

$$r_i^k = f_i(\boldsymbol{b}^k) - \sum_{j=1}^{n} \left(\frac{p_{ij}^k}{U_j^k - b_j} + \frac{q_{ij}^k}{b_j - L_j^k} \right)$$

with $f_i^k(\boldsymbol{b}^k) = f_i(\boldsymbol{b}^k)$ and $\frac{\partial f_i^k}{\partial b_j} = \frac{\partial f_i}{\partial b_j}$ at $\boldsymbol{b} = \boldsymbol{b}^k$. f_i is a convex function since $p_{ij}^k, q_{ij}^k \geq 0$ thus the second derivatives are:

$$\frac{\partial^2 f_i^k}{\partial b_j^2} = \begin{cases} 2\frac{\partial f_i}{\partial x_j} \frac{1}{U_j^k - b_j^k}, & \text{if} \quad \frac{\partial f_i}{\partial b_j} > 0 \\ -2\frac{\partial f_i}{\partial b_j} \frac{1}{b_j^k - L_j^k}, & \text{if} \quad \frac{\partial f_i}{\partial b_j} < 0 \end{cases}$$

$$\frac{\partial^2 f_i^k}{\partial b_j \partial b_\ell} = 0, \quad \text{if} \quad j \neq \ell$$

The new sub-problem P^k is defined, involving the approximate versions of f_i^k. The aim is to minimize the function $\sum_{j=1}^{n} \left(\frac{p_{0j}^k}{U_j^k - b_j} + \frac{q_{0j}^k}{b_j - L_j^k} \right) + r_0^k$ with the new constraints being $\sum_{j=1}^{n} \left(\frac{p_{ij}^k}{U_j^k - b_j} + \frac{q_{ij}^k}{b_j - L_j^k} \right) + r_i^k \leq \hat{f}_i$ for $i = 1, 2, ..., n$ and $\max(b_j, \alpha_j^k) \leq b_j \leq \min(b_j, \beta_j^k)$ for $j = 1, 2, ..., m$. L_j^k, U_j^k are called moving asymptotes, although they may have fixed values based on the optimization problem. α_j^k, β_j^k are limits with $L_j^i k < \alpha_j^k < x_j^k < \beta_j^k < U_j^k$.The solution to the problem P_k is the input $\boldsymbol{b}^{k+1}$, used to the next iteration.

3 Validation of the Solver and Optimization Set-Up

The geometry of C3X turbine blade along with the cooling holes configuration are illustrated in fig. 3.1, based on [6]. The blade's axial chord is 7.816 cm, while its material is ASTM type 310 stainless steel with density $\rho^S = 7900$ kg/m^3 and heat capacity $C^S = 586.15$ J/(kgK). The material's heat conductivity varies linearly with the solid temperature as $\kappa^S = 6.811 + 0.020716T^S$.

In the present thesis, the optimization will be carried out for the flow conditions of 5 different test-cases, namely those identified as no. 108, 111, 113, 157, and 158. The flow conditions of the cases are presented in table 3.3, where the total inlet pressure p_{t1} and temperature T_{t1}, turbulence intensity T_{u1}, outlet pressure p_2, and outlet isotropic Mach number $M_{2,is}$ are recorded. Test-case 111 deals with a transonic flow. The inlet flow angle is $a_1 = 0$ in all cases. Before starting the optimization process, a series of runs were performed to compare with the experimental data from the literature [6]. Based on the 2-D analysis, a procedure was followed, in which a constant heat transfer coefficient is assumed for each cooling hole. The coefficient values depend on the mean coolant temperature T_C and coolant flow mass $\dot{m}_C$ per hole, given in tables 3.4 to 3.8. The cooling holes are modeled as circular cross-section smooth pipes. Utilizing the aforementioned data, the Reynolds number $\mathrm{Re}_D = \frac{4\dot{m}_C}{\pi D\mu}$ and the Nusselt number $\mathrm{Nu}_D = 0.022\mathrm{Cr}\,\mathrm{Pr}^{0.5}\mathrm{Re}_D^{0.8}$ are calculated. D is the hole diameter and Cr is a correction for a fully developed thermal boundary layer to account for thermal entrance region effects, both given in table 3.1. It has already been mentioned that Pr = 0.72. The coolant's viscosity μ is computed via the Sutherland law $\mu = \mu_{ref}\left(\frac{T_C}{T_{ref}}\right)^{1.5}\frac{T_{ref}+C}{T_C+C}$, with $C = 110.56$ K, $T_{ref} = 273.11$ K and $\mu_{ref} = 1.7894 \cdot 10^{-5}$Pa $\cdot$ s. With the coolant thermal conductivity computed via $\kappa_C = \frac{C_p\mu}{\mathrm{Pr}}$, the heat transfer coefficient is finally defined as $h_C = \frac{\kappa_C \mathrm{Nu}_D}{D}$. The parameters T and h_C are assigned to the heat flux condition, imposed on the hole boundaries. Given the geometry of the airfoil shape, the area within which the holes

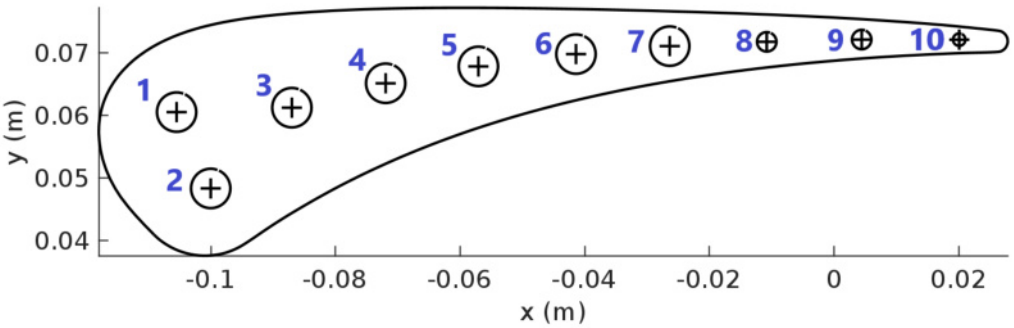

FIGURE 3.1: C3X geometry and cooling hole positions.

TABLE 3.1: Cooling holes geometric characteristics, based on coordinate system of fig. 3.1.

no.	x (m)	y (m)	D (mm)	Cr
1	-0.1055	0.0605	6.30	1.118
2	-0.1000	0.0483	6.30	1.118
3	-0.8701	0.0612	6.30	1.118
4	-0.7196	0.0651	6.30	1.118
5	-0.5708	0.0678	6.30	1.118
6	-0.4142	0.0698	6.30	1.118
7	-0.2638	0.0711	6.30	1.118
8	-0.1081	0.0718	3.10	1.056
9	0.4528	0.0721	3.10	1.056
10	0.2007	0.0721	1.98	1.025

TABLE 3.2: Maximum displacement of the cooling holes centers along the x and y directions.

no.	x (mm)	y (mm)
1	$\pm$ 5	$\pm$ 2
2	-5, 4	$\pm$ 3
3	$\pm$ 3	$\pm$ 8
4	$\pm$ 3	$\pm$ 5
5	$\pm$ 3	$\pm$ 3
6	$\pm$ 3	$\pm$ 1
7	$\pm$ 3	$\pm$ 0.5
8	$\pm$ 5	$\pm$ 0.5
9	$\pm$ 5	-0.2, +0.5
10	$\pm$ 5	$\pm$ 0.3

can be displaced is limited. Upper and lower bounds have been defined, to prevent any overlap between the holes themselves and the airfoil sides. The maximum allowed displacements of the hole centers along the x and y directions are given in table 3.2.

Figures 3.2 to 3.4 depict the pressure p, temperature T and heat transfer coefficient h fields along the FSI region, in comparison with the experimental data, using the Spalart-Allmaras (S-A) turbulence model. The distance is normalized with the blade's axial chord ($x/c < 0$ refers to the pressure and $x/c > 0$ to the suction side), with the pressure reference value p_{ref} being equal to the inlet total pressure p_{t1}, which is different for each case (table 3.3). The remaining reference values are $T_{ref} = 811$ K and $h_{ref} = 1135$ W/(m^{2}K). It should be noted that the software returns the heat flux q_i for each point i on the airfoil, which is then divided by $\Delta T_i = T_{t1} - T_i$ to give the heat transfer coefficient values $h_i = \frac{q_i}{\Delta T_i}$. In the transonic test-case 111, the experiment predicts a rather weak shock wave at $x/c \simeq 0.6$ (suction side) and at the trailing edge (pressure side), due to the small number of measurements. The two regions are indicated by a steep drop in the pressure distribution figure. There is also a decrease in the temperature and heat transfer coefficient at the point, where the

TABLE 3.3: Flow conditions for the five examined test-cases.

Case	**108**	**111**	**113**	**157**	**158**
p_{t1} (Pa)	319500	307989	323157	413272	243700
T_{t1} (K)	786	796	781	818	808
$T_{u1}(\%)$	6.5	8.3	8.3	8.3	8.3
p_2 (Pa)	188900	153339	193145	247004	142530
$M_{2,is}$	0.90	1.05	0.89	0.89	0.91

shock wave occurs. In the case of the transonic flow, higher temperatures are measured along the airfoil, as the coolant mass flow is decreased table 3.5, compared to the remaining cases. There is a good agreement between the solver's results and the experimental data, except for the suction side region near the leading edge, where an overestimation of T and h is observed. Since none of the analysis and optimization runs is using a transition model, the boundary layer is considered fully turbulent along the airfoil and the existence of the laminar boundary layer is ignored, by the Spalart-Allmaras model, in the first half of the airfoil's suction side. In that region, there is a transition delay of the boundary layer. It is for this reason that, the experimental data illustrate a dip in the temperature and the heat transfer coefficient distributions in contrast to the solver's results, in which the laminar boundary layer has not been taken into account, meaning that T and h have been taken overestimated values. The dip region in the experiment is followed by a sharp increase (especially in the case of the heat transfer coefficient) indicating the boundary layer's transition point from laminar to turbulent. It is clear that no transition point is illustrated in the solver's results, given that the flow is modeled as fully turbulent along the airfoil. Although a transition model is necessary for the correction of the results near the leading edge, it does not seem to have any influence on the temperature distribution on the back of the airfoil, where $T^S_{\max}$ occurs. In addition, it is obvious that the inclusion of a transition model in the mathematical approach would lead to a lower temperature in the laminar boundary layer's region, approaching the values measured in the experiment, and hence not surpassing the maximum solid temperature in the trailing edge. Nevertheless, the temperature gap between the pressure and suction side would be decreased, leading to a change in the front holes' displacement, as they tend to move toward the region with the highest T^S. Even in this case, as will be deducted in the following chapters, there is no change in the value of maximum temperature, as the contribution of the front holes' displacement to the minimization of $T^S_{\max}$ is negligible. Consequently, the absence of a transition model can be tolerated in the context of the minimization of $T^S_{\max}$.

TABLE 3.4: Cooling holes properties for test-case 108, obtained from [6].

no.	T_C (K)	$\dot{m}_C$ (g/s)	h_C (W/m^{2}K)
1	346.07	22.7	2119.03
2	345.70	23.9	1882.84
3	338.00	22.5	1788.90
4	338.47	23.7	1865.17
5	331.73	23.6	1854.11
6	360.85	15.9	1366.51
7	340.69	23.4	1847.80
8	358.87	7.98	2663.00
9	396.78	5.29	1942.00
10	437.39	2.89	2639.02

TABLE 3.5: Cooling holes properties for test-case 111, obtained from [6].

no.	T_C (K)	$\dot{m}_C$ (g/s)	h_C (W/m^{2}K)
1	415.81	7.71	780.32
2	417.75	6.21	656.71
3	399.15	6.20	651.86
4	407.29	6.58	685.48
5	384.36	6.61	682.71
6	444.68	6.86	717.26
7	401.55	6.36	665.82
8	417.18	2.25	986.62
9	486.10	1.37	677.71
10	539.68	0.771	945.14

TABLE 3.6: Cooling holes properties for test-case 113, obtained from [6].

no.	T_C (K)	$\dot{m}_C$ (g/s)	h_C (W/m^{2}K)
1	354.02	21.3	1722.37
2	353.06	22.8	1818.10
3	344.81	22.5	1793.48
4	345.42	23.8	1882.56
5	339.51	24.2	1897.33
6	366.62	24.8	1954.10
7	347.27	22.9	1820.60
8	365.88	7.84	2632.15
9	400.68	5.04	1870.66
10	442.16	2.57	2406.14

TABLE 3.7: Cooling holes properties for test-case 157, obtained from [6].

no.	T_C (K)	$\dot{m}_C$ (g/s)	h_C (W/m^{2}K)
1	352.14	22.2	1779.13
2	354.54	22.1	1774.26
3	345.62	21.8	1749.23
4	346.72	22.8	1813.87
5	340.70	22.5	1790.73
6	366.21	22.5	1807.47
7	351.48	21.6	1740.13
8	376.24	7.44	2533.36
9	406.97	4.77	1793.78
10	446.69	2.56	2402.04

TABLE 3.8: Cooling holes properties for test-case 158, obtained from [6].

no.	T_C (K)	$\dot{m}_C$ (g/s)	h_C (W/m^{2}K)
1	358.14	16.7	1419.92
2	359.37	17.4	1468.00
3	349.97	14.8	1284.39
4	351.51	16.5	1402.37
5	342.56	17.5	1464.16
6	371.85	16.5	1413.94
7	351.85	16.1	1374.92
8	385.96	5.5	2000.80
9	413.22	3.49	1403.64
10	454.87	1.71	1745.60

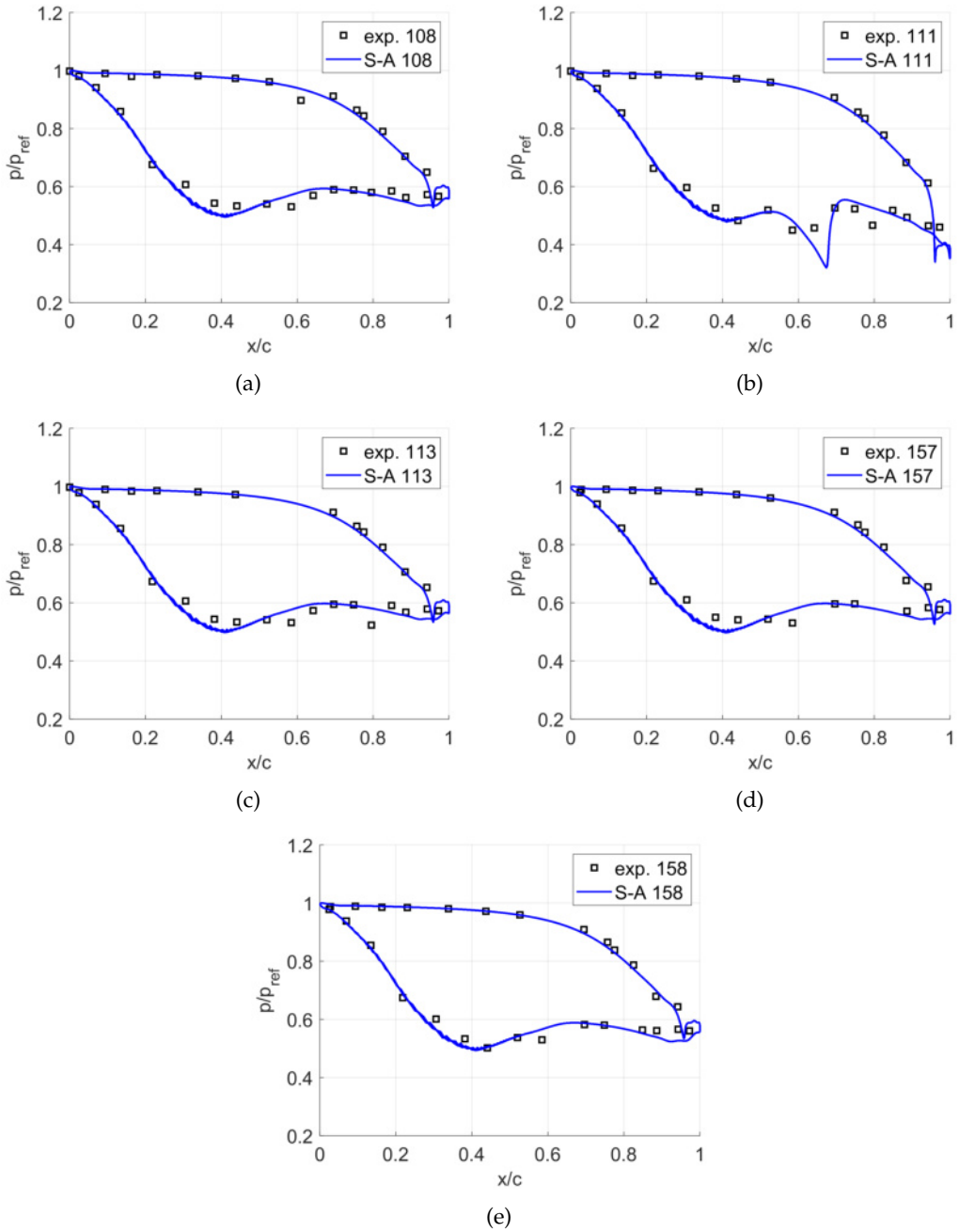

FIGURE 3.2: Comparison of the computed pressure distribution and the experimental data [6], along the blade airfoil contour.

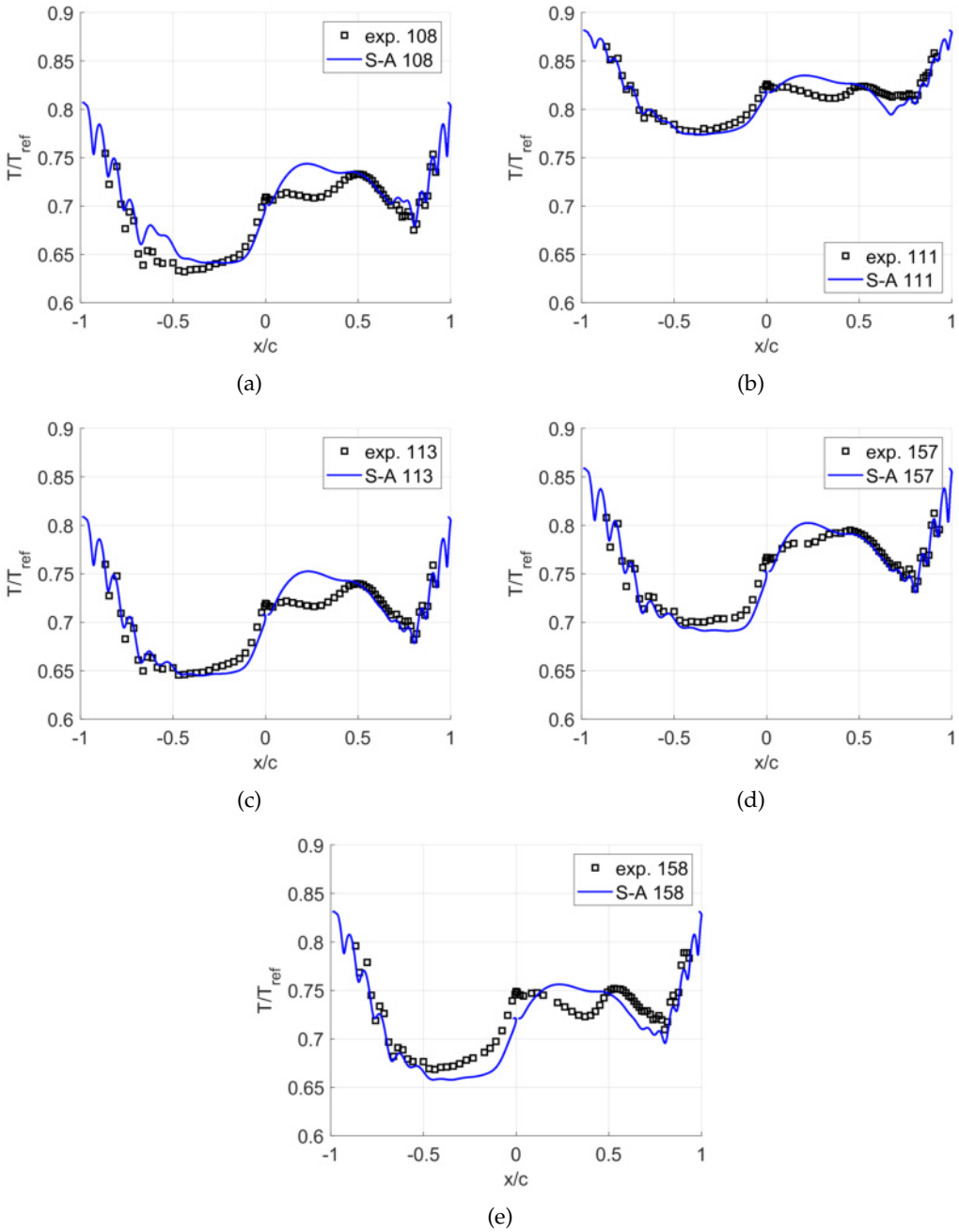

FIGURE 3.3: Comparison of the computed temperature distribution and the experimental data [6], along the blade airfoil contour.

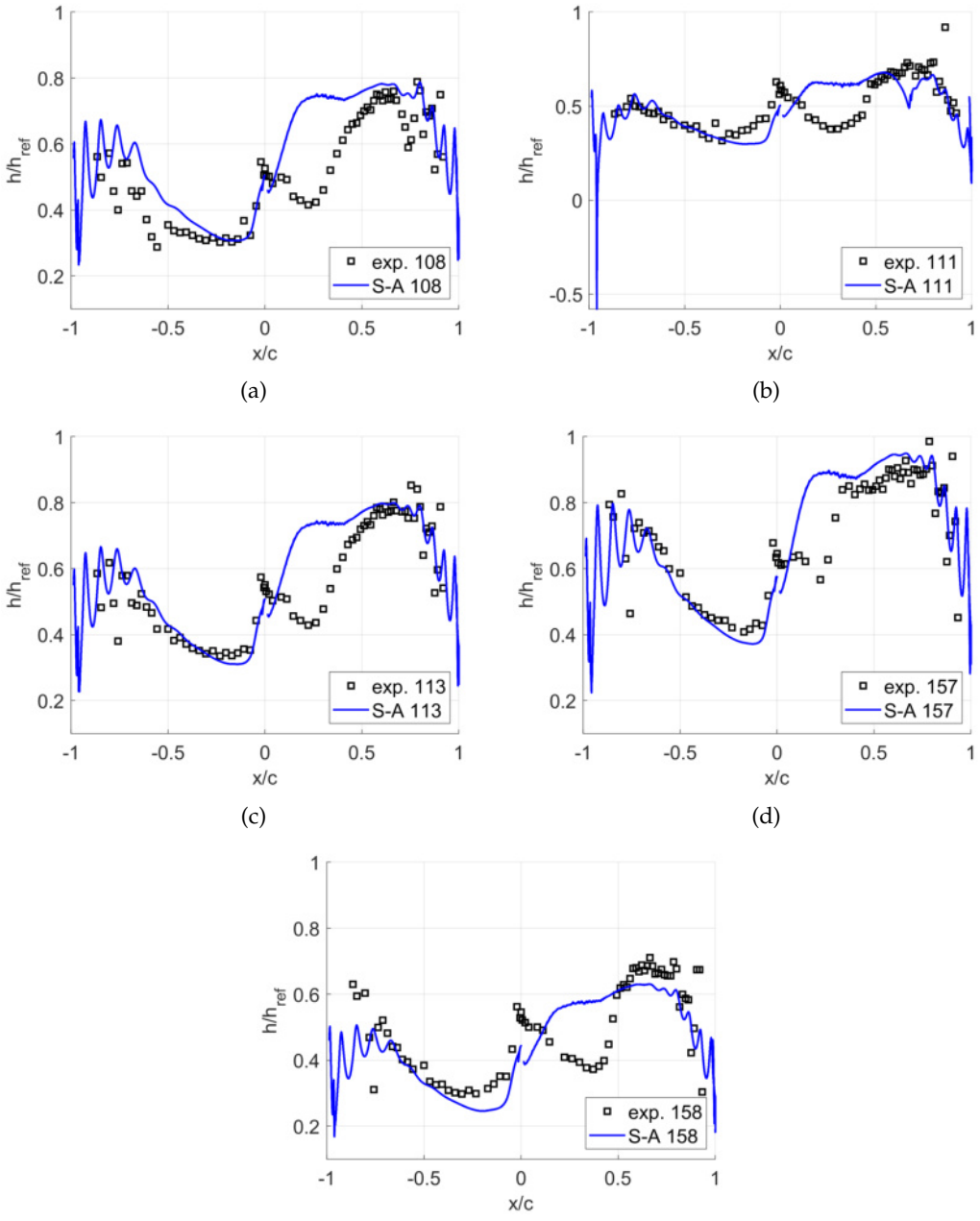

FIGURE 3.4: Comparison of the computed heat transfer coefficient distribution and the experimental data [6], along the blade airfoil contour.

4 Results

In this chapter, the results of the optimization process are presented, aiming at minimum highest blade temperature T^S_{max}, under the conditions of the 5 test-cases, presented in table 3.3. For that to be accomplished, the location of the cooling holes, in the interior of the blade, is to be changed. For the 2-D problem, the displacement of the 10 holes takes place in the axial and pitch-wise directions, while their radii remain fixed. As a result, the design variables consist of the coordinates of the hole centers, increasing the number of them to 20 (i.e. 2 per hole). To avoid any intersection between the holes and the airfoil sides, the appropriate geometric constraints must be defined. It is dictated that the distance between each side and the perimeter of the holes should not exceed 30% of their radius. By maintaining the necessary distance between the holes and the blade sides, high ∇T^S and high thermal stresses can be prevented. Furthermore, upper and lower bounds are imposed on the design variables to prevent overlapping of holes. The use of the aforementioned constraints ensures the creation of realistic geometries and the generation of valid grids in the blade.

Considering that, during the computations, the airfoil contour remains intact, two series of runs were performed. The difference between them lies in the choice of the airfoil shape, used for the optimization. In the first one, the C3X baseline configuration was used, while in the second one, the total pressure losses-optimized configurations, based on the diploma thesis of Panagiotopoulos [13], were used (pr-opt. blades in fig. 4.1) as starting points. Panagiotopoulos has optimized the baseline geometry five times, one for each of the five operating points, aiming to minimize the total pressure losses. It should become clear that the total pressure losses-optimized configurations in [13] have resulted from an optimization procedure with a different objective function and constraints. The optimized versions of the baseline airfoil have different shapes to minimize the total pressure losses, but there is no optimization on the thermal properties. Each of the five optimized airfoils will now be used as starting geometries for thermal optimization, under the same conditions they have been optimized in [13]. In that case, a two-step optimization is practically performed by further thermally optimizing the solutions for each of the 5 test-cases. From this point onward, the two different series of runs will be referred to as TH1 and TH2 optimization, respectively, where **TH** stands for thermal. For instance, using the aforementioned nomenclature, the TH1 optimization's solution, at the conditions of test-case no. 108, will be described as TH1-108 optimized blade. This indicates that the cooling holes of the new blade have been shifted to the new optimized positions. Equivalently, the TH2-158 optimized blade will be the outcome of the two-step optimization under the case-158 conditions, in which both the airfoil shape (step 1, i.e. total pressure losses-optimization) and the holes' location (step 2, i.e. thermal optimization) have been changed.

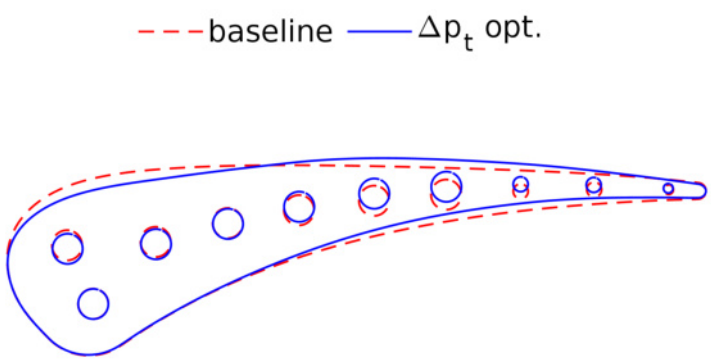

(a) pr-108 opt.

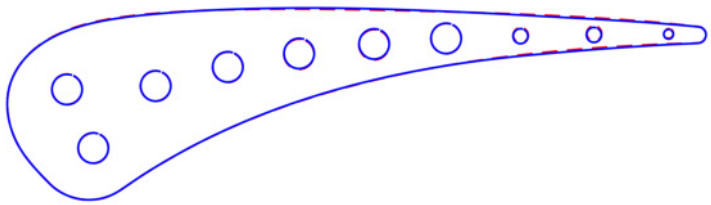

(b) pr-111 opt.

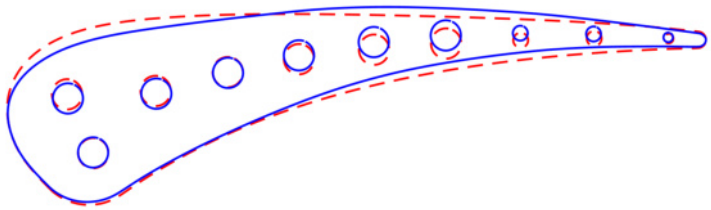

(c) pr-113 opt.

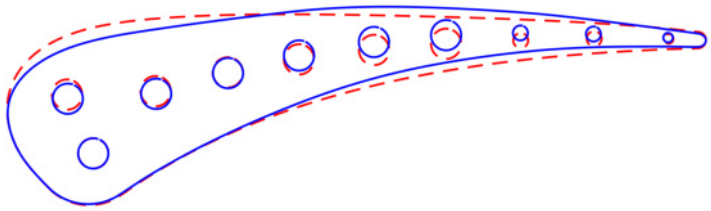

(d) pr-157 opt.

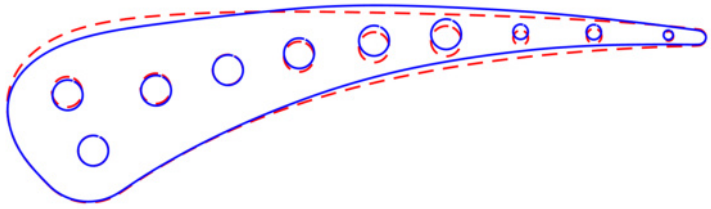

(e) pr-158 opt.

FIGURE 4.1: Comparison of the baseline and total pressure losses-optimized configurations.

4.1 TH1 Optimization

The first part of the optimization runs aims at minimizing the highest blade temperature for the baseline model. During the computations, only the location of the cooling holes can be changed. The optimized hole locations are presented in fig. 4.2. The lower and upper bounds (given in table 3.2), imposed on the design variables, are visualized as rectangular areas. Each center of a hole is allowed to be displaced in its respective area. The effect of the holes' relocation on temperature distribution along the blade is illustrated in fig. 4.3. The length x in the horizontal axis is normalized with the axial chord c. Following optimization, T^S_{max} in the trailing edge, i.e. $x/c = \pm 1$, has been reduced. The holes in the front half of the blade have been displaced toward the suction side ($x/c > 0$), cooling the local area and increasing T^S along the pressure side ($x/c > 0$). It is clear that the cooling holes have been displaced toward the regions of high temperature, as shown in figs. 4.6a, 4.7a, 4.8a, 4.9a and 4.10a. Specifically, the 2 front holes have been re-positioned near the leading edge, while the rest are closer to the trailing edge. The fields of temperature gradient magnitude, for each case, are illustrated in figs. 4.6b, 4.7b, 4.8b, 4.9b and 4.10b. The highest gradient is measured in the perimeter of the cooling hole no.8. The convergence history of the highest solid temperature is plotted in fig. 4.4. It can be concluded that the percentage change of T^S_{max} converges to $\sim$ - 4 % for the subsonic and $\sim$ - 1.5 % for the transonic cases. Furthermore, the figures contain information on the distance of the 10^{th} hole's center from the pressure and suction sides, normalized with its radius, fig. 4.5. For all test-cases, the distance of the 10^{th} hole's center from the suction and pressure side converges to $\sim$ 1.9 and $\sim$ 2 radii, respectively.

It can be deducted that the value of the highest blade temperature is sensitive to the location of the 10^{th} cooling hole, as this hole is the nearest to the trailing edge, where T^S_{max} is attained. For instance, when contrasting figs. 4.4a and 4.5a for the TH1-108 optimized blade, it can be seen that the sharpest changes in temperature are related to the hole's distance from the suction side. As the distance increases, the hole moves toward the center of the blade, hence away from the trailing edge. This could result in less local cooling, leading to a local temperature rise. The above is confirmed by examining the sensitive derivatives diagram in fig. 4.11, computed with the adjoint method. The design variable no. 19, i.e. the x-coordinate of the 10^{th} hole's center has the greatest impact on the objective function T^S_{max}.

To further support the previous hypothesis, the candidate solutions of 9^{th}, 14^{th}, 24^{th}, and 32^{th} optimization cycles for the test-case 108 will be presented. Figures 4.12 and 4.13 show that by moving the 10^{th} hole away from hole no.9 (9^{th}, 24^{th} opt. cycle), the region between the 2 holes is exposed to high T^S_{max}. In contrast, positioning the hole away from the trailing edge (14^{th} opt. cycle), increases T^S_{max} in that area, as is already known. Consequently, to lower T^S_{max} across the entire region between hole no. 9 and the trailing edge, the optimization algorithm carefully adjusts the position of hole no. 10.

Following the algorithm's convergence, each of the 5 optimized solutions, was re-evaluated at the conditions of the 4 other cases. The temperature drop is given in table 4.1 and equals $\sim$ 27.5 K for the subsonic cases, and $\sim$ 10.5 K for the transonic one (case 111) from their baseline values. The best solution for each case is highlighted in cyan, although the differences between them are not greater than $\sim$ 1 K. This can be considered to be well within the CFD code inaccuracies. Regarding the total pressure losses, as can be seen in table 4.2, the difference between the values is barely noticeable, given that the airfoil shape is the baseline one. In addition, by calculating the mean displacement of each hole for the 5 test-cases, as seen

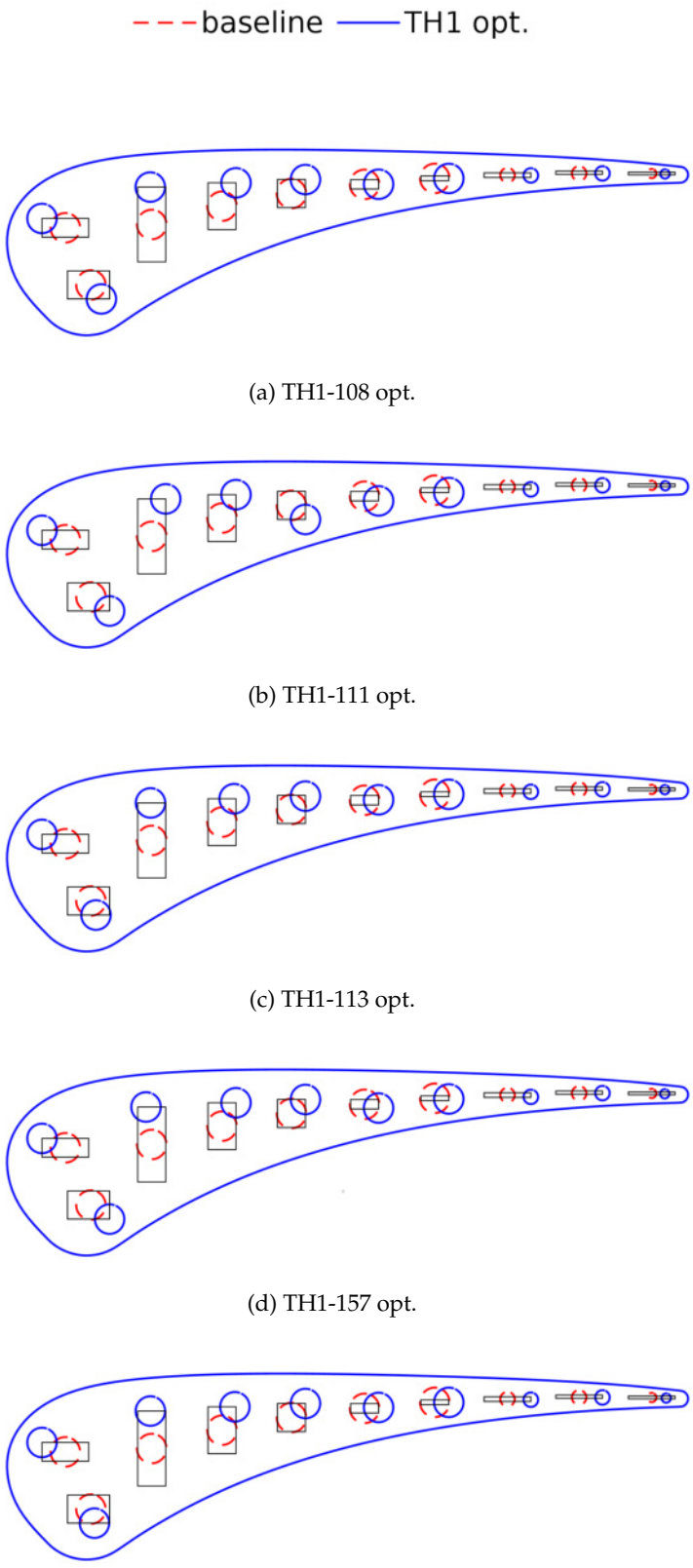

(a) TH1-108 opt.

(b) TH1-111 opt.

(c) TH1-113 opt.

(d) TH1-157 opt.

(e) TH1-158 opt.

FIGURE 4.2: Comparison of the baseline and TH1 optimized configurations.

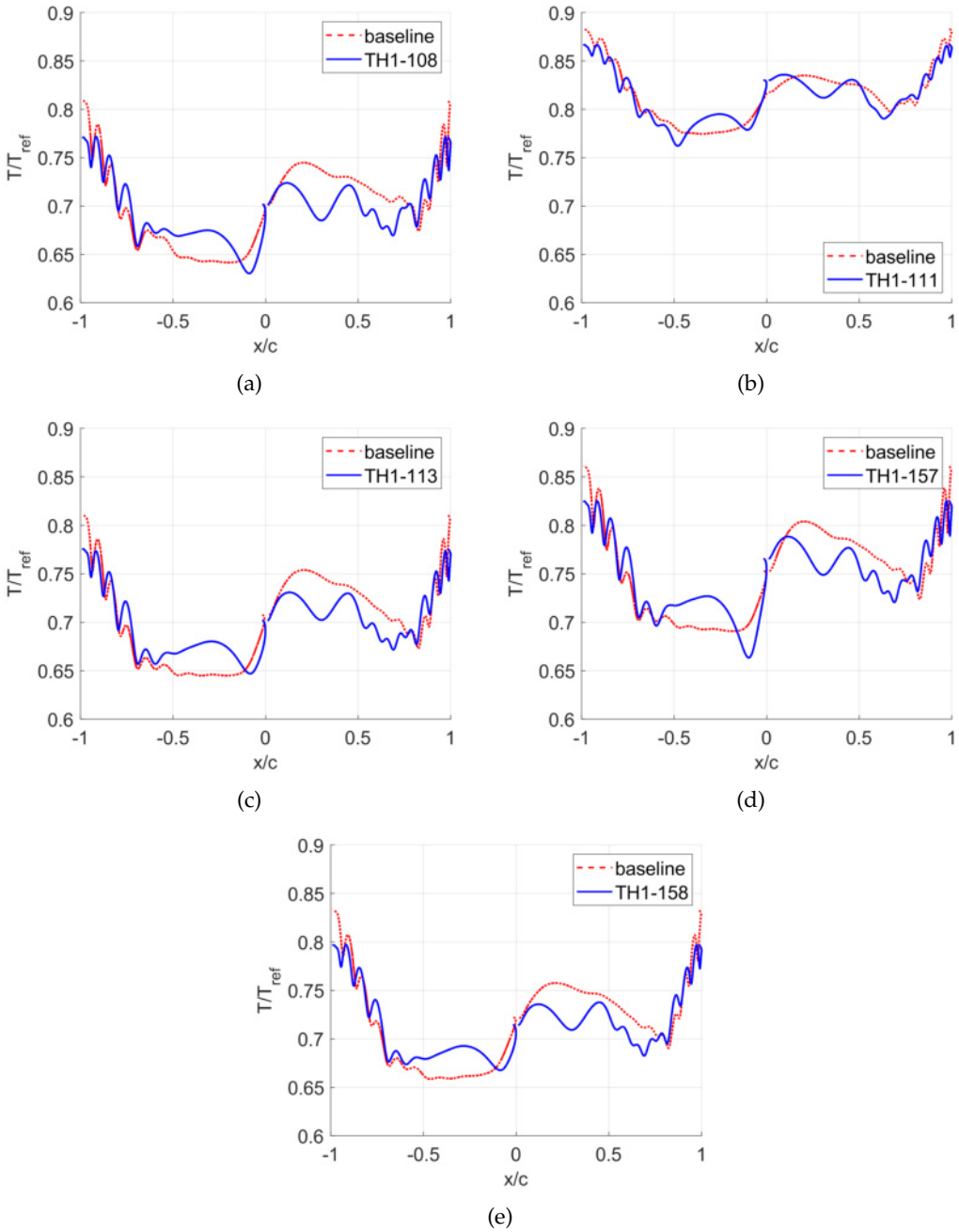

FIGURE 4.3: Comparison of the baseline and TH1 optimized temperature distribution along the blade airfoil contour.

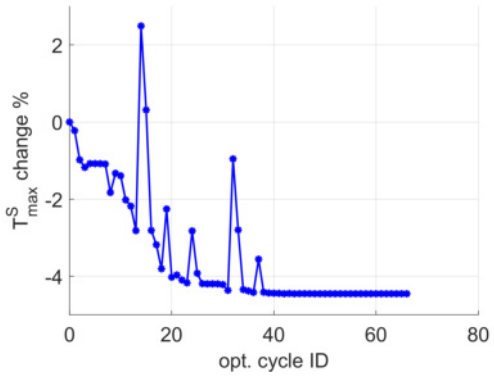

(a) TH1-108 opt.

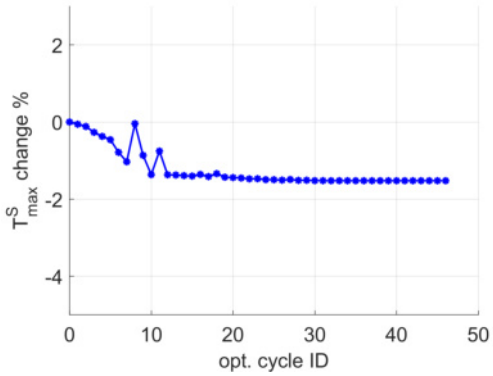

(b) TH1-111 opt.

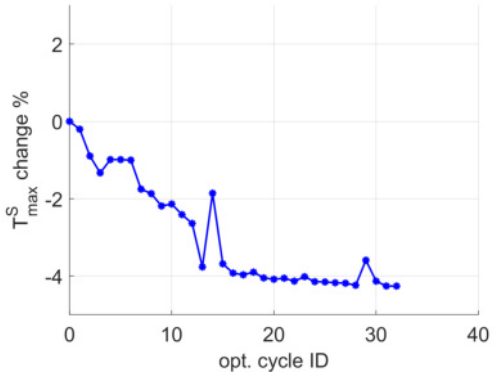

(c) TH1-113 opt.

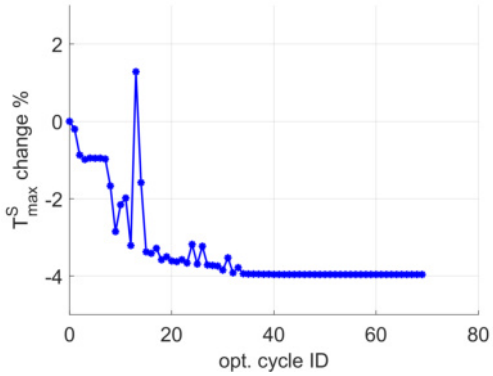

(d) TH1-157 opt.

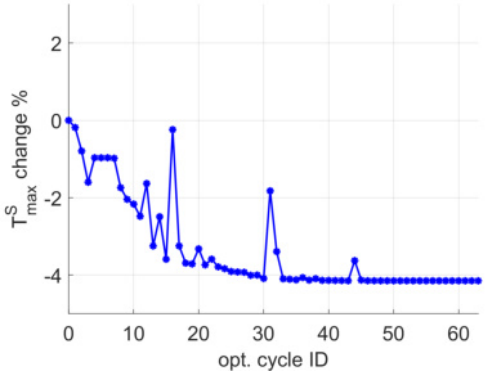

(e) TH1-158 opt.

FIGURE 4.4: Convergence history of highest solid temperature for the TH1 optimization.

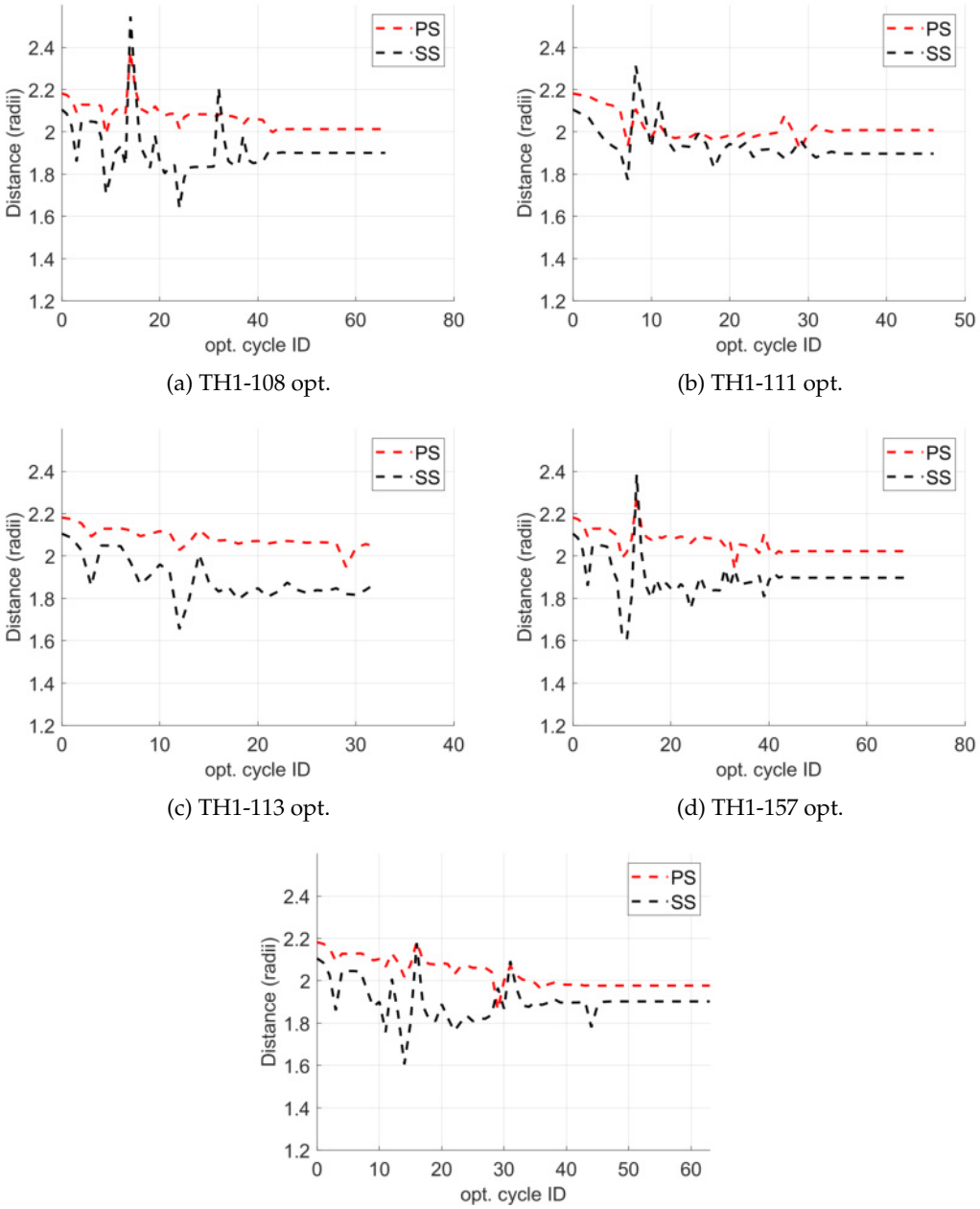

(a) TH1-108 opt.

(b) TH1-111 opt.

(c) TH1-113 opt.

(d) TH1-157 opt.

(e) TH1-158 opt.

FIGURE 4.5: Convergence history of 10th hole's center distance from blade sides for the TH1 optimization.

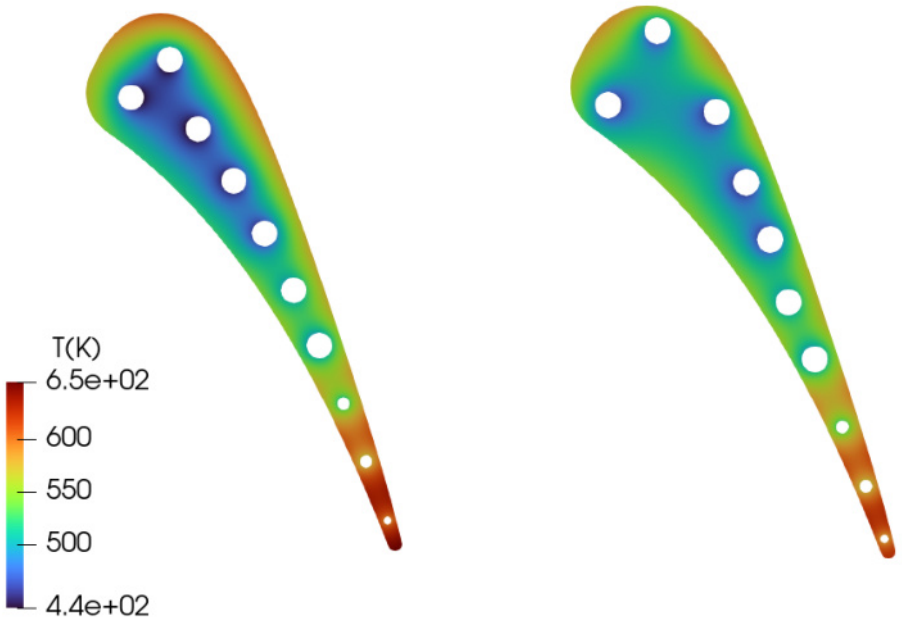

(a) temperature

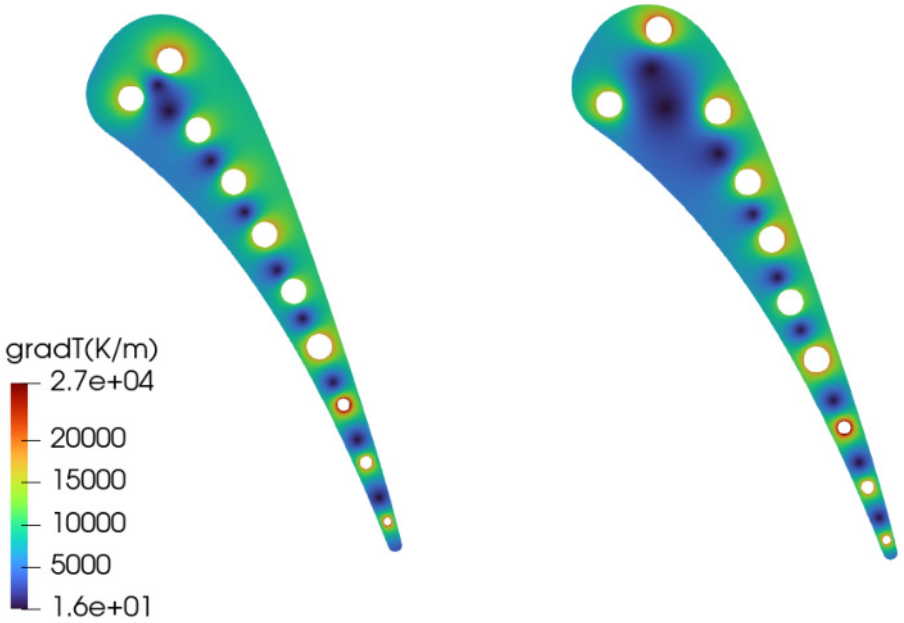

(b) temperature gradient

FIGURE 4.6: Temperature and temperature gradient magnitude distributions of the baseline (**left**) and TH1-108 optimized (**right**) blade.

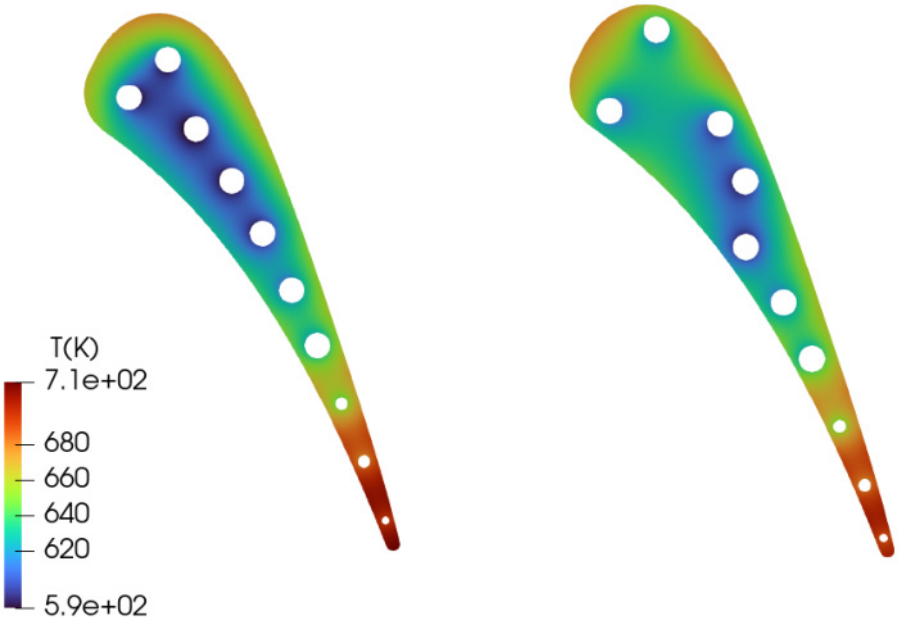

(a) temperature

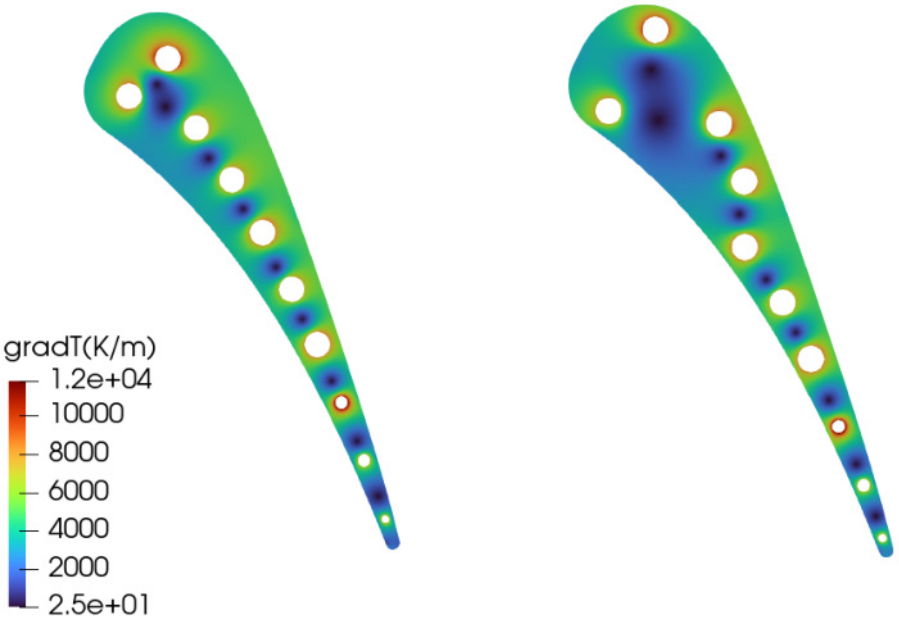

(b) temperature gradient

FIGURE 4.7: Temperature and temperature gradient magnitude distributions of the baseline (**left**) and TH1-111 optimized (**right**) blade.

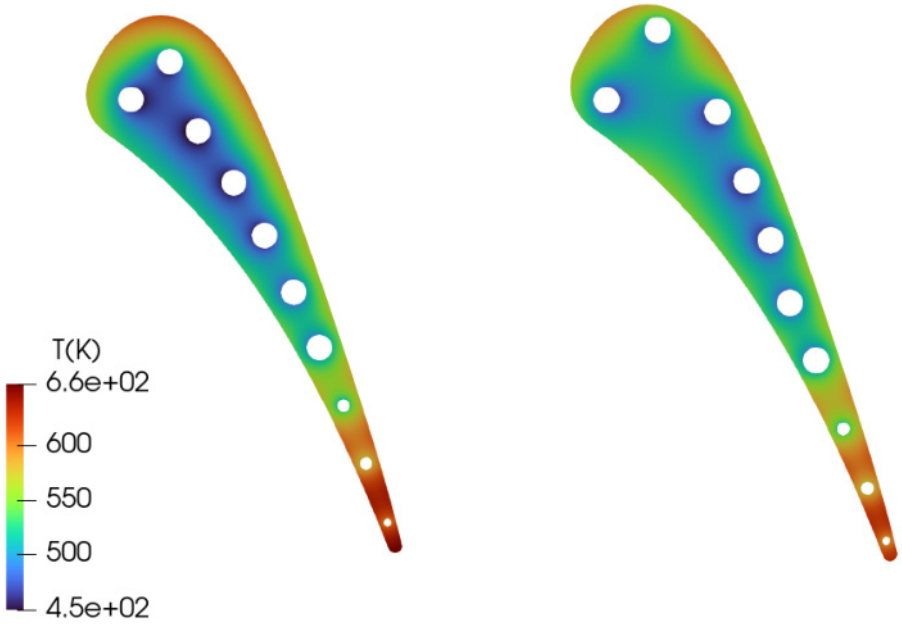

(a) temperature

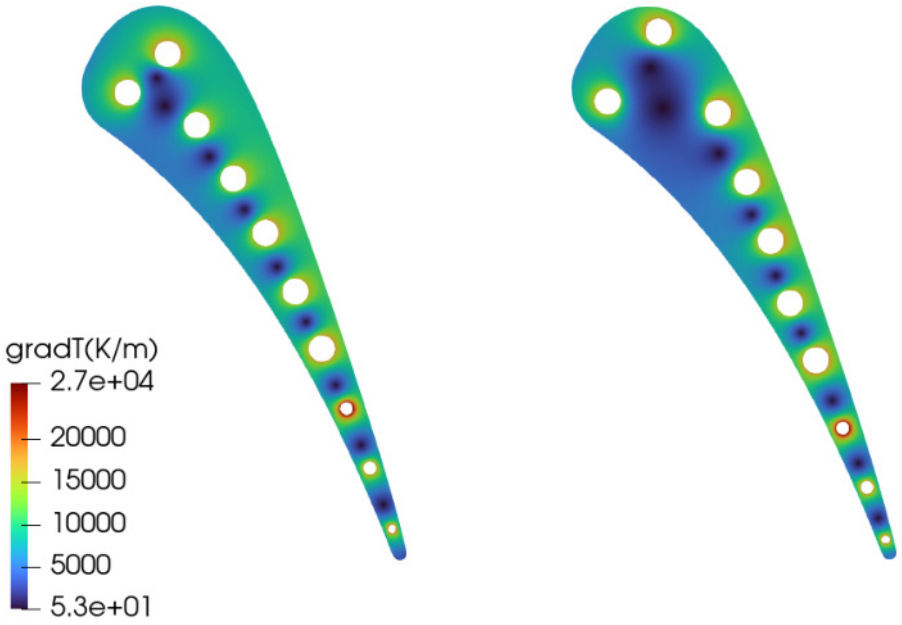

(b) temperature gradient

FIGURE 4.8: Temperature and temperature gradient magnitude distributions of the baseline (**left**) and TH1-113 optimized (**right**) blade.

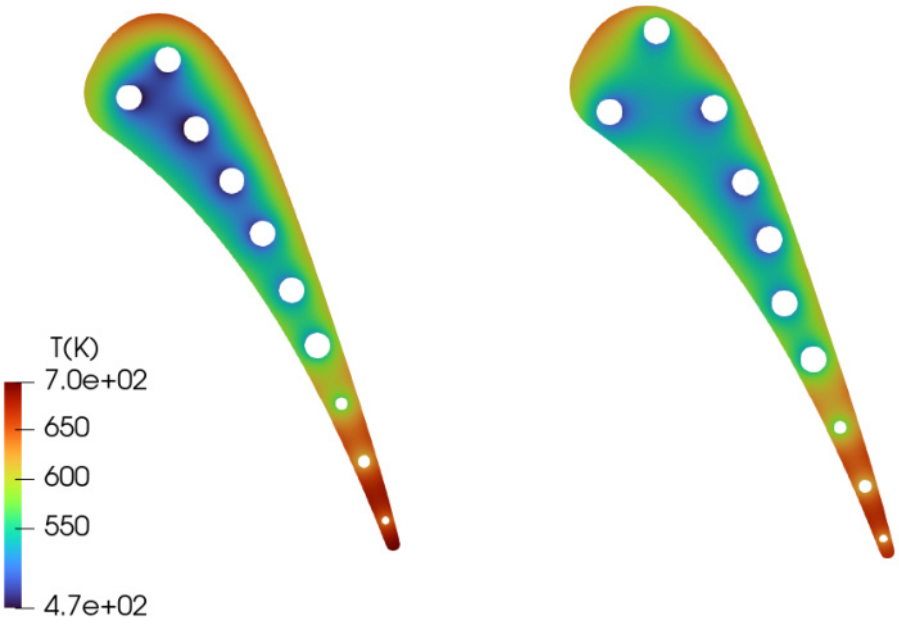

(a) temperature

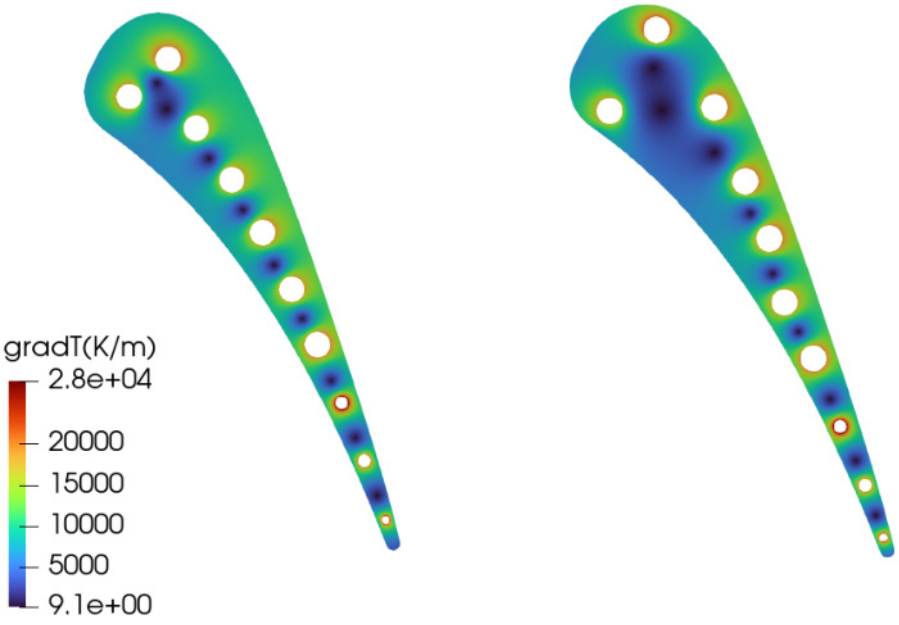

(b) temperature gradient

FIGURE 4.9: Temperature and temperature gradient magnitude distributions of the baseline (**left**) and TH1-157 optimized (**right**) blade.

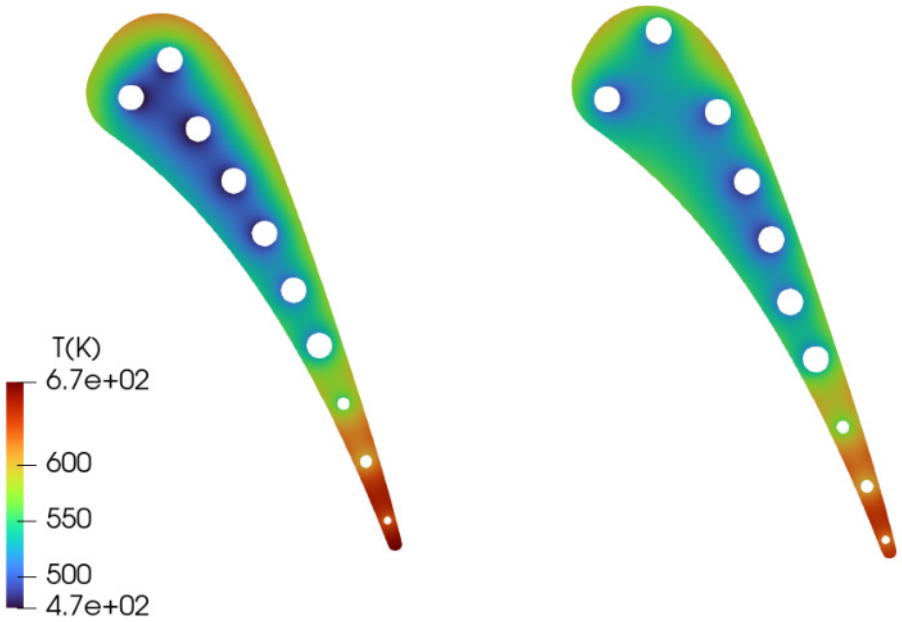

(a) temperature

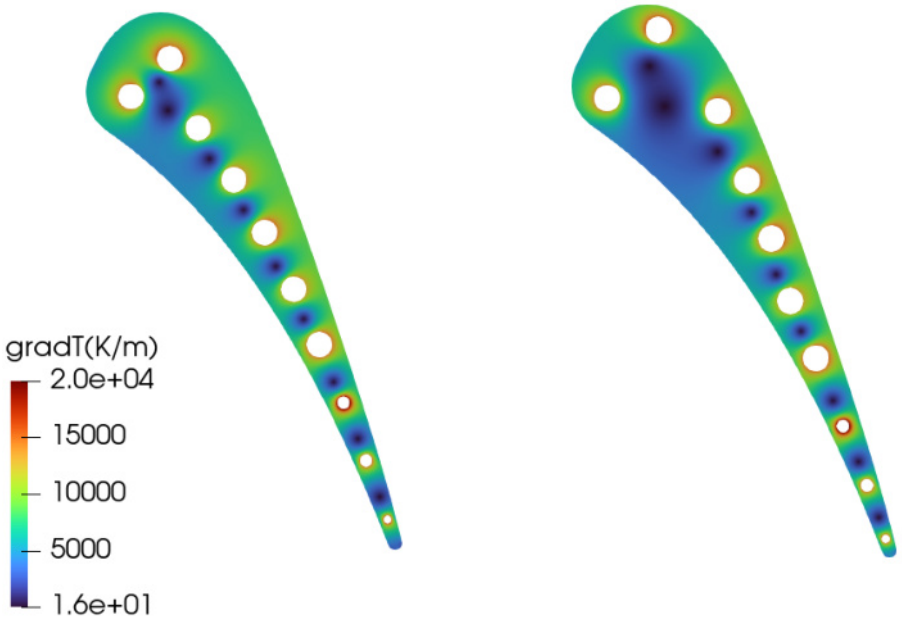

(b) temperature gradient

FIGURE 4.10: Temperature and temperature gradient magnitude distributions of the baseline (**left**) and TH1-158 optimized (**right**) blade.

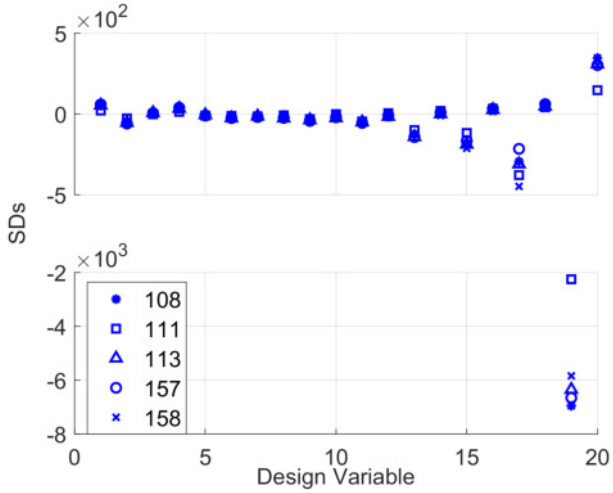

FIGURE 4.11: Sensitivity derivatives computed for the starting geometry with the adjoint method.

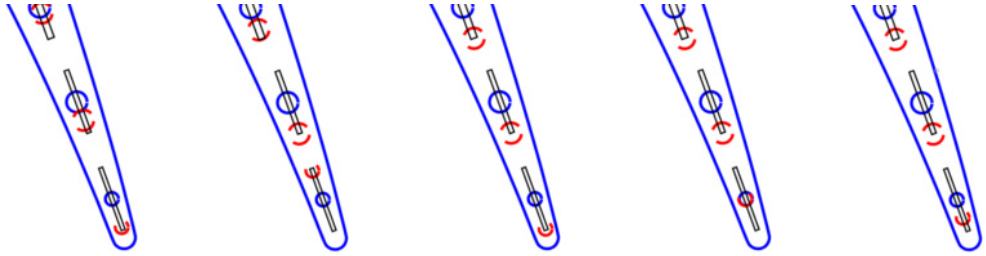

(a) 9th (b) 14th (c) 24th (d) 32th (e) TH1-108 opt.

FIGURE 4.12: The holes' location for a number of candidate solutions of the TH1-108 optimization.

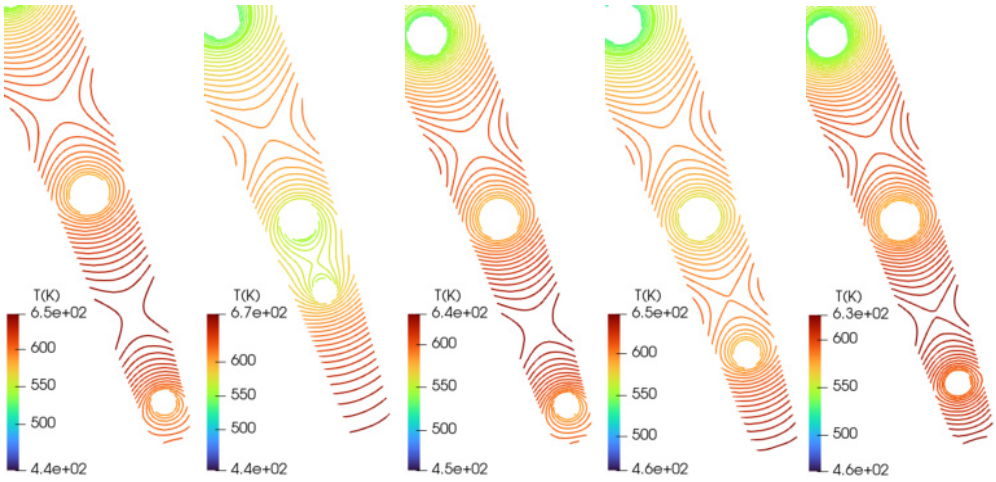

(a) 9th (b) 14th (c) 24th (d) 32th (e) TH1-108 opt.

FIGURE 4.13: The temperature field for a number of candidate solutions of the TH1-108 optimization.

TABLE 4.1: Highest solid temperature T^S_{max} (K) of the baseline optimized blades.

flow conditions	baseline	optimized blade					
		108	**111**	**113**	**157**	**158**	**multi**
108	649.6	620.7	620.7	620.7	620.6	621.4	620.7
111	709.2	698.6	698.4	698.6	698.6	698.7	698.6
113	651.1	623.2	623.1	623.3	623.3	623.3	623.2
157	691.4	664.1	664.2	664.1	664.0	665.0	664.2
158	669.6	642.4	642.2	642.6	642.6	641.8	642.2

TABLE 4.2: Total pressure losses Δp_t (Pa) of the TH1 optimized blades.

flow conditions	baseline	optimized blade					
		108	**111**	**113**	**157**	**158**	**multi**
108	5540.5	5510.9	5515.9	5511.7	5511.2	5510.3	5512.1
111	12384.9	12388.1	12390.4	12388.4	12388.2	12388.5	12388.6
113	5490.2	5460.0	5465.5	5460.8	5460.5	5459.6	5461.4
157	6856.9	6821.4	6827.7	6822.3	6821.9	6820.7	6822.9
158	4490.3	4469.6	4473.2	4470.2	4469.8	4469.4	4470.5

in fig. 4.14, a pseudo-multipoint optimization can be accomplished. All holes, with the exception of no. 10, have been placed on the allowed boundaries, denoted by black lines. The performance of the new configuration (indicated as *multi* blade in the aforementioned tables) is identical to that of the optimized ones.

4.2 TH2 Optimization

The outcomes of the TH2 optimization will be presented in this section. In the previous section, the geometry optimized under the five different flow conditions was the baseline one, based on [6]. In this section, there are five different geometries, obtained from [13]. Each of them is the new version of the baseline geometry, optimized in terms of total pressure losses, under each of the five different operating points. For instance, pr-108 airfoil is the optimized version of the baseline one in terms of total pressure losses, under the test-case 108 conditions. As a result, the new airfoil has a different airfoil shape from the baseline one, and slightly displaced holes (to match the airfoil shape). Each of the airfoils will be thermally optimized under the conditions they already have been optimized, in terms of total pressure losses. In the above example, the pr-108 airfoil will now be thermally optimized only under the same conditions, i.e. the 108 operating point. As a result, the TH2-108 optimized configuration will now be optimized both in terms of total pressure losses (optimization in [13]) and in terms of the highest solid temperature (achieved in the present thesis).

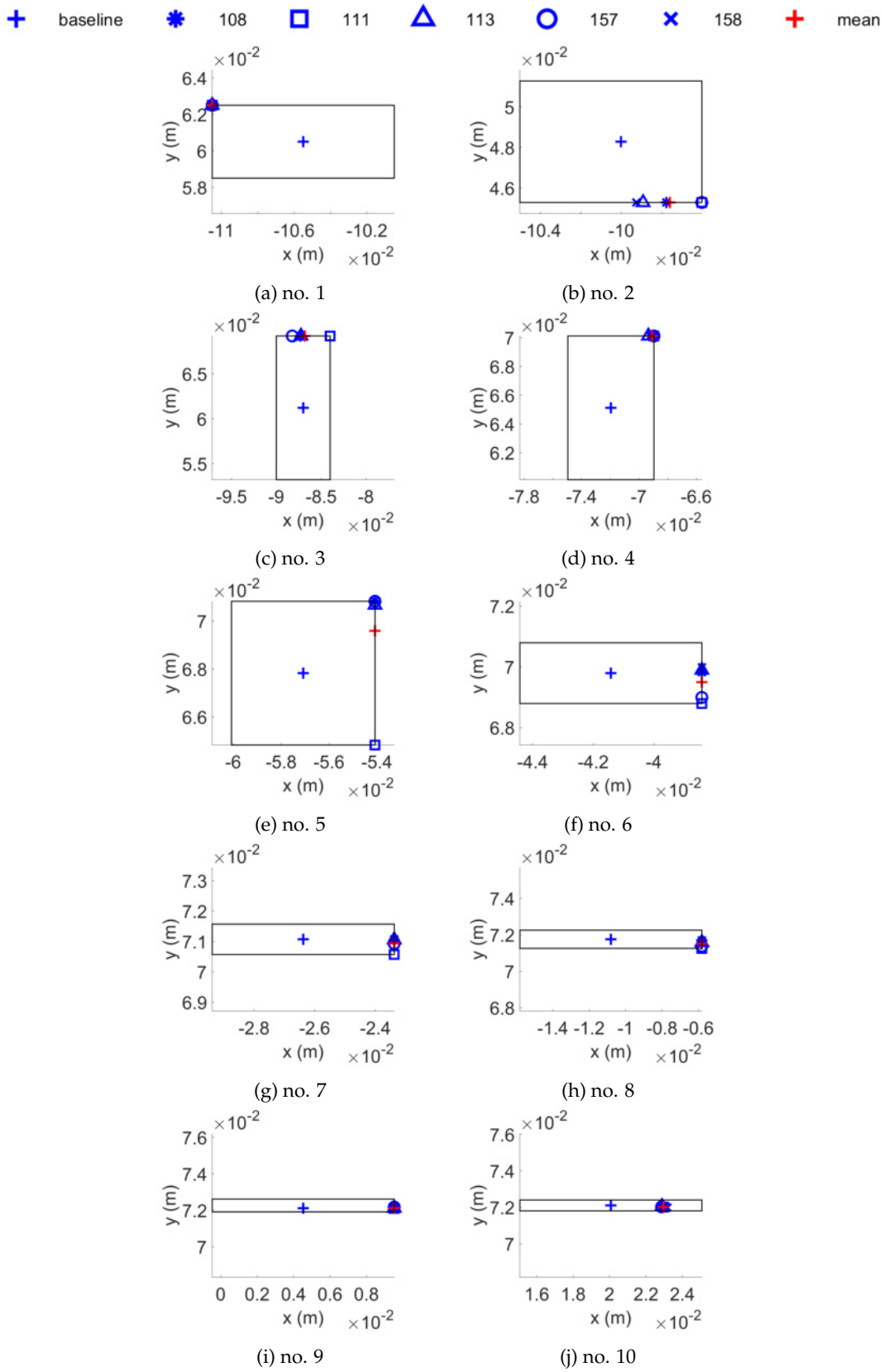

(a) no. 1 (b) no. 2

(c) no. 3 (d) no. 4

(e) no. 5 (f) no. 6

(g) no. 7 (h) no. 8

(i) no. 9 (j) no. 10

FIGURE 4.14: Baseline and optimized locations of the cooling holes' centers for TH1 optimization.

TABLE 4.3: Total pressure losses and highest solid temperature of the TH2 optimized configurations at each optimization step.

flow conditions	Δp_t (Pa)			$T_{\max}$ (K)		
	baseline	**step 1**	**step 2**	**baseline**	**step 1**	**step 2**
108	5540.5	4296.8	4281.2	649.6	651.4	622.3
111	12384.9	10699.9	10704.3	709.2	710.3	699.2
113	5490.2	4236.2	4216.3	651.1	652.9	624.1
157	6856.9	5216.6	5193.5	691.4	693.7	665.4
158	4490.3	3562.3	3547.5	669.6	670.9	642.2

TABLE 4.4: Highest solid temperature T^S_{max} (K) of the TH2 optimized blades.

flow conditions	baseline	optimized blade				
		108	**111**	**113**	**157**	**158**
108	649.6	622.3	621.3	621.8	621.5	622.1
111	709.2	700.1	699.2	699.5	700.1	699.1
113	651.1	624.7	623.5	624.1	624.2	624.0
157	691.4	666.1	664.8	665.8	665.4	666.0
158	669.6	643.4	642.3	642.4	642.8	642.2

Figure 4.15 demonstrates that the holes have, as anticipated, been shifted toward the high-temperature regions. The baseline and optimized airfoil shapes are different. As presented in the convergence history diagrams (figs. 4.17 and 4.18) and the T^S, ∇T^S fields (figs. 4.19 to 4.23), the results are in good agreement with those of the previous section since the percentage change of T^S_{max} equals $\sim$ - 4 % for the subsonic test-cases and $\sim$ - 1.5 % for the transonic one. With the exception of the transonic case, there is a slight reduction in the 10^{th} hole center distance from the blade sides, compared to the TH1 optimization. The aforementioned are fully justified, as the trailing edge thickness has been reduced after the pressure losses optimization in all cases, except for case 111, where there have been minimal geometry changes. Additionally, as shown in figs. 4.24 to 4.28, the flow velocity in the passage throat region has been reduced, decreasing the total pressure losses. For subsonic cases, a weak shock wave occurs at $x/c \simeq 0.6$ of the suction side.

The values of the total pressure drop and highest temperature are given in table 4.3, for each step of the optimization process. At the end of the computations, the highest temperature drop is $\sim$ 27 K for the subsonic cases and $\sim$ 10 K for the transonic one. The total pressure percentage drop ranges from $\sim$ 21% to $\sim$ 24% for the subsonic cases and is equal to $\sim$ 13.5% for the test-case 111. As shown in tables 4.4 and 4.5, when tested under various conditions, each optimized configuration yields a comparable T^S_{max}.

The first optimization [13] was carried out, with changes in the inlet flow capacity and flow exit angle constrained to 0.1% from their baseline values in table 4.6. The inlet capacity is slightly higher after step 2 (table 4.7), while for the majority of re-evaluations, the exit angle condition is met (table 4.8). The violations mainly relate

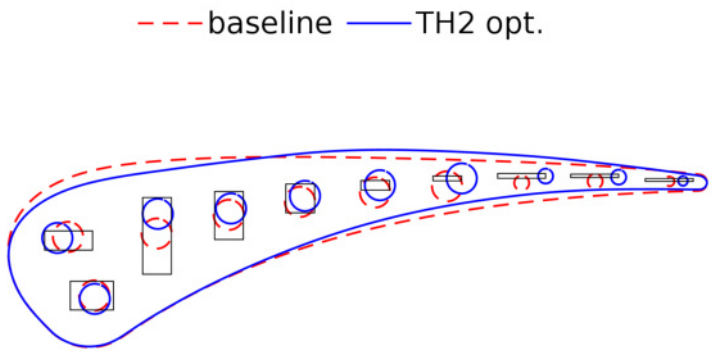

(a) TH2-108 opt.

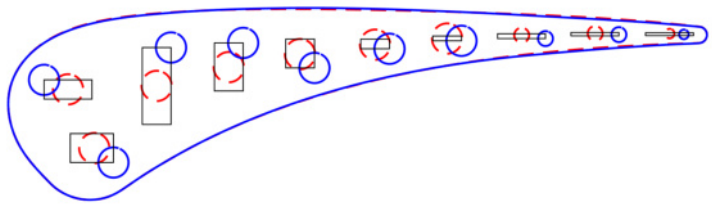

(b) TH2-111 opt.

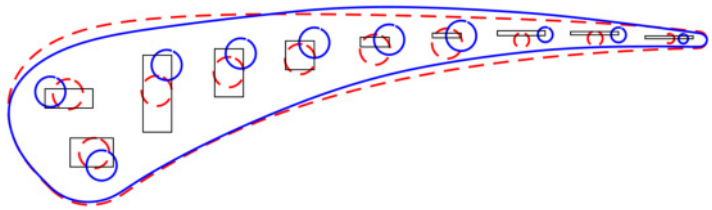

(c) TH2-113 opt.

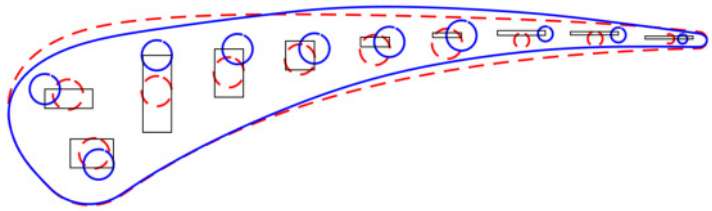

(d) TH2-157 opt.

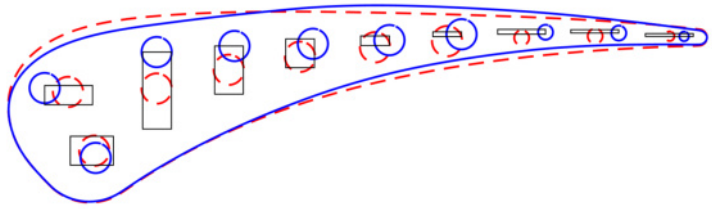

(e) TH2-158 opt.

FIGURE 4.15: Comparison of the baseline and opt-TH2 configurations.

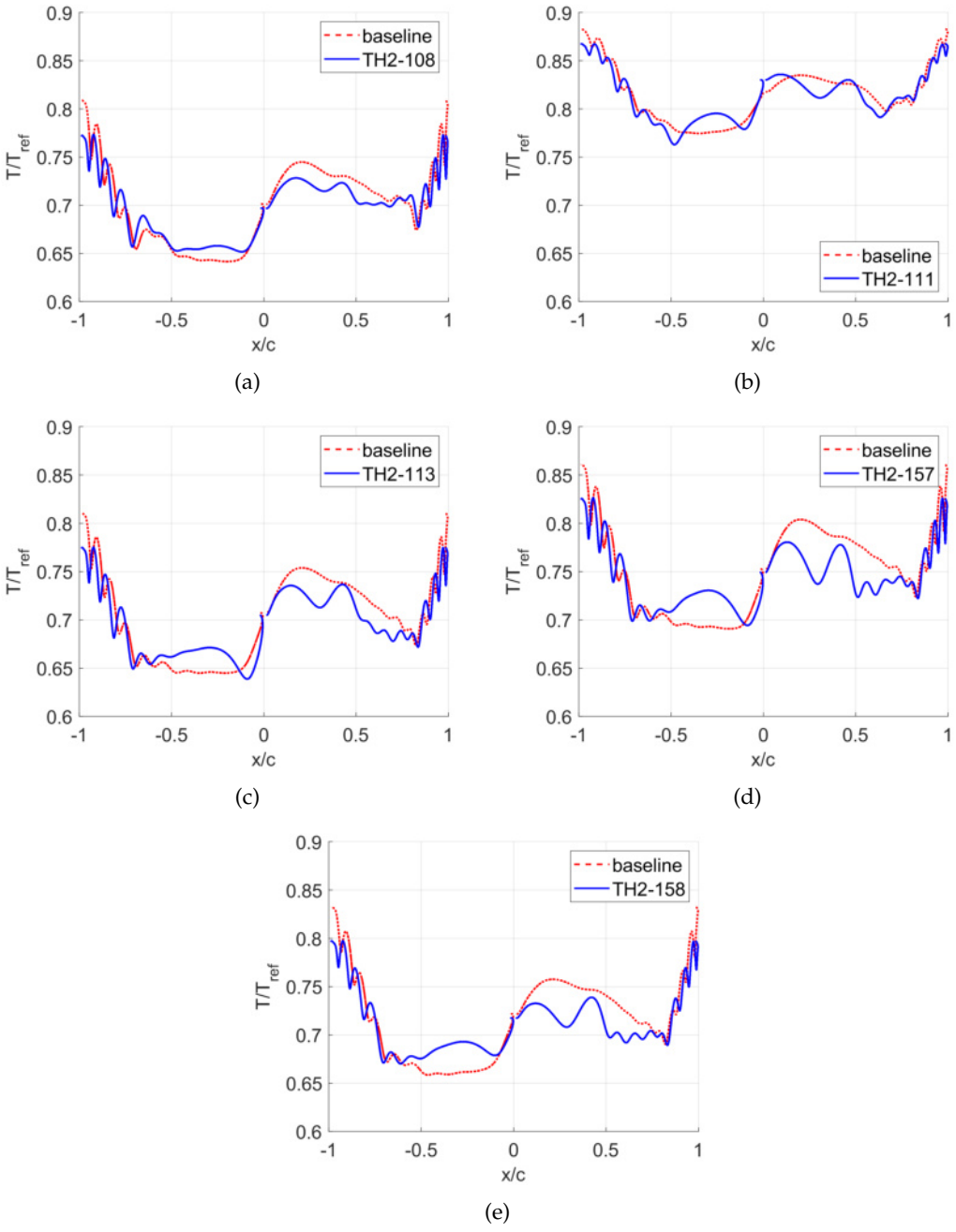

FIGURE 4.16: Comparison of the baseline and TH2 optimized temperature distribution along the blade airfoil contour.

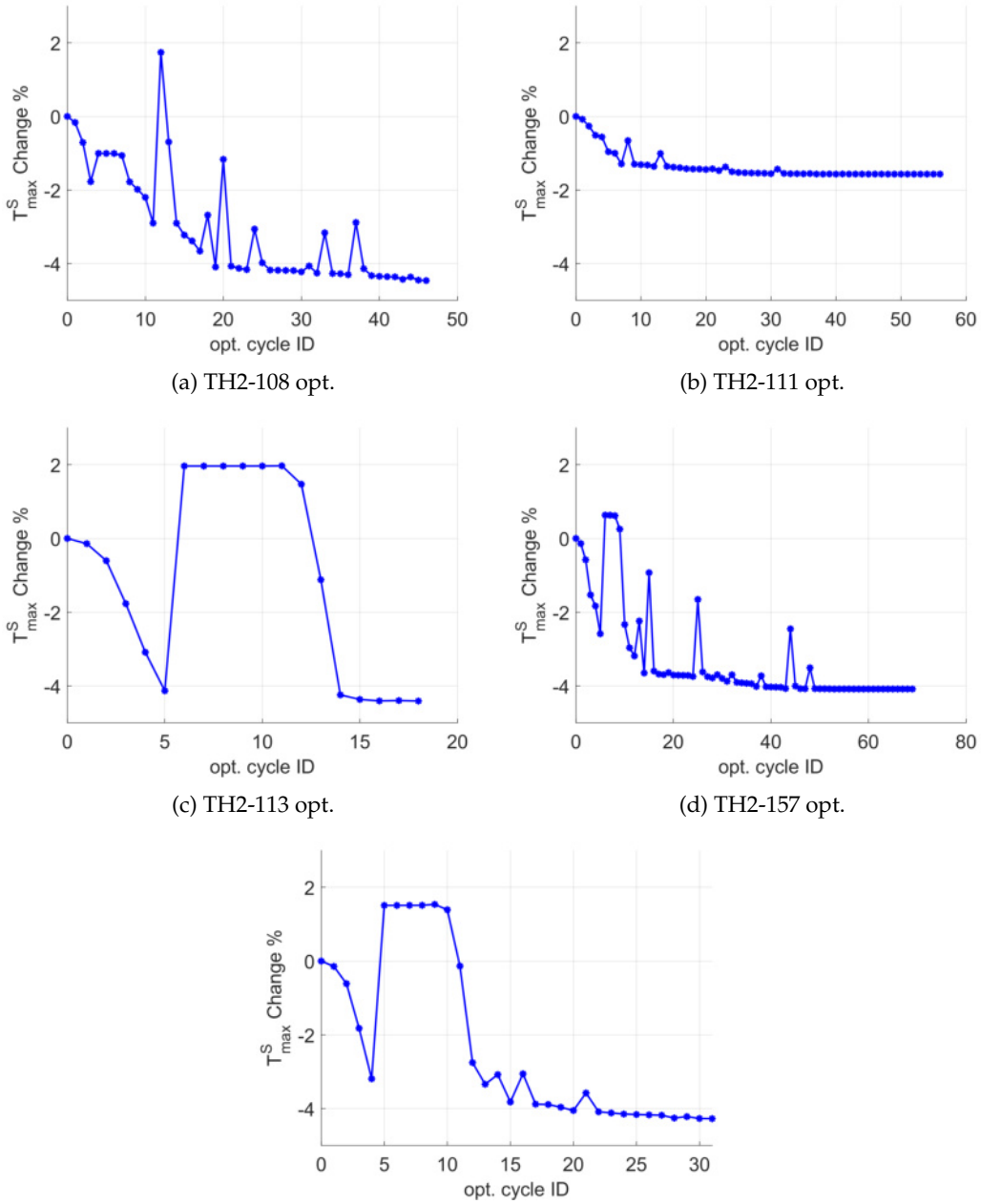

(a) TH2-108 opt.

(b) TH2-111 opt.

(c) TH2-113 opt.

(d) TH2-157 opt.

(e) TH2-158 opt.

FIGURE 4.17: Convergence history of highest solid temperature for the TH2 optimization.

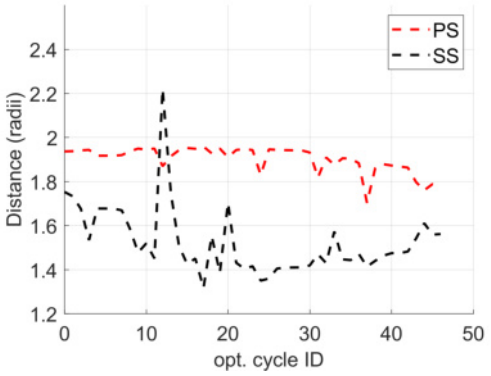

(a) TH2-108 opt.

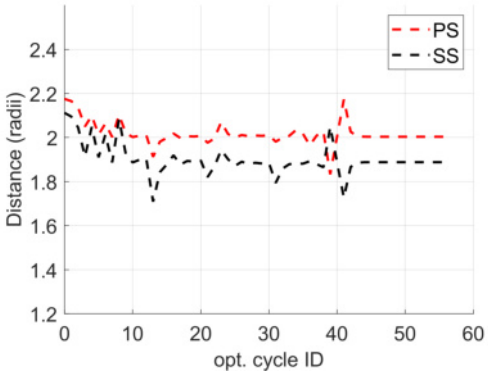

(b) TH2-111 opt.

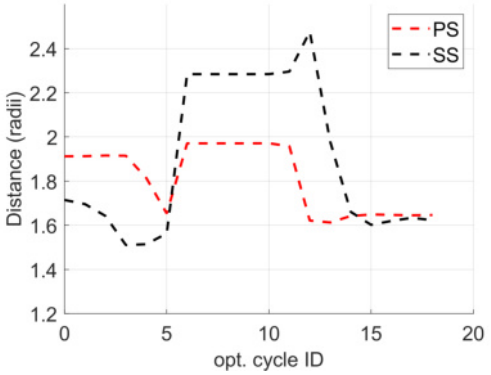

(c) TH2-113 opt.

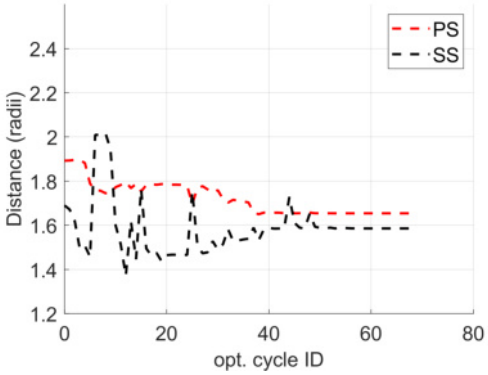

(d) TH2-157 opt.

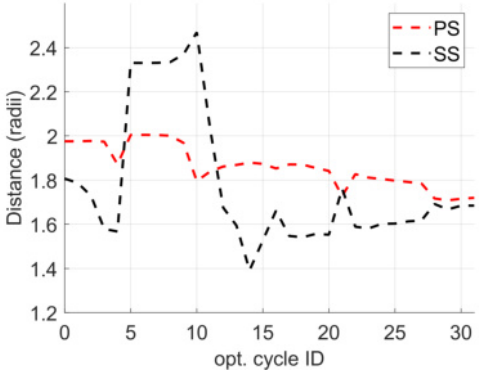

(e) TH2-158 opt.

FIGURE 4.18: Convergence history of 10^{th} hole's center distance from blade sides for the TH2 optimization.

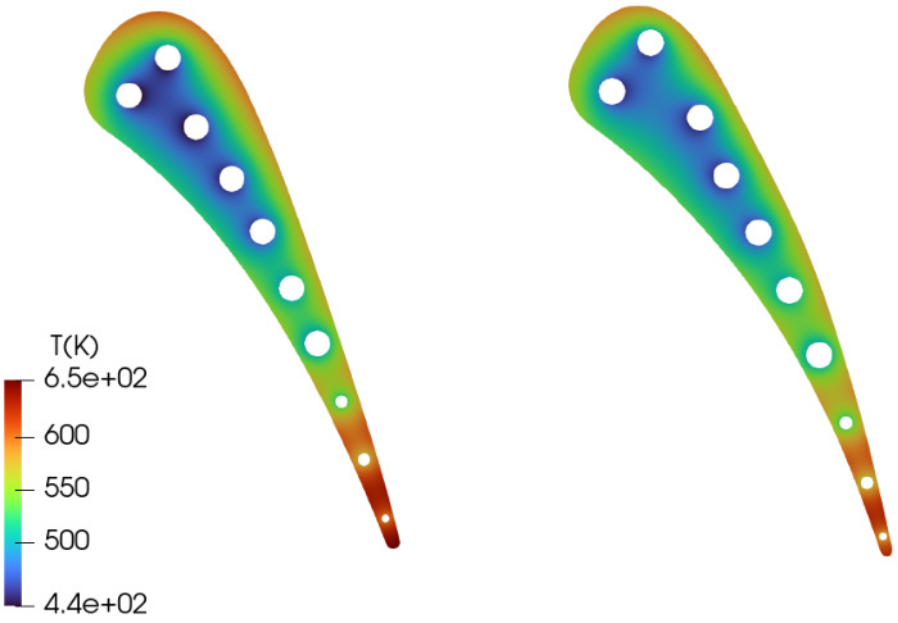

(a) temperature

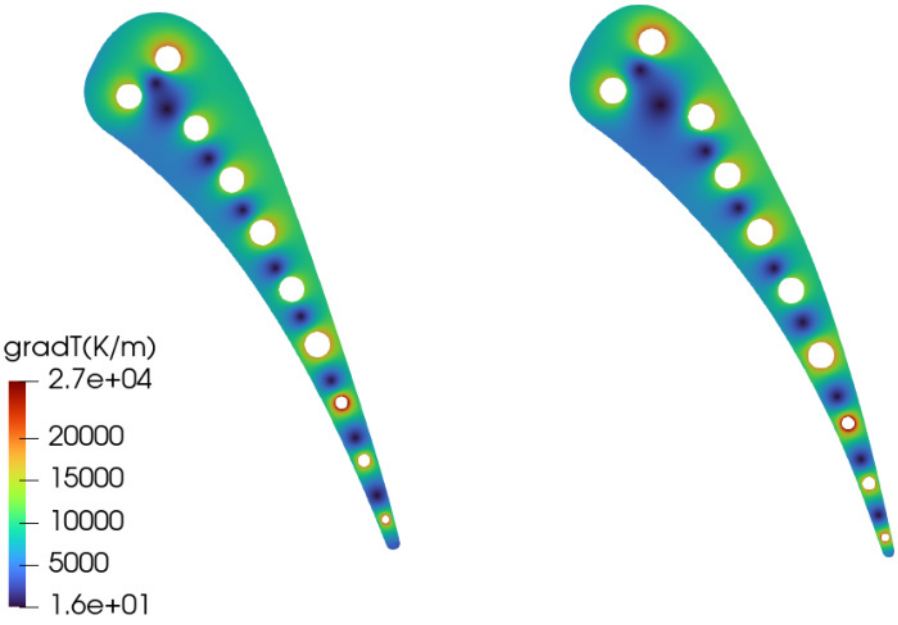

(b) temperature gradient

FIGURE 4.19: Temperature and temperature gradient magnitude distributions of the baseline (**left**) and TH2-108 optimized (**right**) blade.

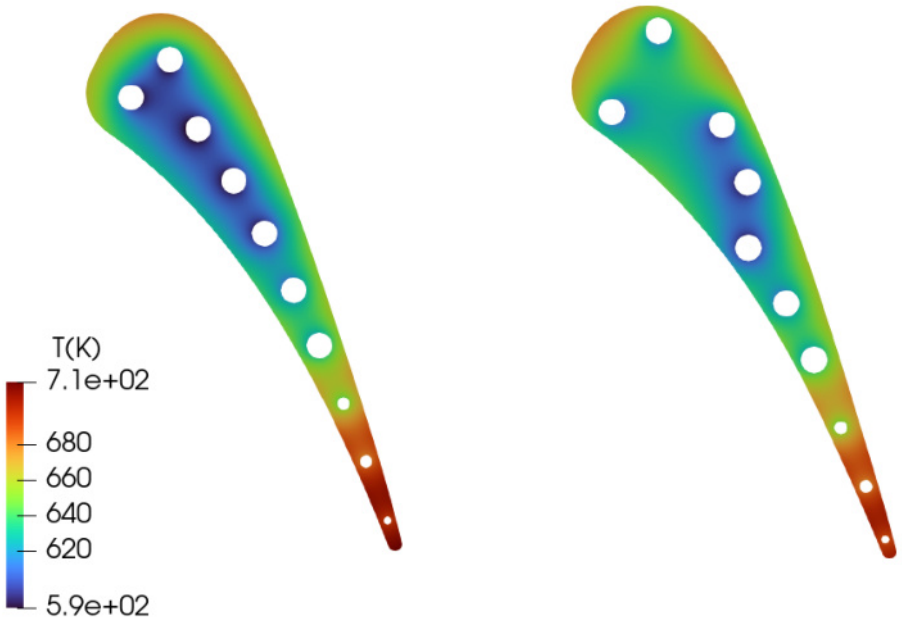

(a) temperature

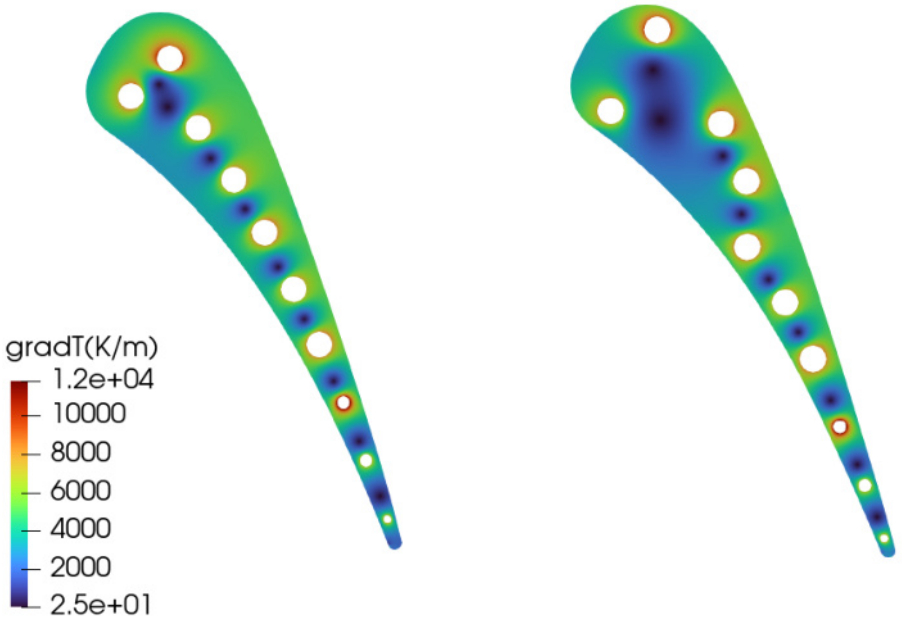

(b) temperature gradient

FIGURE 4.20: Temperature and temperature gradient magnitude distributions of the baseline (**left**) and TH2-111 optimized (**right**) blade.

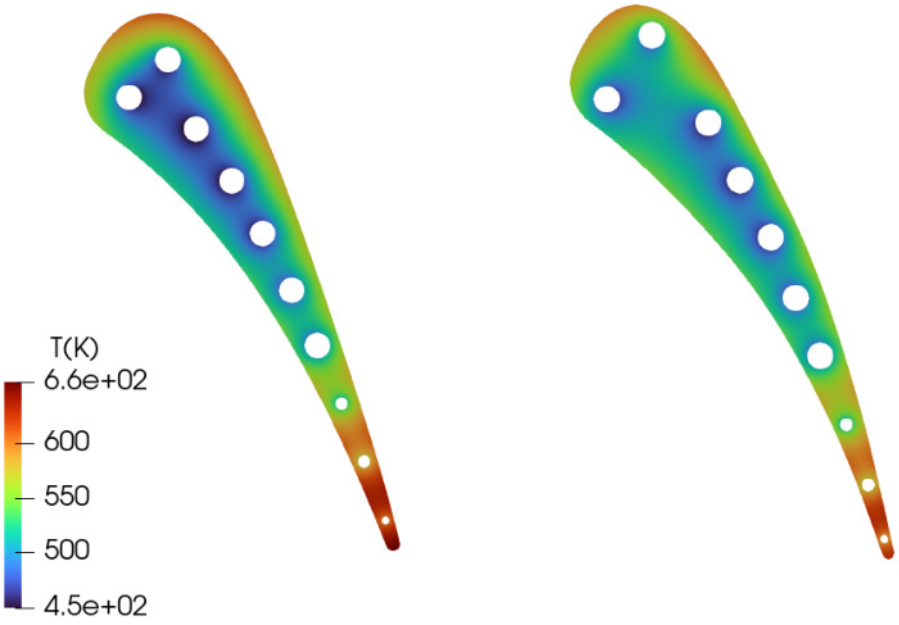

(a) temperature

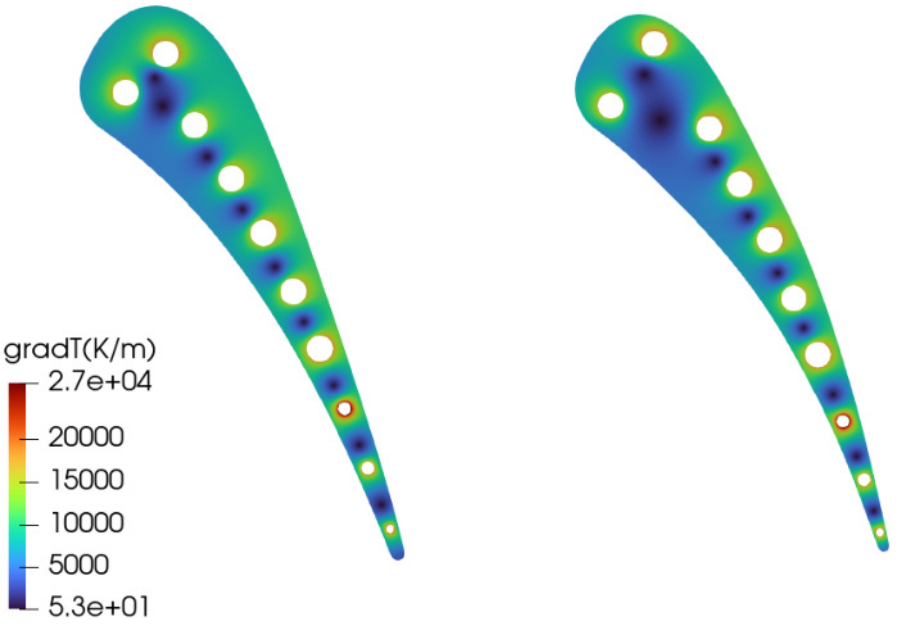

(b) temperature gradient

FIGURE 4.21: Temperature and temperature gradient magnitude distributions of the baseline (**left**) and TH2-113 optimized (**right**) blade.

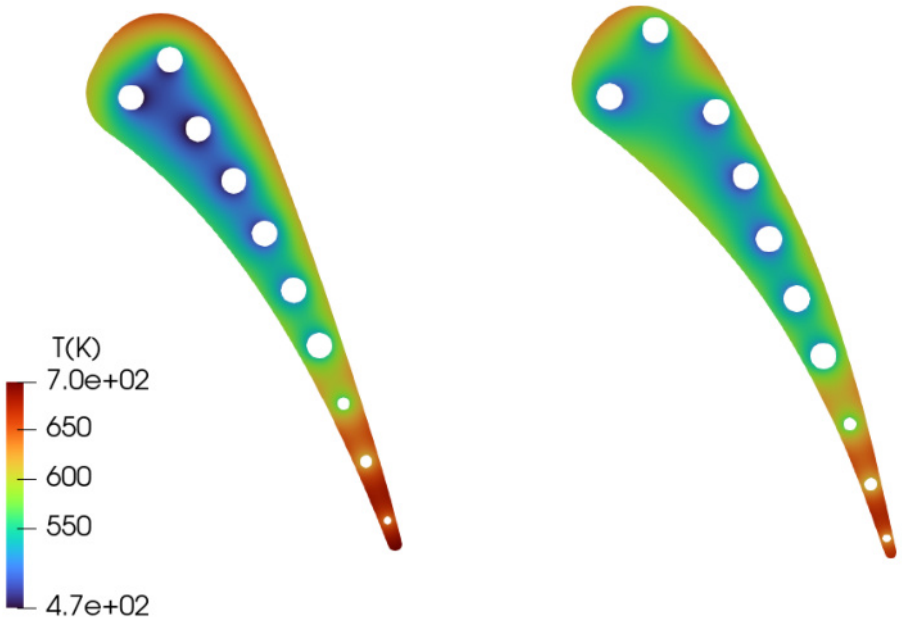

(a) temperature

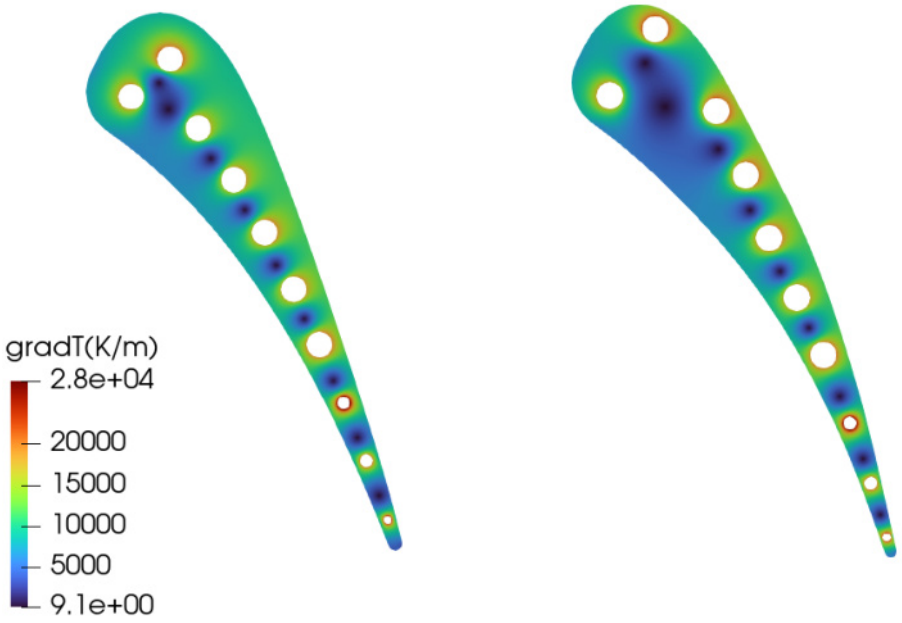

(b) temperature gradient

FIGURE 4.22: Temperature and temperature gradient magnitude distributions of the baseline (**left**) and TH2-157 optimized (**right**) blade.

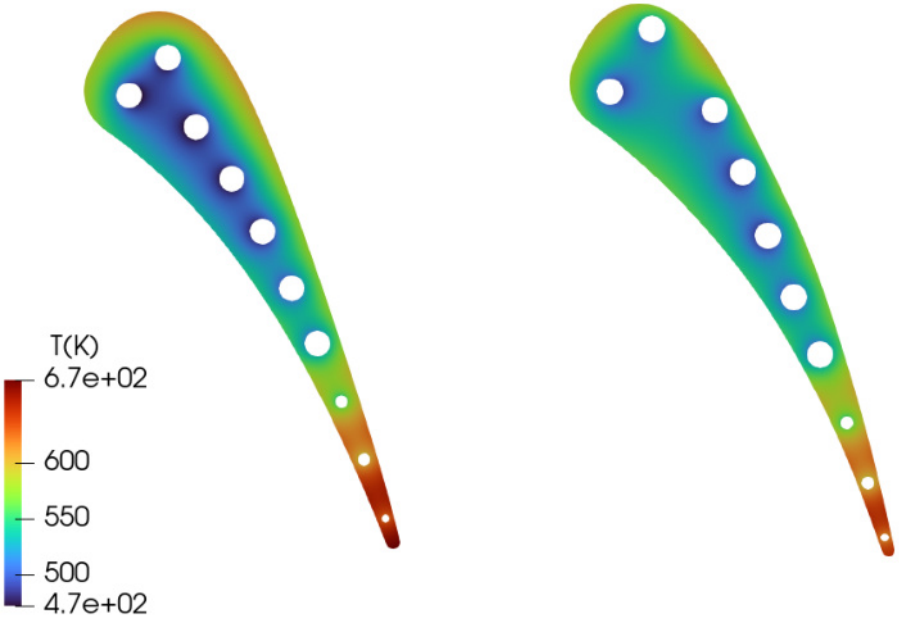

(a) temperature

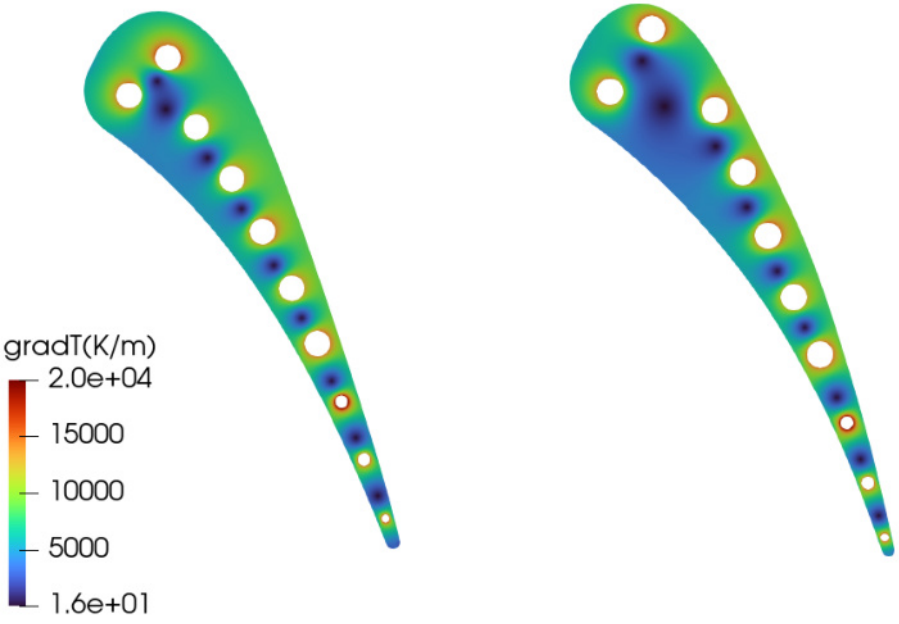

(b) temperature gradient

FIGURE 4.23: Temperature and temperature gradient magnitude distributions of the baseline (**left**) and TH2-158 optimized (**right**) blade.

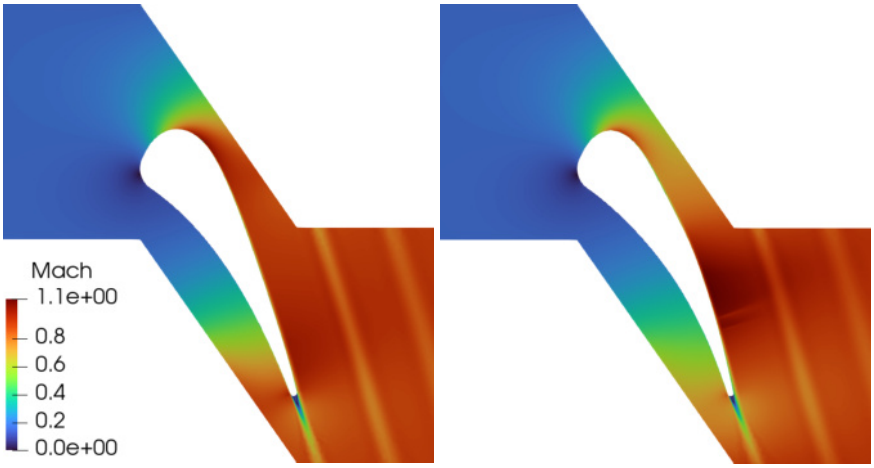

(a) baseline (b) TH2 opt.

FIGURE 4.24: Mach distribution of the baseline and TH2-108 optimized blade.

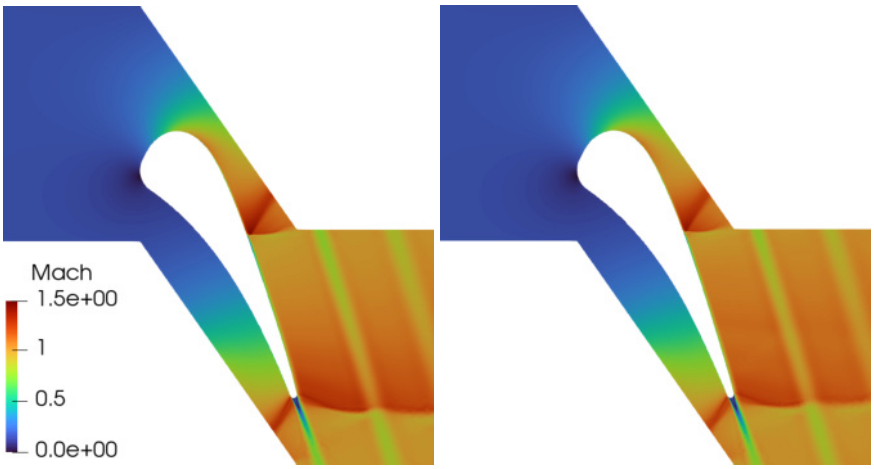

(a) baseline (b) TH2 opt.

FIGURE 4.25: Mach distribution of the baseline and TH2 optimized blade.

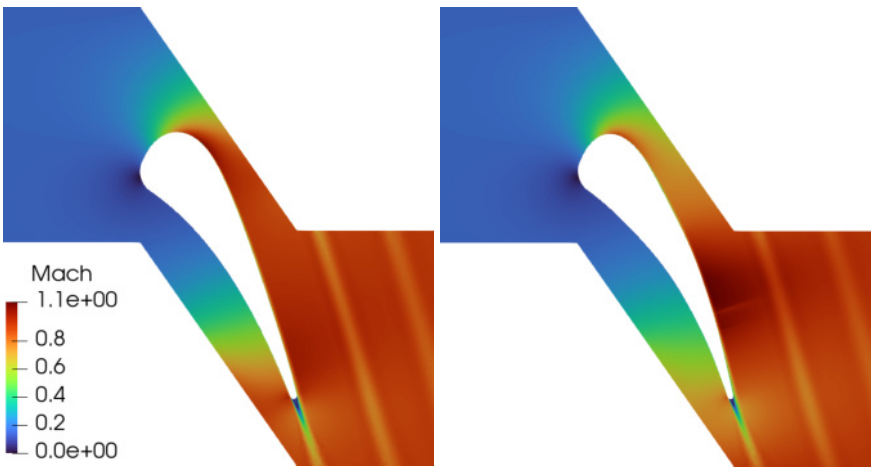

(a) baseline (b) TH2 opt.

FIGURE 4.26: Mach distribution of the baseline and TH2 optimized blade.

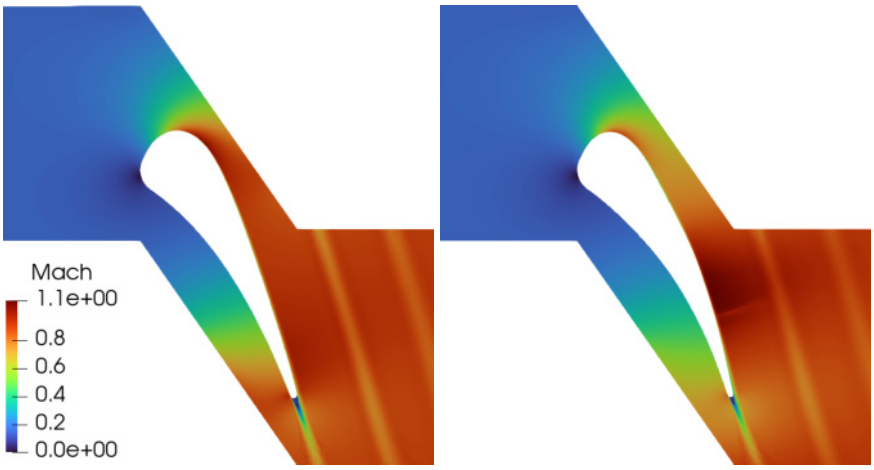

(a) baseline (b) TH2 opt.

FIGURE 4.27: Mach distribution of the baseline and TH2 optimized blade.

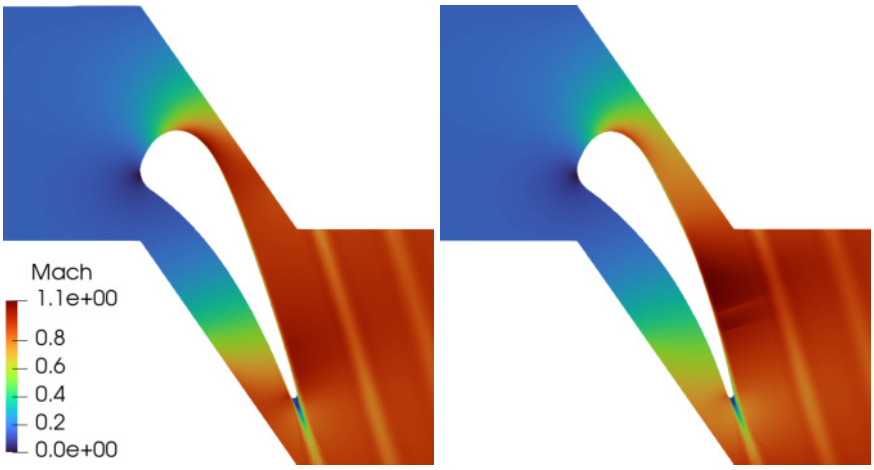

(a) baseline (b) TH2 opt.

FIGURE 4.28: Mach distribution of the baseline and TH2 optimized blade.

TABLE 4.5: Total pressure losses Δp_t (Pa) of the TH2 optimized blades.

flow conditions	**baseline**	**optimized blade**				
		108	**111**	**113**	**157**	**158**
108	5540.5	4281.2	5546.3	4267.0	4243.8	4362.1
111	12384.9	13644.9	10704.3	14002.9	14295.9	12684.8
113	5490.2	4247.5	5492.8	4216.3	4162.2	4332.9
157	6856.9	5299.8	6875.5	5260.6	5193.5	5406.6
158	4490.3	3519.4	4505.6	3570.4	3587.2	3547.5

TABLE 4.6: Inlet flow capacity $\dot{m}_1^*$ and flow exit angle a_2 of the baseline test-cases.

	108	**111**	**113**	**157**	**158**
$\dot{m}_1^* \cdot 10^5$	6.7053257	6.7597963	6.6941078	6.6961264	6.7105246
a_2 (rad)	-1.2755952	-1.2691205	-1.275526	-1.2755307	-1.2756093

TABLE 4.7: Inlet flow capacity percentage change % of the TH2 optimized blades.

flow conditions	**optimized blade**				
	108	**111**	**113**	**157**	**158**
108	0.1227	0.3498	0.1185	0.1154	0.0956
111	3.4615	0.1051	3.5051	3.6688	2.9503
113	0.1059	0.3578	0.1116	0.1117	0.0666
157	0.1184	0.3566	0.1238	0.1253	0.0753
158	0.1278	0.3344	0.1232	0.1222	0.1147

to the performance of the TH2-111 optimized blade.

4.3 Additional Parametric Studies

After the main optimization procedures had been completed, an additional set of runs was performed to test different approaches to the CHT problem. First, computations on pressure losses-optimized test-cases 111 and 158 were conducted, keeping either the 4 front (no. 1, 2, 3, 4) or the 3 last (no. 8, 9, 10) cooling holes intact, as illustrated in fig. 4.29. It can be deduced (fig. 4.31) that the front holes displacement only contributes by $\sim$ 0.3% and $\sim$ 0.15% to the $T_{\max}$ percentage change for the subsonic and transonic cases respectively (or a maximum temperature drop of $\sim$ - 2 K and $\sim$ - 1 K). In accordance with fig. 4.30, the displacement of the front holes reduces T^S locally but has no impact on T^S_{max} at the trailing edge. Figures 4.33 to 4.36 further validate that the temperature field in the trailing edge has not been affected by the front holes displacement.

TABLE 4.8: Exit flow angle (rad) of the TH2 optimized blades.

flow conditions	**optimized blade**				
	108	**111**	**113**	**157**	**158**
108	-1.2768	-1.2745	-1.2768	-1.2769	-1.2768
111	-1.2571	-1.2703	-1.2565	-1.2557	-1.2597
113	-1.2767	-1.2745	-1.2768	-1.2769	-1.2768
157	-1.2767	-1.2744	-1.2767	-1.2768	-1.2767
158	-1.2768	-1.2746	-1.2767	-1.2767	-1.2768

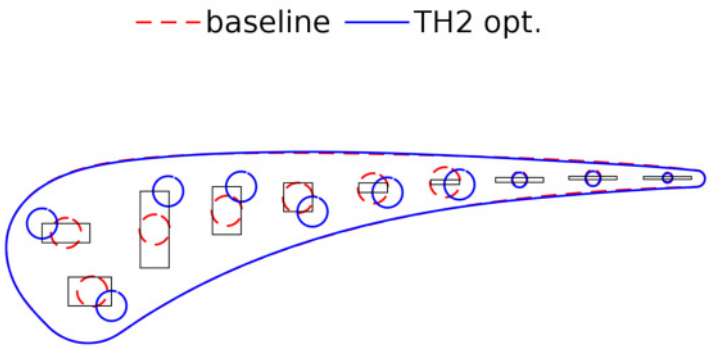

(a) TH2-111 opt., 3 back holes fixed

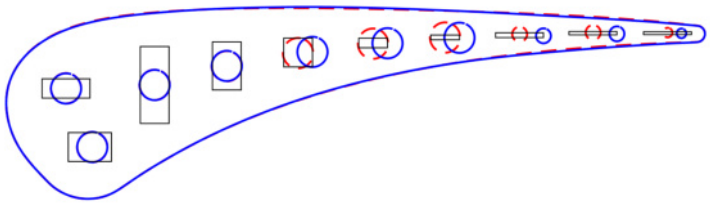

(b) TH2-111 opt., 4 front holes fixed

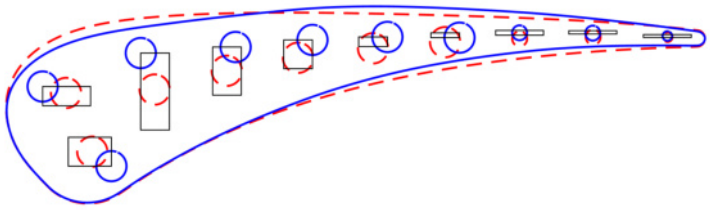

(c) TH2-158 opt., 3 back holes fixed

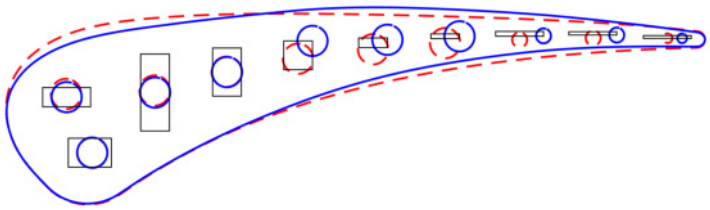

(d) TH2-158 opt., 4 front holes fixed

FIGURE 4.29: Comparison of the baseline and opt-TH2 configurations.

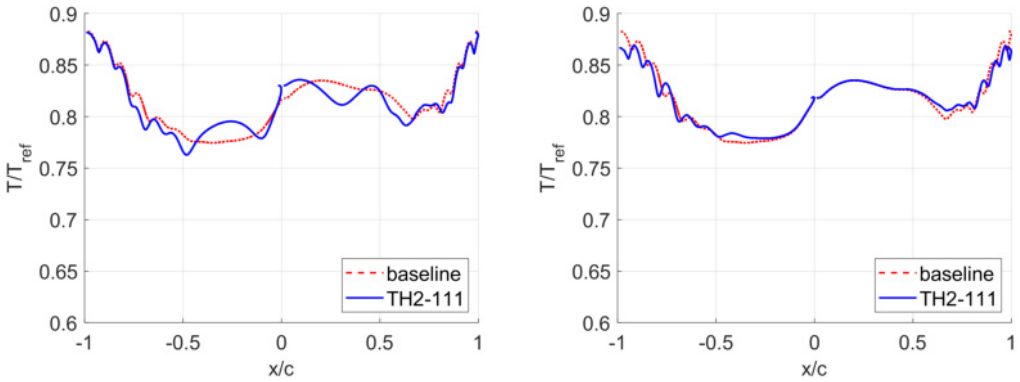

(a) 3 back holes fixed

(b) 4 front holes fixed

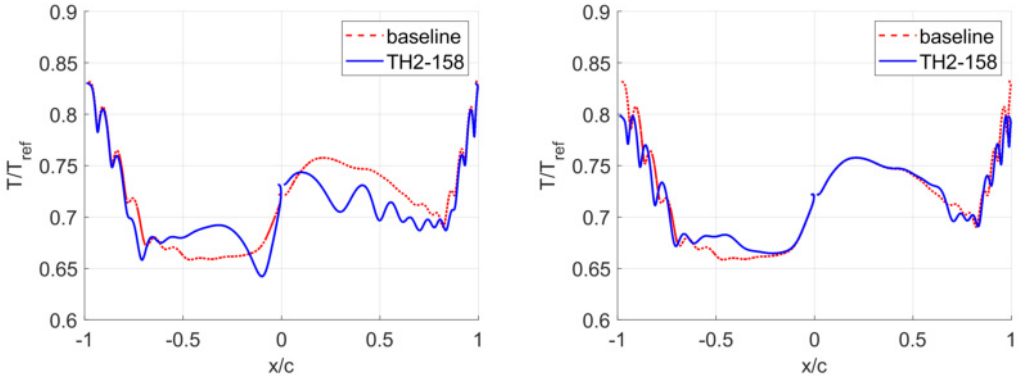

(c) 3 back holes fixed

(d) 4 front holes fixed

FIGURE 4.30: Comparison of the baseline and TH2 optimized temperature distribution along the blade airfoil contour (fixed holes runs).

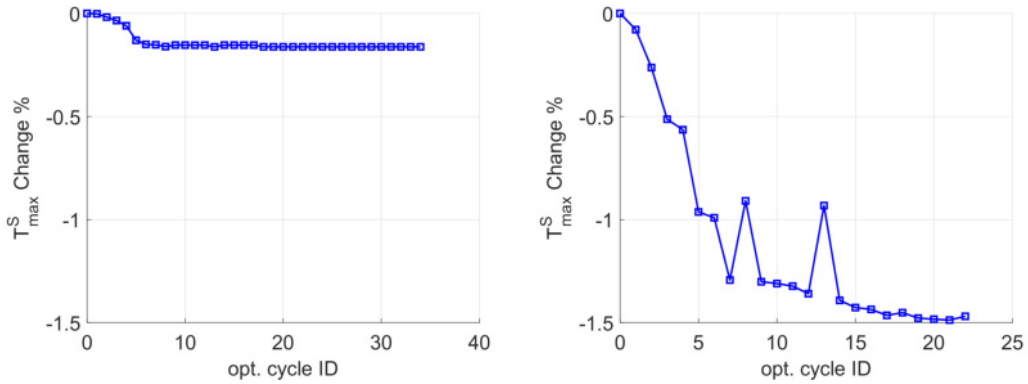

(a) TH2-111 opt. (3 back holes fixed)

(b) TH2-111 opt. (3 front holes fixed)

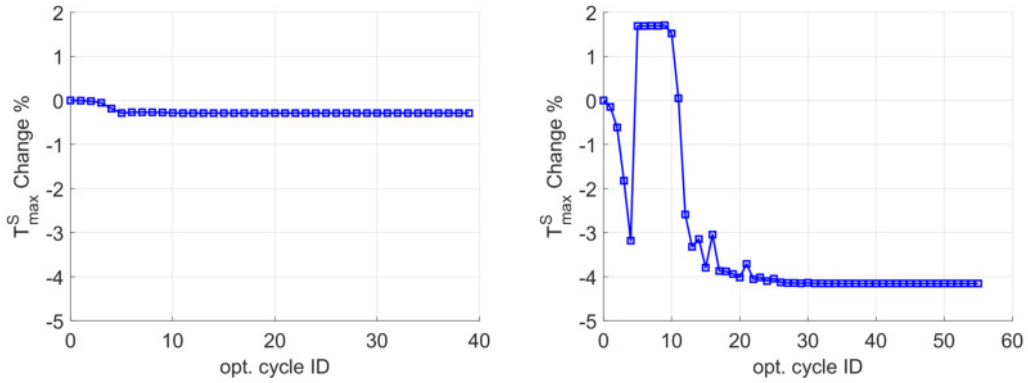

(c) TH2-158 opt. (3 back holes fixed)

(d) TH2-158 opt. (3 front holes fixed)

FIGURE 4.31: Convergence history of highest solid temperature for the TH2 optimization.

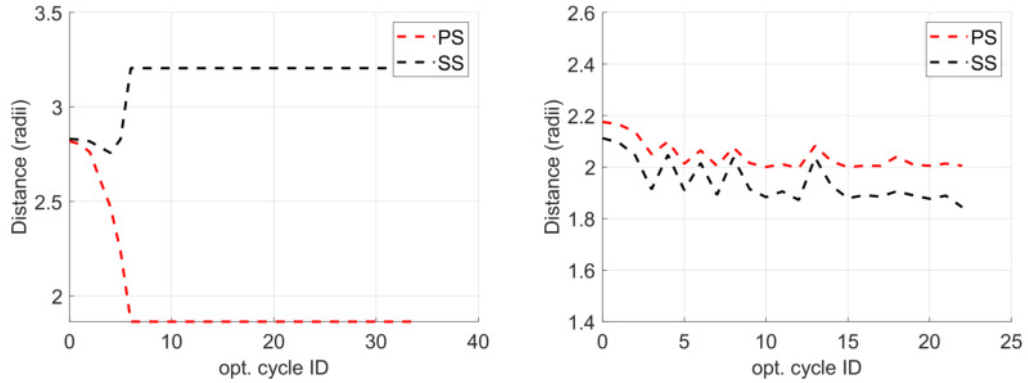

(a) TH2-111 opt. (3 back holes fixed)

(b) TH2-111 opt. (3 front holes fixed)

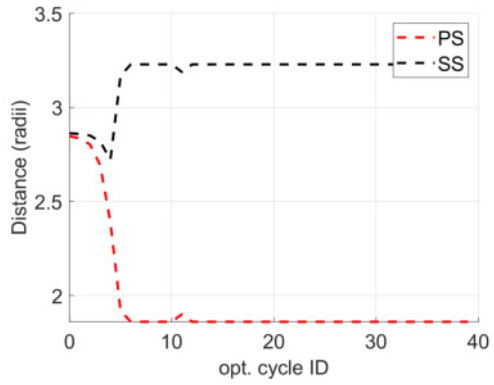

(c) TH2-158 opt. (3 back holes fixed)

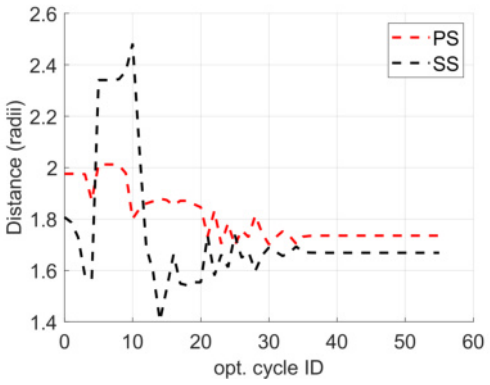

(d) TH2-158 opt. (3 front holes fixed)

FIGURE 4.32: Convergence history of 10^{th} hole's center distance from blade sides for the TH2 optimization.

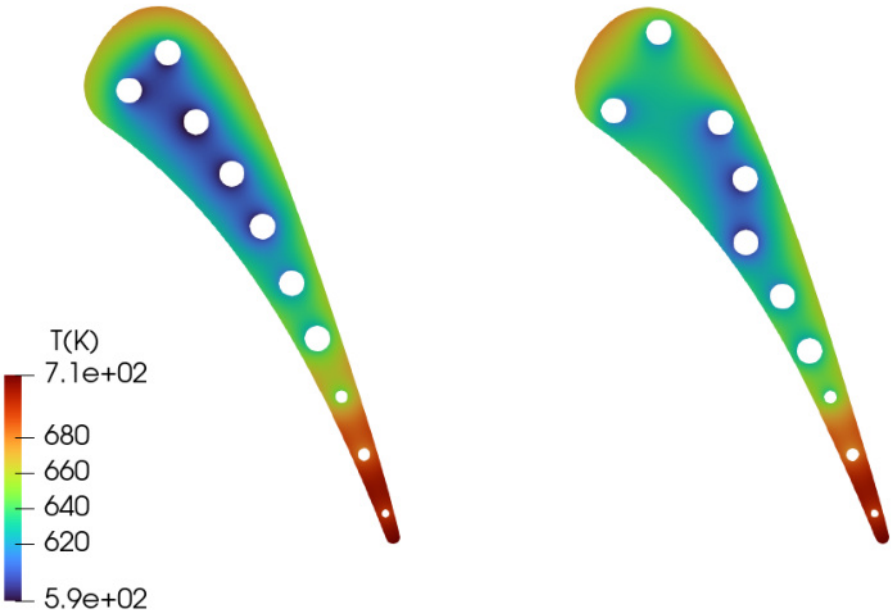

(a) temperature

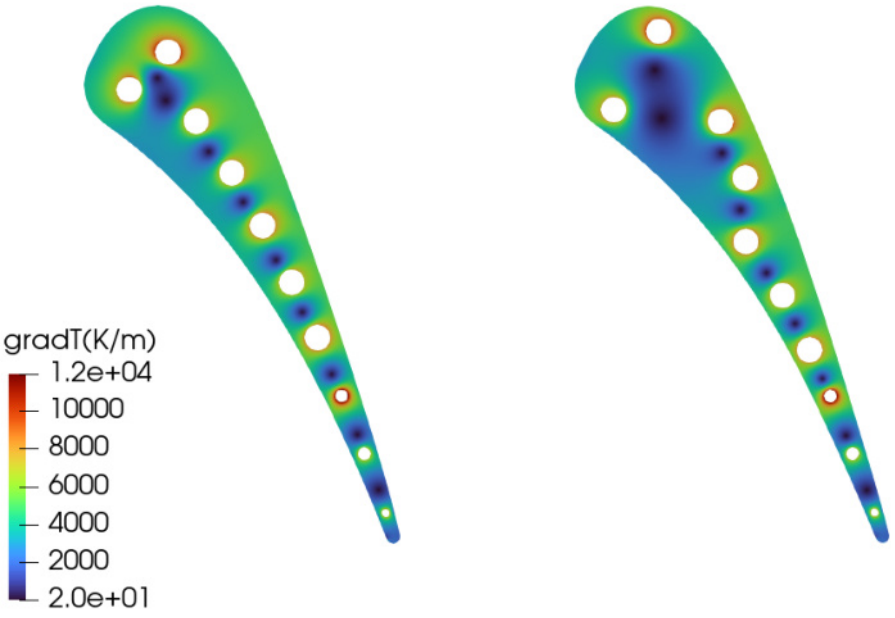

(b) temperature gradient

FIGURE 4.33: Temperature and temperature gradient magnitude distributions of the baseline (**left**) and TH2-111 optimized (**right**) blade (3 back holes fixed).

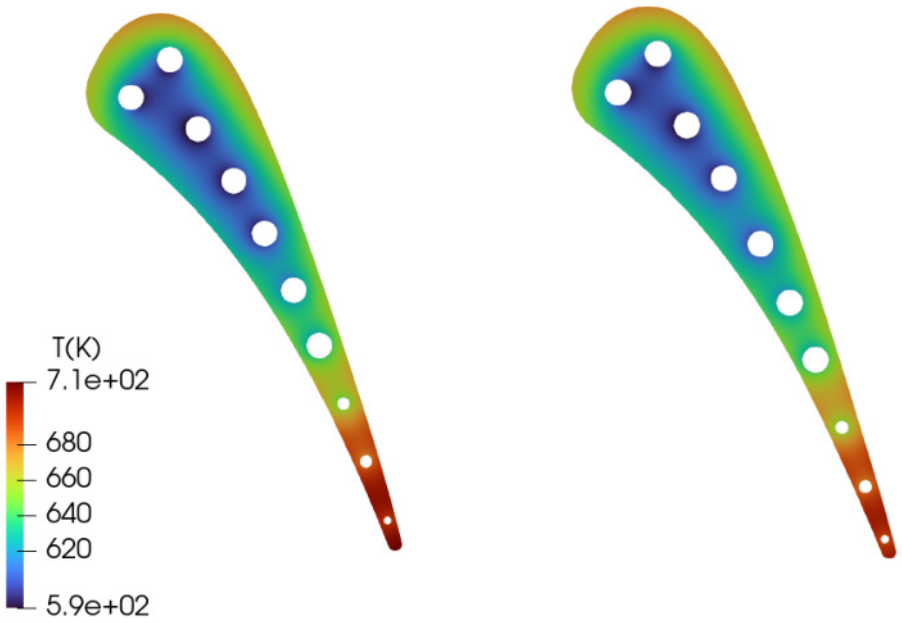

(a) temperature

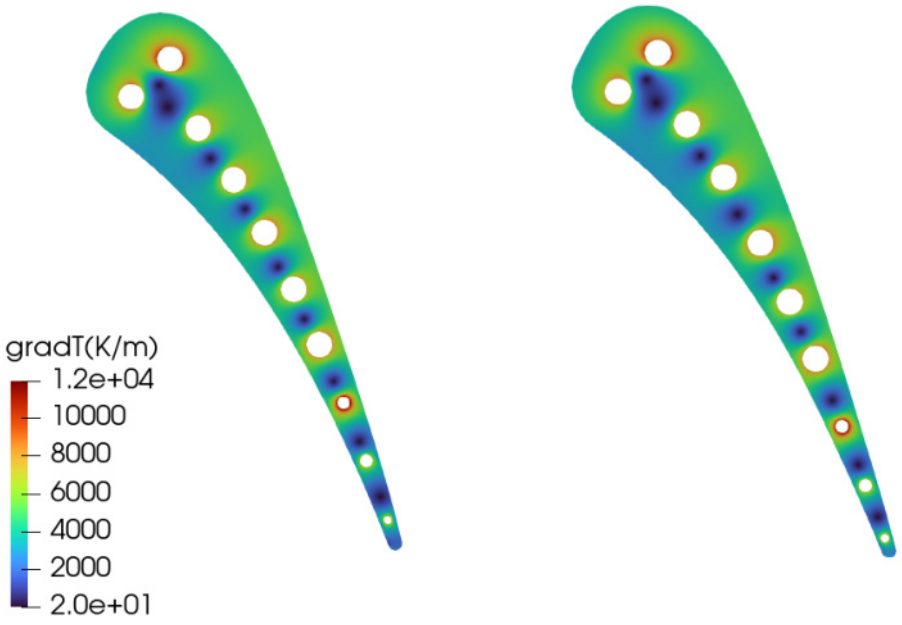

(b) temperature gradient

FIGURE 4.34: Temperature and temperature gradient magnitude distributions of the baseline (**left**) and TH2-111 optimized (**right**) blade (4 front holes fixed).

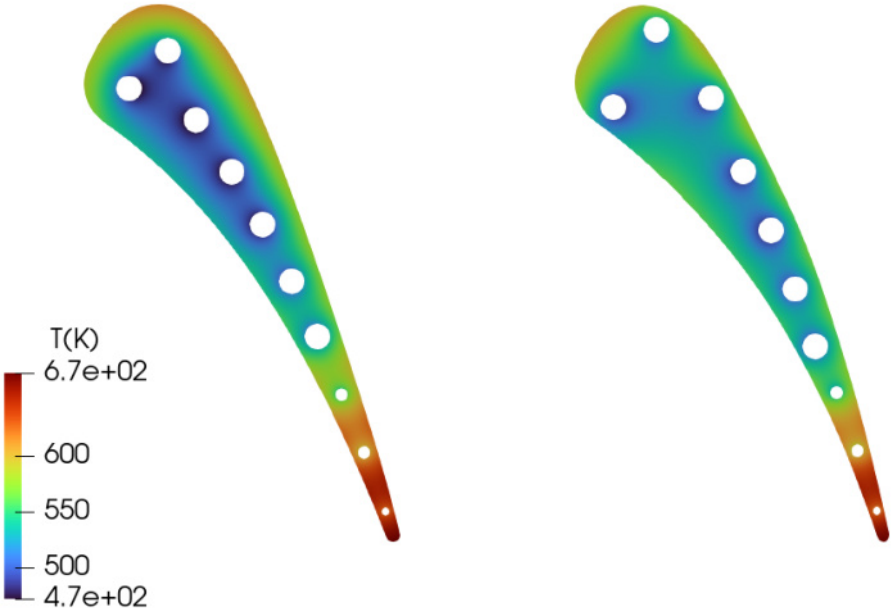

(a) temperature

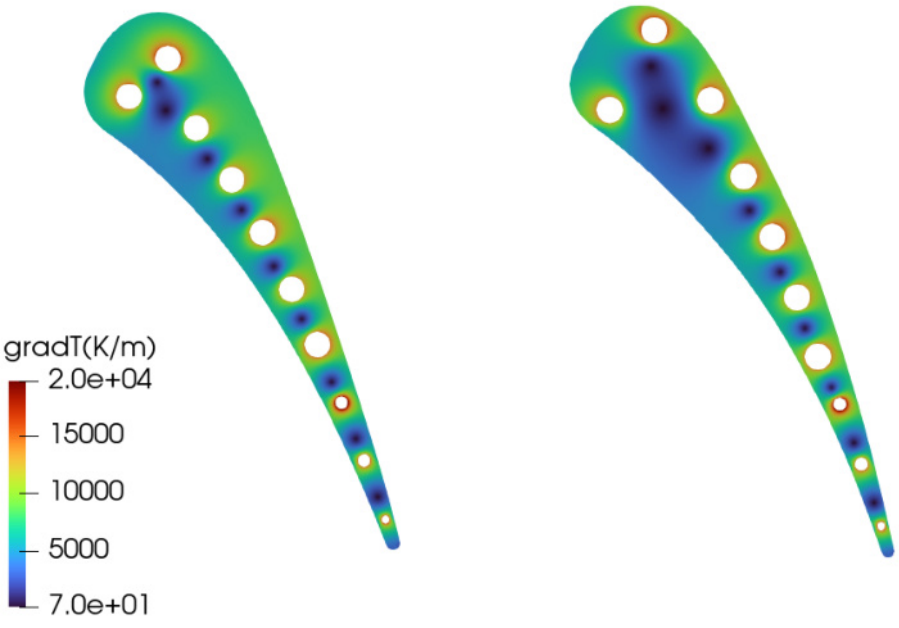

(b) temperature gradient

FIGURE 4.35: Temperature and temperature gradient magnitude distributions of the baseline (**left**) and TH2-158 optimized (**right**) blade (3 back holes fixed).

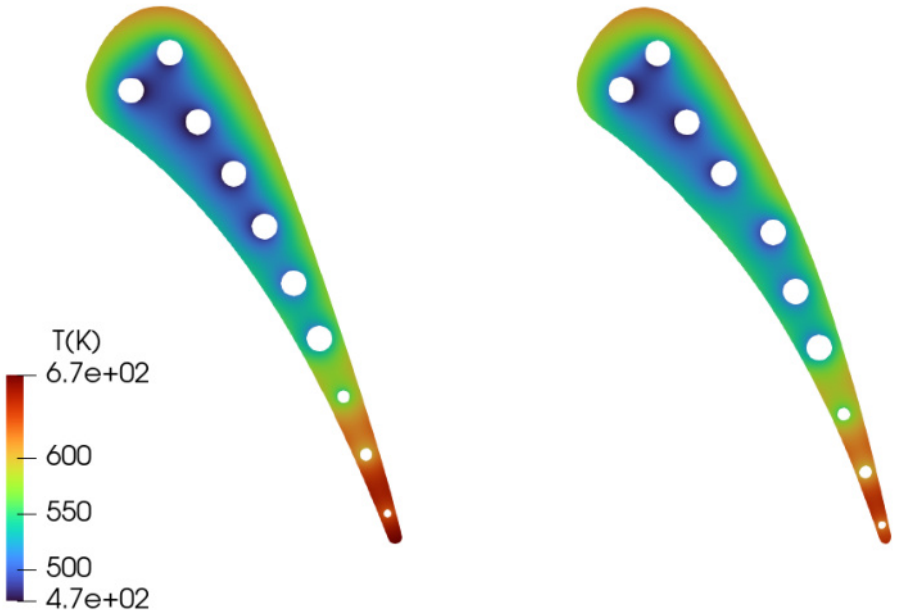

(a) temperature

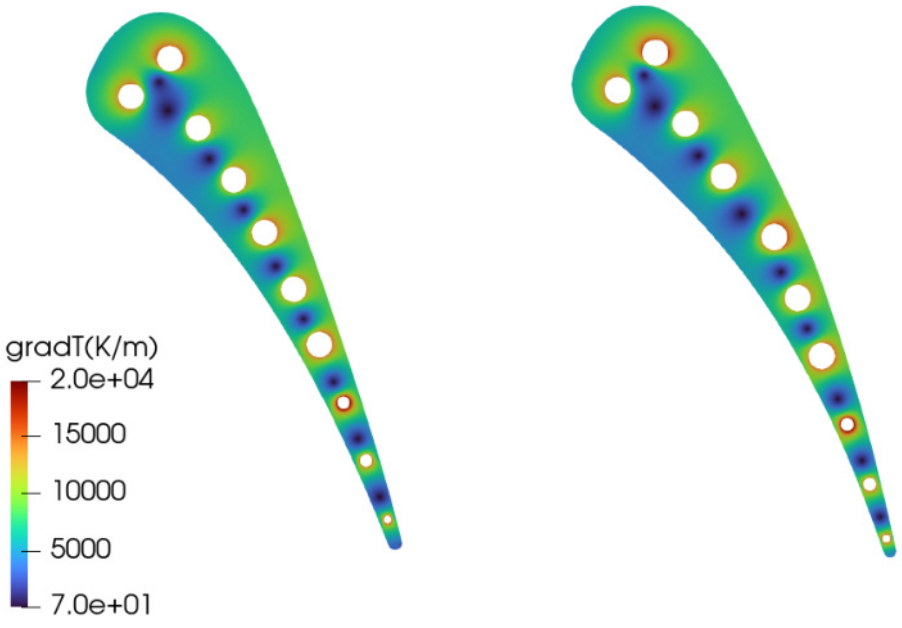

(b) temperature gradient

FIGURE 4.36: Temperature and temperature gradient magnitude distributions of the baseline (**left**) and TH2-158 optimized (**right**) blade (4 front holes fixed).

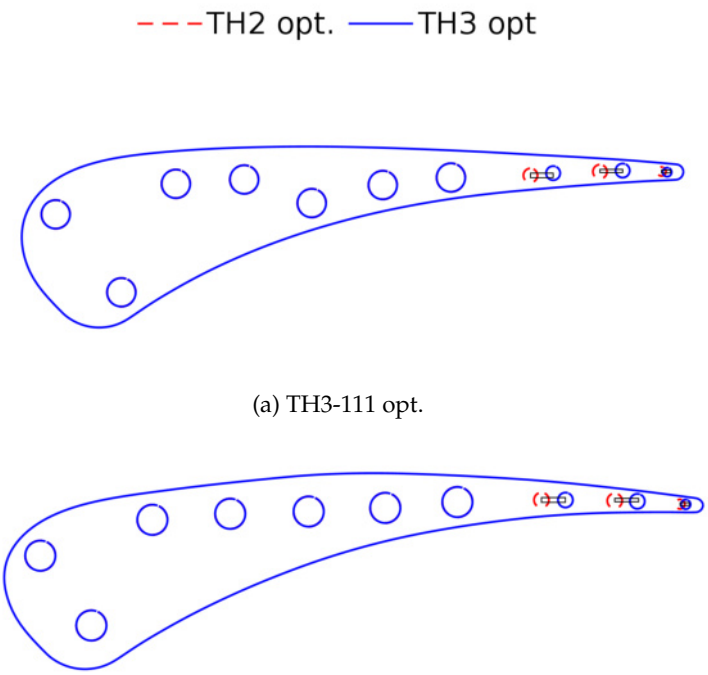

(a) TH3-111 opt.

(b) TH3-158 opt.

FIGURE 4.37: Comparison of the opt-TH2 and opt-TH3 configurations.

In addition, the TH2 optimized 111 and 158 cases were further optimized, setting a new vector of design variables to include only the coordinates of the 3 back holes. These holes were chosen as they are closer to the area of interest, where the highest temperature occurs. They are allowed to move within their respective areas, defined by the displacements in table 3.2, starting from their TH2 optimized positions, except that their x displacement is not allowed to be negative, i.e. they are only allowed to move closer to the trailing edge, as illustrated in fig. 4.37. In addition, the upper bound of hole no. 10 is not defined as a displacement but is kept as the maximum x coordinate bound corresponding to the TH2 optimization, to avoid any interaction with the trailing edge. The new candidate solutions will be referred to as TH3 optimized blades, as they have been optimized thrice. In this way, T^S_{max} is expected to be further reduced, as the holes are allowed to move closer to the trailing edge without being constrained from the bounds of the previous optimization. As can be seen in fig. 4.39, it is clear that the temperature has changed by $\sim -1.4\%$ for the 111 and $\sim -3\%$ for the 158 test-case, with small modifications in the holes' location, along the y direction. These percentages are equivalent to temperature drops from 699.2 to 689.8 K and from 642.2 to 622.9 K, respectively. In contrast, T^S has been increased between hole no. 7 and 8 (figs. 4.41 and 4.42) since hole no. 8 is shifted near the trailing edge, yet has not surpassed the maximum value. It is evident that with the displacement of the 3 last holes toward the trailing edge, the temperature field tends to be uniform with a lower maximum value in this region.

Finally, an optimization run was performed on total pressure losses-optimized case 108, reducing the total number of cooling holes from 10 to 9. Figure 4.43a illustrates the initial geometry used for the TH2 optimization, without hole no. 3. The displacement area of hole no. 4 has now been extended to include the space left by

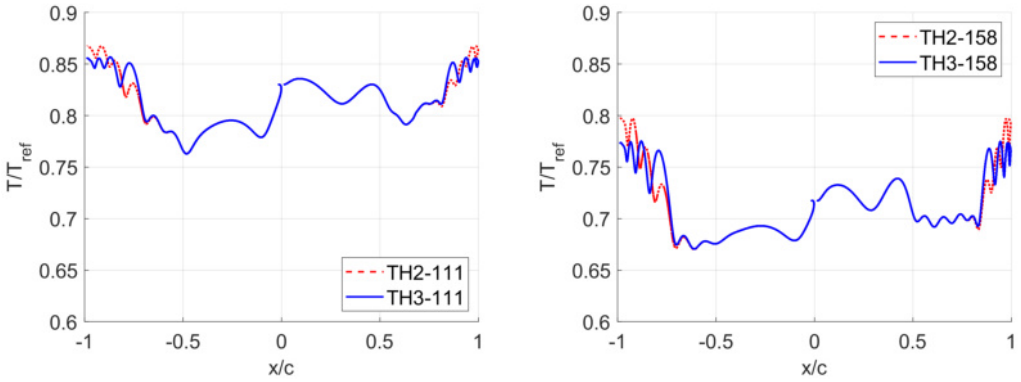

(a) (b)

FIGURE 4.38: Comparison of the TH2 optimized and TH3 optimized temperature distribution along the blade airfoil contour.

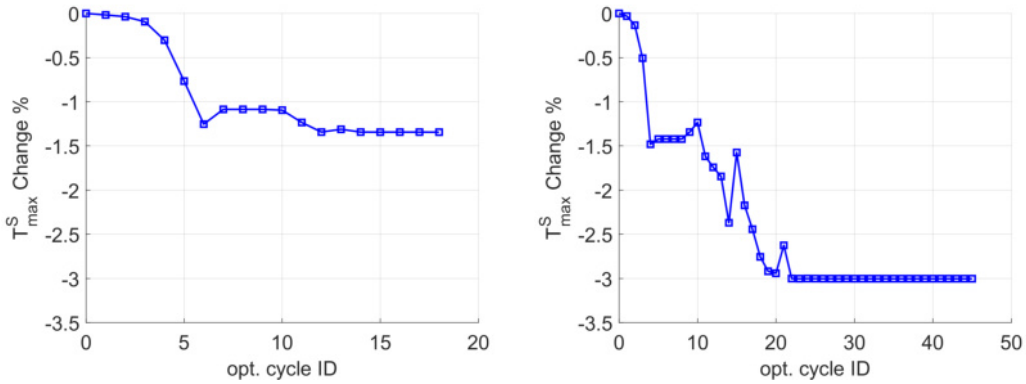

(a) TH3-111 opt. (b) TH3-158 opt.

FIGURE 4.39: Convergence history of highest solid temperature for the TH3-111 optimization.

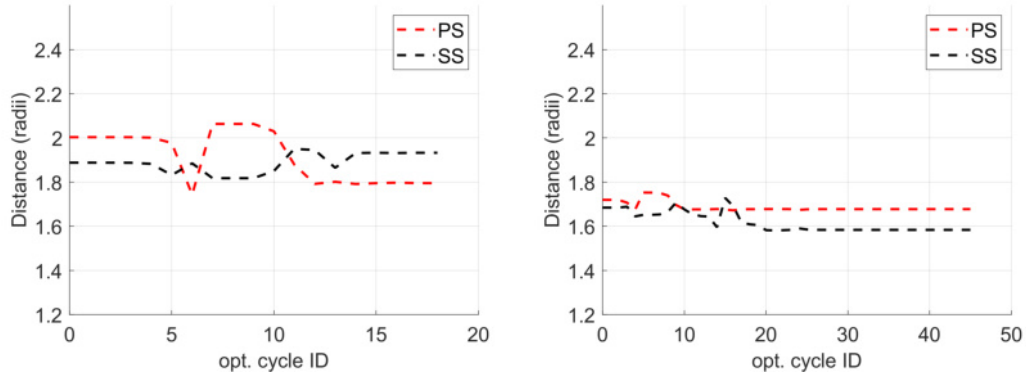

(a) TH3-111 opt. (b) TH3-158 opt.

FIGURE 4.40: Convergence history of 10^{th} hole's center distance from blade sides for the TH3-158 optimization.

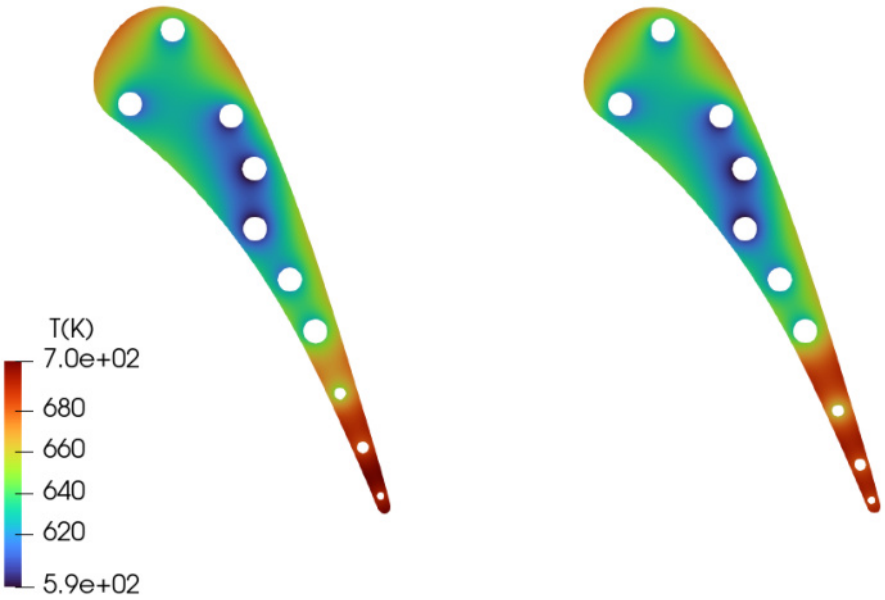

(a) temperature

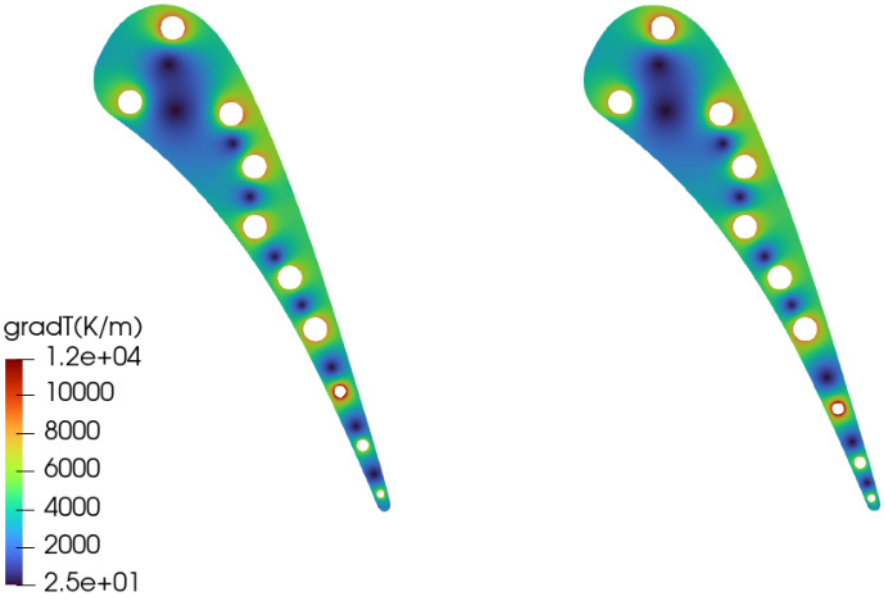

(b) temperature gradient

FIGURE 4.41: Temperature and temperature gradient magnitude distributions of the TH2-111 and TH3-111 optimized (**right**) blade.

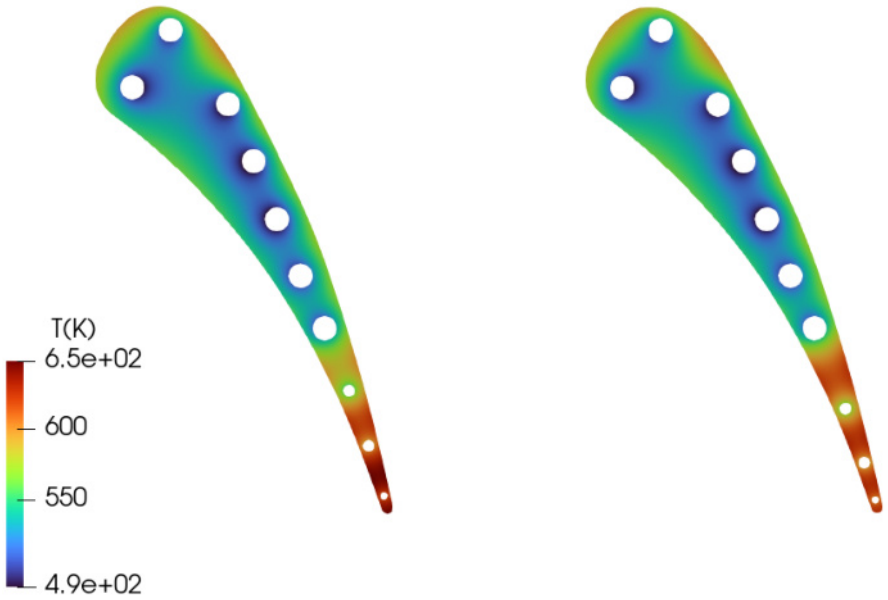

(a) temperature

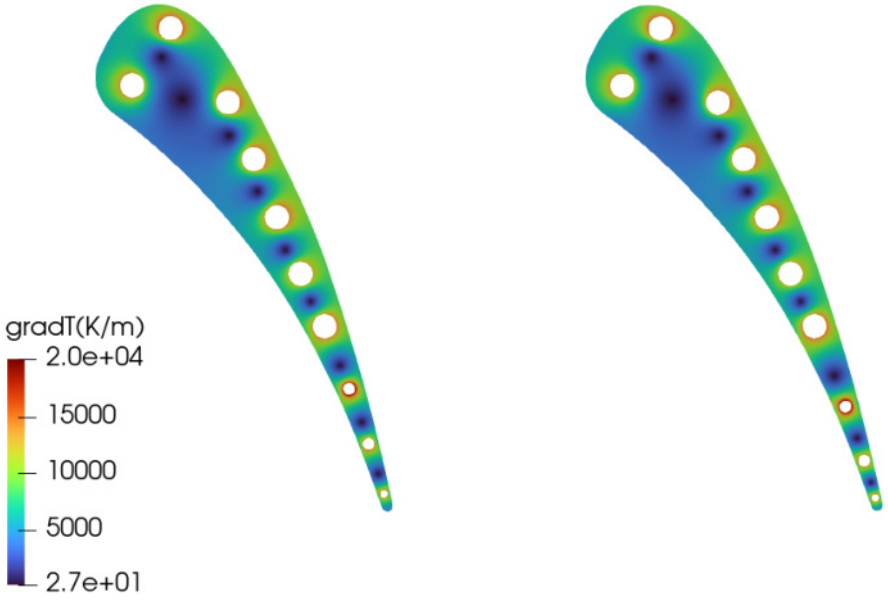

(b) temperature gradient

FIGURE 4.42: Temperature and temperature gradient magnitude distributions of the TH2-158 and TH3-158 optimized (**right**) blade.

hole no. 3. There is a $T^S_{\max}$ drop equal to $\sim -4\%$, although T^S increases up to the maximum value in the front half of the suction side, based on figs. 4.43d and 4.44. The above analysis highlights the importance of the front holes, as they may not impact the $T^S_{\max}$ of the trailing edge, yet they cool down the front part of the airfoil, meaning that by removing them, there is a high risk of rising T^S to the levels of the maximum value in the region, where they are located.

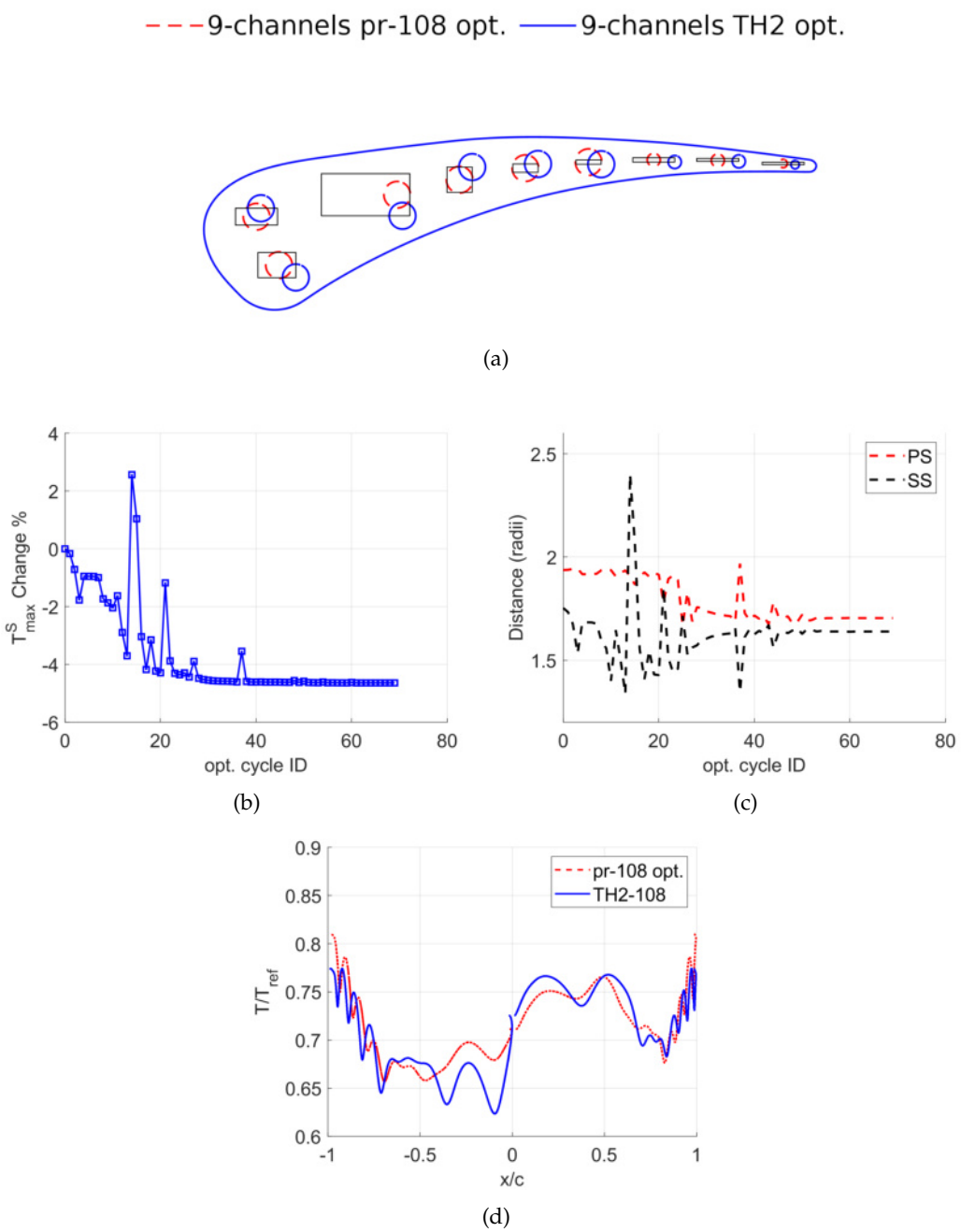

FIGURE 4.43: Properties of the TH2-108 optimized geometry without hole no. 3. (a) New configuration (b) convergence history of highest solid temperature (c) convergence history of 9th hole's center distance from blade sides (d) temperature distribution along the blade airfoil contour.

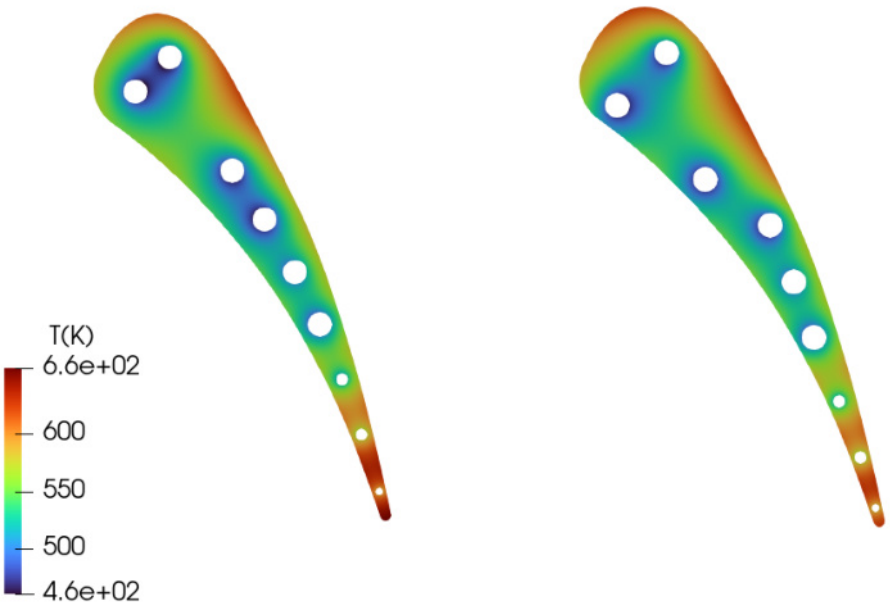

(a) temperature

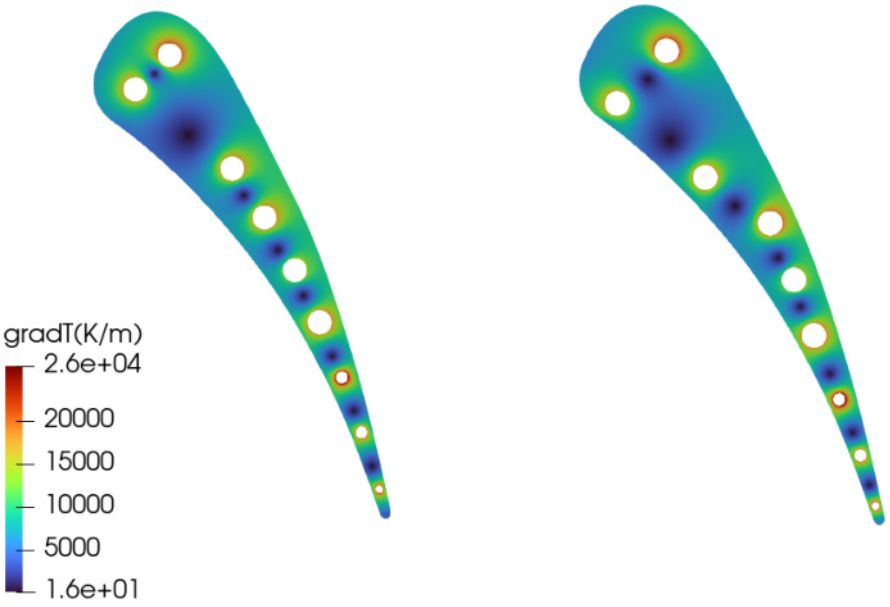

(b) temperature gradient

FIGURE 4.44: Temperature and temperature gradient magnitude distributions of the pr-108 and TH3-108 optimized (**right**) blade.

5 Conclusions

This chapter presents the findings of the whole study, along with important observations and future suggestions.

- Except for the first half of the blade's suction side, where an overestimation of T^S and h^S is observed, the results for the primal problem are in good agreement with the experimental data of the C3X turbine blade in the remaining airfoil contour. The lack of a transition model, given that the adjoint equations should be formulated from scratch, leads to a poor prediction in that region. This is soon to be resolved as the inclusion of the $\gamma - \mathrm{Re}_\theta$ transition model into the continuous adjoint method is already under development at the PCOpt.

- The optimization procedure, involving the initial constraints, converges to a T^S_{max} drop equal to $\sim 4\%$ for the subsonic cases and $\sim 1.5\%$ for the transonic one. Using the total pressure losses-optimized airfoils as the starting geometry, the results give a slightly higher T^S_{max} (by ~ 1 K) from the baseline geometry.

- The key factor for the aerothermal optimization of the airfoil is the displacement of channel no. 10 (the one closest to the trailing edge) along the x direction. The front channels have almost no impact on the minimization of the objective function T^S_{max}.

- A second displacement toward the trailing of the 3 back channels, compared to their optimized positions, leads to an additional $\sim 3\%$ and $\sim 1.4\%$ T^S_{max} drop (for the subsonic and transonic cases respectively). It seems that a dynamic constraint needs to be developed in the future, by computing the distance between them and the airfoil sides and updating the constraints at the end of each optimization cycle.

- Removal of a cooling channel, even one away from the trailing edge, can lead to higher T^S in the region, at risk of getting close to the maximum value. Any modifications of the cooling channels' number should be carefully executed, by updating the constraints of the adjacent channels to cover the free space left behind from those removed.

Bibliography

[1] A. C. Aitken. "XXV.-On Bernoulli's Numerical Solution of Algebraic Equations". en. In: *Proceedings of the Royal Society of Edinburgh* 46 (1927), pp. 289–305. DOI: 10.1017/S0370164600022070.

[2] V. G. Asouti, X. S. Trompoukis, I. C. Kampolis, and K. C. Giannakoglou. "Unsteady CFD Computations Using Vertex-Centered Finite Volumes for Unstructured Grids on Graphics Processing Units". en. In: *International Journal for Numerical Methods in Fluids* 67.2 (Sept. 2011), pp. 232–246. DOI: 10.1002/fld.2352.

[3] D. De Marinis, M.D. de Tullio, M. Napolitano, and G. Pascazio. "A Conjugate-Heat-Transfer Immersed-Boundary Method for Turbine Cooling". en. In: *Energy Procedia* 82 (Dec. 2015), pp. 215–221. DOI: 10.1016/j.egypro.2015.12.025.

[4] K. T. Gkaragkounis. "The Continuous Adjoint Method in Aerodynamic and Conjugate Heat Transfer Shape Optimization, for Turbulent Flows". PhD thesis. National Technical University of Athens, 2020.

[5] K. T. Gkaragkounis, E. M. Papoutsis-Kiachagias, and K. C. Giannakoglou. "The Continuous Adjoint Method for Shape Optimization in Conjugate Heat Transfer Problems with Turbulent Incompressible Flows". en. In: *Applied Thermal Engineering* 140 (July 2018), pp. 351–362. DOI: 10.1016/j.applthermaleng.2018.05.054.

[6] L.D. Hylton and Lewis Research Center. *Analytical and Experimental Evaluation of the Heat Transfer Distribution Over the Surfaces of Turbine Vanes: Final Report*. NASA contractor report. National Aeronautics and Space Administration, NASA Lewis Research Center, 1983. URL: https://books.google.gr/books?id=YFfsswEACAAJ.

[7] A. Jameson, Wolfgang Schmidt, and Eli Turkel. "Numerical Solution of the Euler Equations by Finite Volume Methods Using Runge Kutta Time Stepping Schemes". en. In: *14th Fluid and Plasma Dynamics Conference*. Palo Alto,CA,U.S.A.: American Institute of Aeronautics and Astronautics, June 1981. DOI: 10.2514/6.1981-1259.

[8] I.S. Kavvadias, E.M. Papoutsis-Kiachagias, and K.C. Giannakoglou. "On the Proper Treatment of Grid Sensitivities in Continuous Adjoint Methods for Shape Optimization". en. In: *Journal of Computational Physics* 301 (Nov. 2015), pp. 1–18. DOI: 10.1016/j.jcp.2015.08.012.

[9] S. H. Lo. "A New Mesh Generation Scheme for Arbitrary Planar Domains". en. In: *International Journal for Numerical Methods in Engineering* 21.8 (Aug. 1985), pp. 1403–1426. DOI: 10.1002/nme.1620210805.

[10] K. Mazaheri, M. Zeinalpour, and H.R. Bokaei. "Turbine Blade Cooling Passages Optimization Using Reduced Conjugate Heat Transfer Methodology". en. In: *Applied Thermal Engineering* 103 (June 2016), pp. 1228–1236. DOI: 10.1016/j.applthermaleng.2016.05.007.

[11] R. Moretti, M. P. Errera, Vi. Couaillier, and F. Feyel. "Stability, Convergence and Optimization of Interface Treatments in Weak and Strong Thermal Fluid-Structure Interaction". en. In: *International Journal of Thermal Sciences* 126 (Apr. 2018), pp. 23–37. DOI: 10.1016/j.ijthermalsci.2017.12.014.

[12] G. Nowak and W. Wroblewski. "Optimization of Blade Cooling System with Use of Conjugate Heat Transfer Approach". en. In: *International Journal of Thermal Sciences* 50.9 (Sept. 2011), pp. 1770–1781. DOI: 10.1016/j.ijthermalsci.2011.04.001.

[13] D. Panagiotopoulos. "Shape Optimization of an Internally Cooled Turbine Blade Airfoil Using the Continuous Adjoint Method". Diploma thesis. National Technical University of Athens, 2022.

[14] D.I. Papadimitriou and K.C. Giannakoglou. "A Continuous Adjoint Method with Objective Function Derivatives Based on Boundary integrals, for Inviscid and Viscous Flows". en. In: *Computers & Fluids* 36.2 (Feb. 2007), pp. 325–341. DOI: 10.1016/j.compfluid.2005.11.006.

[15] E. M. Papoutsis-Kiachagias and K. C. Giannakoglou. "Continuous Adjoint Methods for Turbulent Flows, Applied to Shape and Topology Optimization: Industrial Applications". en. In: *Archives of Computational Methods in Engineering* 23.2 (June 2016), pp. 255–299. DOI: 10.1007/s11831-014-9141-9.

[16] P.L Roe. "Approximate Riemann Solvers, Parameter Vectors, and Difference Schemes". en. In: *Journal of Computational Physics* 43.2 (Oct. 1981), pp. 357–372. DOI: 10.1016/0021-9991(81)90128-5.

[17] P. Spalart and S. Allmaras. "A One-Equation Turbulence Model for Aerodynamic Flows". en. In: *30th Aerospace Sciences Meeting and Exhibit*. Reno,NV,U.S.A.: American Institute of Aeronautics and Astronautics, Jan. 1992. DOI: 10.2514/6.1992-439.

[18] William Sutherland. "LII. *The Viscosity of Gases and Molecular Force*". en. In: *The London, Edinburgh, and Dublin Philosophical Magazine and Journal of Science* 36.223 (Dec. 1893), pp. 507–531. DOI: 10.1080/14786449308620508.

[19] K. Svanberg. "The Method of Moving Asymptotes - a New Method for Structural Optimization". en. In: *International Journal for Numerical Methods in Engineering* 24.2 (Feb. 1987), pp. 359–373. DOI: 10.1002/nme.1620240207.

[20] X. Trompoukis, K. Tsiakas, V. Asouti, M. Kontou, and K. Giannakoglou. "Continuous Adjoint-Based Optimization of an Internally Cooled Turbine Blade-Mathematical Development and Application". en. In: *International Journal of Turbomachinery, Propulsion and Power* 6.2 (June 2021), p. 20. DOI: 10.3390/ijtpp6020020.

[21] B. Wang, W. Zhang, G. Xie, Y. Xu, and M. Xiao. "Multiconfiguration Shape Optimization of Internal Cooling Systems of a Turbine Guide Vane Based on Thermomechanical and Conjugate Heat Transfer Analysis". en. In: *Journal of Heat Transfer* 137.6 (June 2015), p. 061004. DOI: 10.1115/1.4029852.

[22] A.S. Zymaris, D.I. Papadimitriou, K.C. Giannakoglou, and C. Othmer. "Continuous Adjoint Approach to the Spalart–Allmaras Turbulence Model for Incompressible Flows". en. In: *Computers & Fluids* 38.8 (Sept. 2009), pp. 1528–1538. DOI: 10.1016/j.compfluid.2008.12.006.